APPLICATION OF A PROTON LINEAR ACCELERATOR FOR CANCER THERAPY TO RADIATION RESISTANCE QUALIFICATION OF SPACE COMPONENTS AND SYSTEMS

A PHD DISSERTATION
SUBMITTED IN PARTIAL FULFILMENT OF THE REQUIREMENTS FOR THE DEGREE OF

DOCTOR OF PHILOSOPHY

IN ENERGY AND ENVIRONMENT

AUTHORED BY

GIULIA BAZZANO

SUPERVISED BY

PROF. GIOVANNI B. PALMERINI

XXXIV CYCLE
2019-2021

DEPARTMENT OF ASTRONAUTICAL, ELECTRIC AND ENERGY ENGINEERING
(DIAEE)
SAPIENZA UNIVERSITY OF ROME

SAPIENZA
UNIVERSITÀ DI ROMA

TABLE OF CONTENTS

ABSTRACT

The thesis focuses mainly on demonstrating the possibility to successfully employ a full-LINAC proton accelerator designed for particle therapy to perform irradiations of electronic components for space applications fulfilling the European Space Components Coordination standard prescriptions on beam qualification. The research activity is carried out at the TOP-IMPLART proton accelerator: it is a prototype of a pulsed fully linear machine aimed at active intensity modulated proton therapy under development at ENEA Frascati Research Centre in collaboration with the Italian Institute of Health (ISS) and the Oncological Hospital Regina Elena-IFO. Design beam properties of this accelerator, such as extraction energy, energy spread, transverse spot size and average current, are the same as conventional cyclotron-based facilities for proton therapy, whereas the instantaneous beam current is orders of magnitude higher as the beam is delivered in 3 μs long pulses with a maximum repetition rate of 200 Hz.

In the first part of the research activity, we describe the methods and specific beam detectors developed for the characterization in air of the proton beam of the TOP-IMPLART linac and discuss how the clinical-oriented methods can be employed for Radiation Hardness Assurance purposes. In particular, we want to demonstrate the capability of our delivery system to provide a continuous monitoring of the proton flux and fluence with an accuracy of at least ± 10%. This, coupled with a characterization of the beam parameters (energy, energy spectrum, transverse uniformity) at the target position with the same accuracy, shall fulfil the typical prescription of standard procedures for electronic components irradiation Beam energy and spectrum, transverse homogeneity, fluence and flux are assessed both experimentally and by numerical calculations.

We than presents three irradiation campaigns carried out at a beam energy of 35 MeV: they were selected as exemplary of the different radiation hardness tests that can be performed with protons: displacement damage effects, single event effects and system level qualification where cumulative and stochastic effects are probed simultaneously. The outcomes of the irradiation campaigns are discussed

in terms of lesson learned aiming constantly improving the methodology to better comply with the international standards.

Lastly, we present the upgrade in the beam monitoring system carried out together with the energy upgrade to 55.5 MeV. Development of a new current monitor and new online control system for two existing devices are reported. They significantly improve fluence and flux monitoring precision, benefiting future RHA activities.

Chapter 1
INTRODUCTION

In this Chapter, the framework for the research activities is presented in Sec. 1.1 to Sec 1.4 and the main contents of the thesis are highlighted in Sec. 1.5**Errore. L'origine riferimento non è stata trovata.**

1.1 ELECTRONIC PARTS SPACE RADIATION TESTING AND THE STATE OF THE INFRASTRUCTURE

In fall 2016, the Department of Energy, with NASA and U.S. Air Force support, asked the National Academies of Sciences, Engineering, and Medicine to undertake a study on the testing facilities in the United States for radiation-hardened electronics for spacecraft. The report, "Testing at the speed of light – The state of U.S. electronic parts space radiation testing infrastructure", was published in 2018 (*Testing at the Speed of Light*, 2018). Here we report an extract from the Summary:

"Spacecraft depend on electronic components that must perform reliably over missions measured in years and decades. Space radiation is a primary source of degradation, reliability issues, and potentially failure for these electronic components. This report of the Committee on Space Radiation Effects Testing Infrastructure for the U.S. Space Program evaluates the nation's current capabilities and future needs for testing the effects of space radiation on microelectronics to ensure mission success and makes recommendations on how to provide effective stewardship of the necessary radiation test infrastructure for

the foreseeable future. Although simulation and modelling is valuable for understanding the radiation risk to microelectronics, there is no substitute for testing, and an increased use of commercial-off-the-shelf (COTS) parts in spacecraft may actually increase requirements for testing, as opposed to simulation and modelling. Although the effort of testing may be difficult and expensive, it is small compared to the cost of a radiation-induced failed mission, which can be hundreds of millions of dollars, not to mention the inability to conduct the mission. This study was conducted at the request of the U.S. Department of Energy (DOE), the U.S. Air Force, and NASA, all of which have an interest in the testing infrastructure for space electronics. It was initiated because these organizations are concerned about the adequacy of the current testing infrastructure and its ability to meet the growing demands for national security, civil, and commercial space systems. Radiation that threatens space missions derives from three main natural sources: galactic cosmic rays (GCRs), consisting of protons, electrons, and ionized heavy nuclei; charged particles (mainly protons and electrons) trapped by planetary magnetic fields (e.g., Earth's Van Allen belts); and solar particle events (SPEs) that occasionally flood regions of space with large fluxes of energetic protons and heavier nuclei. Together, these sources create a radiation environment of high-energy electrons with energies from a few electron volts (eV) to as high as tens of millions of electron volts (megaelectron volts, MeV) (as in the Jovian environment), protons with appreciable fluxes at energies from a few electron volts to hundreds of megaelectron volts, and heavy ions with energies from ~1 MeV per nucleon to several thousand megaelectron volts per nucleon. Spacecraft electronics are susceptible to radiation effects that emerge from interactions with these energetic particles—both degradation and eventual failure—due to total ionizing dose (TID) and displacement damage dose (DDD) and the instantaneous response of the electronics to single ionizing particles, called single-event effects (SEEs). If electronics are not "hardened" to both cumulative and single-event radiation effects, they will likely experience these effects in space, resulting in performance anomalies and the potential compromise of space missions. SEE testing fulfils several roles, including the following: hardening of electronics technology; measuring susceptibility of off-the-shelf parts (be they commercial or military); and assessing system-level hardening in a realistic environment. After reviewing the facilities, methodologies, and expertise for bounding the threats due to TID, DDD, and electrostatic discharge, the committee believes that the test infrastructure for these effects does not experience the same level of strain and fragility as the infrastructure required for testing SEEs. Most

TID testing is done with gamma-ray sources, so the infrastructure requirements are not nearly as intensive as those for SEEs. A gamma irradiator can fit in a small room and does not require all the power, cooling, and other resources that a particle accelerator does. There are safety requirements, but these are manageable. SEEs are also less well understood. Depending on the technology of the affected device, SEEs can result in consequences ranging from self-recovering disturbance of device outputs to catastrophic failure of the device. The infrastructure is not under as much strain with the other threats as it is for SEEs and can meet the threats for the foreseeable future."

The finding of the U.S. committee that the radiation testing infrastructure is "fragile [..] already experiencing long wait times and rising testing prices, and it could easily suffer major strains if even a single major facility closes down suddenly" is a worldwide concern.

In December 2020T the G-RAD 2020 workshop (https://workshops.ill.fr/event/273/) which was organized "to put together testing facilities and radiation experts and stakeholders from industry and academia to stimulate discussion on current and future needs in radiation hardness testing and evaluate limitations of available radiation facilities and possible evolutions". The RADNEXT project (https://radnext.web.cern.ch/) funded by the European Commission in 2020 aims at addressing the user demand – facility availability issues ,"with the objective of creating a network of facilities and related irradiation methodology for responding to the emerging needs of electronics component and system irradiation; as well as combining different irradiation and simulation techniques for optimizing the radiation hardness assurance for systems, focusing on the related risk assessment".

The European Commission is now funding, in the Horizon Europe Framework Programme (HORIZON), among the topics of the call "Strategic autonomy in developing, deploying and using global space-based infrastructures, services, applications and data 2021", the "development of very high energy (>100MeV/nucleon, up to several GeV/nucleon) ion facilities in Europe for the tests of EEE space components, shielding and radiobiology, to experimentally simulate the cosmic rays environment for space applications" to limit the dependency for SEE testing with heavy ions to U.S. and Japan facilities.

1.2 PROTONTHERAPY ACCELERATORS AND RADIATION HARDNESS ASSURANCE (RHA)

Proton beams produced by particle accelerators are, together with heavy ions, the main radiation source in standard radiation hardness assurance protocols for single event effects in electronic components ((ESCC Basic Specification No. 25100 - SINGLE EVENT EFFECTS TEST METHOD AND GUIDELINES, 2014);((JEDEC Solid State Technology Association, 2013)). Proton beams are also a standard radiation source for Displacement Damage testing ((*ESCC Basic Specification No. 22500 - GUIDELINES FOR DISPLACEMENT DAMAGE IRRADIATION TESTING*, 2019)). Additionally, protons induce ionization (TID) and therefore, in principle, all radiation effects can be probed simultaneously with this radiation source.

Specialized facilities exist for proton and heavy ions radiation hardness assurance qualification. In Europe, the ESA has frame contracts with three facilities (UCL Belgium, PSI Switzerland, RADEF Finland) and other frequently employed facilities are KVI Netherlands, GANIL France and, to a limited extent, GSI-FAIR Germany and CERN, Switzerland.

In this framework, where the need for radiation testing increases but the number of available facilities does not, protontherapy centres can play a significant role. Proton therapy is an advanced radiotherapy technique: compared to traditional photon-based radiotherapy it allows higher conformation of the tumour volume and healthy tissues dose sparing. Unfortunately, the higher installation and running costs of the facilities have so far limited the availability of proton therapy.

Beam requirements for proton therapy largely superimpose with standard SEE high energy proton testing recommendations in terms of available particle energies, intensities and transverse homogeneity (that is, with respect to the beam direction) at the target position. For Displacement Damage testing, lower proton energies are typically employed, but with intensities about a factor 10 higher. From a beam delivery point of view, dosimetry prescriptions for patient therapy are even more stringent than for electronic equipment, thus resulting in well characterized and accurate irradiation.

While beam time availability for non-medical use is limited, typically on weekends only, the use of such facilities for electronic components testing is growing as more and more proton therapy centres enter operation stage (as tracked by the Particle

Therapy Co-Operative Group https://www.ptcog.ch/index.php/facilities-in-operation). This is especially true in the USA where SEE testing relies more and more on proton therapy facilities availability, as highlighted in the already cited (*Testing at the Speed of Light*, 2018). From the facility point of view, a synergy with the radiation hardness community might be beneficial since maximization of beam time usage is crucial in covering the hefty installation and running costs of the accelerator. A better understanding of the specific needs, methods and strategies of RHA with proton beams in commissioning or even design phase of accelerators for medical application could become increasingly relevant.

1.3 SUMMARY OF RADIATION EFFECT ON ELECTRONIC COMPONENT

Here we report a summary of the main effects of radiation on electronic components: cumulative (Total Ionizing Dose and Displacement Damage Dose effects) and stochastic (Single Event Effects). It is based on the RADECS 2019 short course notes, the paper (Ravotti, 2018) for Total Ionizing Dose effects and the PhD thesis (Ravotti, 2006) for Displacement Damage Dose and NIEL definitions.

1.3.1 TOTAL IONIZING DOSE EFFECTS

Regarding its effects on electronic materials and devices, an incident energetic particle impacting a target material loses its energy mostly via three main interactions: ionizing, non-ionizing, and radiative processes. This energy loss is expressed via the stopping power dE/dx. The total stopping power is therefore made of 3 contributions, each relative to one interaction process:

$$\left.\frac{dE}{dx}\right|_{total} = \left.\frac{dE}{dx}\right|_{el} + \left.\frac{dE}{dx}\right|_{nucl} + \left.\frac{dE}{dx}\right|_{rad}$$

Ionizing energy loss creates free charges, whereas non-ionizing processes generate atomic displacements.

When impacting a target material, ionizing radiation mainly generates electron-hole pairs. In a semiconductor material, such as silicon (Si), the main effect will be the occurrence of a transient parasitic photocurrent. In an insulator material, such as silicon dioxide (SiO2) of MOS technologies, some fraction of the electrons and holes can become trapped in the oxide, and some fraction can cause the release of hydrogen and induce interface traps at the Si/SiO2 interface.

The effects of ionization are generally estimated by the concept of Total ionizing Dose (TID), which measures the amount of energy deposited in the material. The official unit to quantify the total absorbed ionizing dose in a material is the Gray (Gy), corresponding to an energy of 1 J deposited per kg of matter. Historically, the space community is using another unit to express TID: the rad (for radiation absorbed dose), which can be converted easily: 1 Gy = 1 J/kg = 100 rad.

In the case of photons, this TID can be expressed by:

$$\boldsymbol{TID = \Phi_{ph} \cdot \left(\frac{\mu_n}{\rho}\right)}$$

where Φ is the integrated energy flux of incident photons (in MeV/cm²), and μ_n/ρ is the mass absorption coefficient (in cm²/g) of photons in the material.

For charged particles the dose to a thin object of a given material will depend primarily on the rate of energy loss of the particles in that material and their distribution across the beam. A thin material object is the one with thickness much smaller than the range of the charge particle in the material itself. The TID in Gy from protons and electrons can thus be calculated directly from the mass-collision stopping power and the fluence:

$$\boldsymbol{TID = K \cdot \Phi \cdot S/\rho} \qquad 1$$

where Φ is the particle fluence expressed in cm^{-2}, $K=1.602\times10^{-10}$ is a scale factor, and S/ϱ is the mass-collision stopping power, which has units of MeV·cm²/g. The mass collision stopping power is usually approximated as the Linear Energy Transfer (LET) which depends on the target material and on the particle's energy. Electronic stopping powers can be calculated for silicon, germanium, GaAs, and many compounds using the TRIM or SRIM code (Ziegler et al., 2010) or can be found from NIST tables (Berger et al., 2005).

1.3.2 DISPLACEMENT DAMAGE EFFECTS

In addition to ionization effects, high-energy electrons, protons, neutrons, and heavy ions can also cause displacement damage in silicon and other semiconductor materials, when the particle interacts with the nucleus of the atom, instead of the electron cloud.

With non-ionizing processes, the energy loss causes the atoms to be displaced from their equilibrium sites and can lead to lattice disorder. This is the primary interaction process for neutrons, which are charged neutral and do not interact with the electron cloud of an atom. This is also the case for part of the energy lost by electrons, protons, and heavy ions.

The amount of energy deposited per unit length in a material (from non-ionization processes) is given by its nuclear stopping power $dE/dx\ |_{nucl}$

The mass-stopping power is defined as the non-ionizing energy loss (NIEL), and is given by:

$$NIEL = \frac{1}{\rho}\frac{dE}{dx}\Big|_{nucl}$$

where ϱ is the density of the material and $dE/dx\ |_{nucl}$ is the rate of energy loss in the material from nonionizing processes. NIEL is expressed in units of MeV cm^2/g.

The NIEL for a given particle (electron, proton, heavy ion) depends on the target material and on the particle's energy. The Displacement Damage Dose (DDD) associated with an exposure to a given particle beam can then be calculated by multiplying the NIEL of the particle with its total fluence delivered.

$$\boldsymbol{DDD = NIEL(E) \cdot \Phi(E)} \qquad \mathbf{2}$$

where Φ(E) is the total fluence of particle at energy E, with NIEL(E).

1.3.2.1 THE NIEL HYPOTHESIS AND HARDNESS FACTOR

The basic assumption of the NIEL hypothesis is that any displacement damage induced change in the material scales linearly with the amount of energy imparted in displacing collisions, without taking into account the spatial distribution of the introduced displacement defects and the various annealing sequences taking place after the initial damage event. In this way the NIEL can be calculated and is expressed by the displacement damage cross section D(E). With the help of the displacement damage cross section D(E) it is finally possible to define a hardness factor κ allowing to compare the damage efficiency of different radiation sources with different particles and individual energy spectra Φ(E).

It is common practice to define the hardness factor κ in such a way that it compares the damage produced by a specific irradiation to the damage which would have been produced by monoenergetic neutrons of 1 MeV and the same fluence:

$$\boldsymbol{k = \frac{\int D(E)\Phi(E)dE}{D(E_n = 1\ MeV)\int \Phi(E)dE}} \quad \textbf{3}$$

Here, $D(E_n=1\ MeV)$ is set to 95 MeVmb (ASTM Committee, 1994). The equivalent 1 MeV neutron fluence Φ_{eq} can thus be calculated by:

$$\boldsymbol{\Phi_{eq} = k\,\Phi = k\int \Phi(E)dE} \quad \textbf{4}$$

and it is measured in 1-MeV neutron equivalent particles/cm^2 or simply (cm^{-2}). With the same approach, equivalent fluence for another particle specie and energy can be defined through hardness factor scaling.

1.3.3 SINGLE EVENT EFFECTS

Ionizing radiation mainly generates electron-hole pairs, which impact semiconductor materials, such as silicon (Si), by generating a transient parasitic current. A single particle (either neutron or proton and heavy ion) interacting with the semiconductor material can trigger different effects at device level. The manner in which the parasitic single-event-induced current evolves within semiconductor devices depends on the LET of the particle, on the location of the particle hit, on the device being struck, and on the bias applied to the device. For a single particle interaction with a microelectronic device, there are typically two types of ionizing mechanisms: the first is a direct ionization by the particle itself, if its LET is large enough to induce a perturbation of the device; the second is indirect ionization, coming from secondary particles created by nuclear reactions between the incident particle and the target material.

1.3.3.1 CHARGE DEPOSITION BY DIRECT IONIZATION

An energetic particle interacting with the semiconductor will generate free carriers and lose its energy along its path, until coming to rest in the material. The total distance the particle has travelled into the material is called the range. The LET is

the rate of energy loss per unit length (or electronic stopping power), for a given particle (electron, proton, heavy ion) it depends on the target material and on the particle's energy. Electronic stopping powers can be calculated for silicon, germanium, GaAs, and many compounds using the TRIM or SRIM code.

1.3.3.2 CHARGE DEPOSITION BY INDIRECT IONIZATION

Light particles such as protons and neutrons usually do not generate enough charge by direct ionization to cause SEEs (although we'll see that this tends to change with device scaling). However, high energy protons and neutrons can both still impact SEE sensitivity via indirect ionization mechanisms. When a high-energy proton or neutron enters the semiconductor lattice, it can trigger an atomic displacement, especially after an inelastic collision with a target nucleus. Different nuclear reactions may occur, including elastic collisions that produce Si recoils, emission of alpha or gamma particles and the recoil of a daughter nucleus, and spallation reactions in which the target nucleus is broken into two recoiling fragments. All these reaction by-products can then deposit energy along their paths by direct ionization: basically, these particles will then behave as "regular" heavy ions with a given LET and range, and will deposit charge along their path, as previously described. Being much heavier than the original proton or neutron, they can deposit higher charge densities and may thus trigger single-event effects.

When performing radiation experiments to characterize the sensitivity of a given device to any of the SEEs described, one measures the probability of error to occur in the device. This probability is measured as the cross-section for interaction with the impacting particle. The cross-section is simply defined as the ratio between the number of faults (upsets, errors, transients, etc…) with the total fluence of particle reaching the device and the total number of bits of the device:

$$\boldsymbol{XS = \frac{N_{errors}}{N_{bits} \cdot \Phi}} \qquad \textbf{5}$$

where N_{errors} is the total number of errors, Φ is the particle fluence (expressed in cm^{-2}), and Nbits is the total number of bits of the device. XS is therefore expressed in cm^2/bit. If the Number of bits is not relevant for the investigated Single Event Effect the cross section is measured as cm^{-2}/device. The measured SEE cross sections are commonly plotted as a function of the LET of the incident particle (for heavy ions) or as a function of the proton energy.

1.4 RADIATION SOURCE CHARACTERIZATION REQUIREMENTS FOR RADIATION HARDNESS ASSURANCE

Despite the differences in radiation effects that can be induced by ionizing particles, looking into equations 1, 2 and 5 for charged particles, the physical parameters relevant to quantitatively describe the imparted radiation are a limited set and common to all type of investigated effects.

These are

- The radiation specie
- Its energy spectrum
- Its fluence and flux on the target
- The composition of the target

Additionally, we must consider the homogeneity of these properties across the Device Under Test (DUT) area. It is thus non surprising that the radiation source characterization requirements by ESCC (and other institutions) can be summarized as follows

Table 1 Summary of dosimetry and beam characterization requirements extracted from ESCC specifications

Parameter	Description	Accuracy
Flux and fluence	Dosimetry shall allow the continuous monitoring of the flux and the fluence at the device throughout the test with an accuracy of ±10%	±10%
Energy spectrum	The energy of the beam in the active volume should be constant ±5% and the spread in the FWHM of the beam energy shall be less than ±10%	±10%
Homogeneity	The radiation field shall be uniform to ±10% over the area of the device(s) under test in terms of both fluence and energy	±10%

1.5 THE TOP-IMPLART PROJECT AND SCOPE OF THIS THESIS

Dosimetry concepts described in the previous paragraph also apply in proton (or particle) therapy: the concept of TID is equivalent to the concept of "Dose" used in radiotherapy and radiobiology and dose delivery from a monoenergetic particle beam is described by equation 1. As summarized for instance in (Schippers & Seidel, 2014) an accelerator facility for particle therapy implements a variety of

technical measures to ensure an accurate and reproducible dose delivery to patients. Clinical treatments require a ± 3% dose accuracy over a 3-dimensional, irregular volume of non-homogeneous density. The "building blocks" used to define a particle therapy treatment planning are particle beams of well-defined energy, varying intensities, and spot sizes. Monitoring of these quantities is mandatory and demanded to highly specialized subsystems in all radiotherapy facilities that verify the beam properties either online or periodically through the Quality Assurance (QA) procedures.

It is therefore reasonable to assume that monitoring and qualification techniques developed for protontherapy could be adapted to perform RHA test compliant with the requirements of Table 1. As each facility develops unique solutions to satisfy the clinical requirements, so will be the development of procedures to perform RHA irradiation in that facility.

Most proton facilities use a cyclotron as an accelerator, while proton-carbon ones employ a synchrotron. It is generally acknowledged, however, that more compact and efficient accelerators must be developed to reduce treatment duration (hypofractionation), improve dose delivery precision, and reduce costs, with the aim to make proton facilities more profitable, thus closing the gap with traditional x-ray machines.
High frequency pulsed LINear ACcelerators (LINAC) have been proposed, in the first nineties of the previous century (Hamm et al., 1991), (Nightingale et al., 1992) as possible compact, lightweight, and cost-effective solution. To this date, though, no such an accelerator is yet fully commissioned. Three simultaneous projects are developing a full-LINAC proton therapy accelerator: the TOP-IMPLART project funded by Regione Lazio, the ERHA system by the Italian private company LinearBeam and the LIGHT system by the former CERN spin-off company ADAM (now owned by the British company AVO).

The TOP-IMPLART project was funded by the innovation department of Regione Lazio in 2012 aiming at the construction of a novel, full-LINAC proton therapy accelerator which is presently under installation and commissioning in ENEA Frascati Research Centre. Since there is no fully linear proton accelerator in operation specifically designed for cancer treatment, the project funds both the accelerator and pre-clinical radiobiology campaign to demonstrate the reliability of the system. In particular, the beam monitoring techniques routinely applied in

cyclotron or synchrotron-based facilities must be adapted and validated to the specific properties of this beam source.
One of the peculiarities of the TOP-IMPLART accelerator is its intrinsically extendable modularity: it can deliver an exploitable beam any time while under construction. The immediate characterization and virtually continuous improvement of its performance is thus possible even for energies far from those suitable for therapy treatments. Following this approach, machine development in terms of energy upgrade, stability and repeatability control, has been complemented by both dosimetry and radiobiology experiments that validate the quality of the beam. Experimental activity is mainly focused on the development of a dedicated dose monitoring system, tailored to the high instantaneous dose rate of the TOP-IMPLART accelerator, and characterization of the machine properties in terms of reproducibility and stability even at pre-clinical energies (i.e. below 60 MeV).

As proton LINACs aim at providing an alternative to cyclotrons and synchrotrons in the cancer therapy domain, they could be a meaningful alternative for radiation testing. In the framework of this PhD thesis activity with Università La Sapienza, we investigated the possibility to apply the beam delivery competences developed for pre-clinical studies to test components designed for space applications.

The beam monitoring and delivery strategies implemented so far during the TOP-IMPLART commissioning were aimed at radiobiology experiments on cell cultures. For these experiments, passive beam delivery is adequate thanks to the simple geometry of the target, that can be described as a 2D object of homogeneous material and regular shape. Passive beam delivery methods exploit increase of transverse dimension of the pristine proton beam by diffusion in air and scattering through thin layers of high Z materials, possibly followed by a collimator to conform the beam to the target 2D transverse profile. In these applications no intensity variation is required and the accelerator delivers a fixed proton current level.

The strong similarities in the typical irradiation geometries between electronic components and in vitro radiobiology suggests that the already available delivery strategies could be successfully adapted to radiation hardness qualification. While typical radiobiology experiments verify the accelerator and monitoring system behaviour in low-current, short-duration irradiation configuration, electronic

components irradiation will also require high-current, long-duration irradiation. RHA activities will therefore constitute complementary activities in assessing the accelerator and beam monitoring equipment reliability in a broader spectrum of operation set-ups.

Passive delivery was the first clinical method employed in proton therapy in the 1960s and it is still used today, though it is surpassed by the clinically superior, but technically more complex, active scanning technique. Active beam scanning employs directly the pristine beam but requires deflecting magnets, fast variation of the extracted proton current and a complex control system. This method will be tested at ENEA Frascati once the TOP-IMPLART accelerator reaches clinical energies.

The TOP-IMPLART project aims at demonstrating active delivery with a full-LINAC accelerator. For this reason, the currently implemented passive delivery is only a first step in the clinical qualification, whereas the already developed passive delivery scheme could possibly have achieved an already significant maturity level for electronic components qualification.

In this thesis, we aim at assessing the present delivery and monitoring capabilities of the TOP-IMPLART accelerator in the light of the ESCC prescriptions for standard irradiation procedures. In particular, we will discuss the capability of our delivery system to provide a continuous monitoring of the proton flux and fluence with an accuracy of at least ± 10% in ranges relevant for RHA applications. This, coupled with a characterization of the beam parameters (energy, energy spectrum, transverse uniformity) at the target position with the same accuracy, shall fulfil the typical prescription of standard procedures for electronic components irradiation.

The research activity is structured as a series of irradiation campaigns on devices considered representative of different radiation hardness tests that can be performed with protons: displacement damage effects, single event effects and system level qualification where cumulative and stochastic effects are probed simultaneously. Whenever possible, tests are conducted on reference devices whose response is known either from literature or from previous irradiation data. Each experiment comprises the identification of an irradiation set-up, its full characterization and the beam and device monitoring strategies. Results are discussed in terms of lesson learned, aiming at constantly refining the methodology to better comply with the ESCC prescriptions and streamline the

accelerator set-up process, balancing the accuracy requirements and the need for complex beam measurements. Finally, research activities on the development and commissioning of a new beam current monitor and on the integration of existing devices into the accelerator control system are presented, highlighting their impact on future RHA test campaigns.

This is the outline of the thesis:

- *The TOP-IMPLART project and proton LINAC*:
  an overview of the design principle, layout and commissioning results for the TOP-IMPLART proton accelerator; the beam monitoring devices routinely employed for both the accelerator commissioning and irradiation activities

- *A p-i-n diode online dosimetry system for Displacement Damage measurement*:
  it is based on a cheap, COTS component whose applications have been investigated at CERN since the early nineties and is now routinely used also in other laboratories; it was considered a good candidate for a first "case study" to test our beam qualification system through comparison with existing literature data on this device radiation response and develop an alternative dosimetry system specifically dedicated to radiation hardness tests.

- *Radiation testing of a 6-axis MEMS Inertial Navigation Unit with protons and x-rays:*
  an irradiation campaign of a COTS product where cumulative and stochastic effects were investigated over increasing level of radiation exposure. The inertial measurement unit which combines the sensors and the control ASIC on a single chip is an example of a complex device. The radiation testing single-event effect (SEE) and total ionizing dose (TID) standards developed by the community are in a continuous struggle when it comes to keeping up with the innovation introduced by brand new devices (e.g., flip-chips, multiple chips stacked within the same package, 3-D layouts) which outperform those devices the standards were tailored for (Coronetti et al., 2021). A "system level" radiation testing approach was selected: it can be cost effective tool for a space system for which the risk

associated with a lower level of assurance can be accepted. Comparison of irradiation with proton beam and x-rays (produced by another facility within the ENEA laboratory) is also presented.

- *SEU measurements with ESA Monitor*

  this irradiation campaign was a collaboration with CERN R2E (Radiation to Electronics) group. The specific project was devoted to the comparison of proton and neutron induced Single and Multiple Event Upsets susceptibility of different SRAMs, including both commercial products and radiation tolerant devices For the ENEA laboratory the collaboration provided the opportunity to test our dose delivery system accuracy with the ESA monitor, which acts as a cross reference tool between European facilities, and, through the interaction with the CERN colleagues, to develop internal procedures and adopt best practices apt for planning and execution of "standard" RHA irradiation campaign for Single Event Effects.

- *Evolution of the TOP-IMPLART beam monitoring system:*

  in this final chapter we present a series of activities related to the evolution of the TOP-IMPLART beam monitoring system. These include the commissioning of a new beam current monitor and the actions to integrate existing devices into the accelerator control system. The aim of these actions is to overcome the limitations, highlighted in the experimental irradiation activities reported in the previous chapters, of an online monitoring system so far based solely on integral ionization chambers. More specifically we describe the new online control system of the 2D ionization chambers, cross calibration activities of the 2D ionization chamber with the existing beam current monitor and the commissioning of a new, passive RF cavity based current monitor. Advantages of the new monitoring system specifically for RHA testing purposes is discussed.

Finally, the last part of the thesis, consisting of the *Conclusions* chapter is devoted to discussing and resume the main achieved results, to propose some additional considerations and to provide comments on possible development for future studies in the field. Also, the section *Appendix* supplement the thesis by including more in-depth information about the implemented technical solutions.

Chapter 2
THE TOP-IMPLART PROJECT AND PROTON LINAC

The ENEA Frascati Particle Accelerators and Medical Applications Laboratory has a long standing in the development and prototyping of linear accelerators as radiation sources in a wide range of technological applications. Presently, two accelerators are in operation: the TOP-IMPLART proton linac, which is in the commissioning stage, and the REX (Removable Electron X-rays) facility based on a S-band linear accelerator which can provide electron beams up to 5 MeV and bremsstrahlung X-rays beams via a conversion head with tungsten target.

In this chapter we provide an overview of the design principle, layout and commissioning results for the TOP-IMPLART proton accelerator. Beam monitoring devices routinely employed for both the accelerator commissioning and irradiation activities are presented.

2.1 PROTONTHERAPY AND THE TOP-IMPLART PROJECT

Radiation therapy is one of the cornerstones of cancer treatment. The exposure of tumour tissues to ionizing radiation induces unrecoverable damage to DNA of the cancerous cells, leading to their death. Photons and heavy charged particles (hadrons) are the most used radiation sources. X rays represent the most widespread choice since they can be easily produced from compact and cost-

effective electron accelerators. Photons, however, lose their energy in matter as a function of the penetration depth in an exponentially decreasing fashion. This implies that the target must be irradiated from multiple directions, in order to reduce the dose released to surrounding healthy tissues while keeping constant the one delivered to the tumour. In this regard, hadrons present some advantages over x rays. The energy deposition curve exhibits a small amount of energy lost when the particle velocity is high (entry channel), while most of it is lost in a narrow portion of the path, the so-called Bragg peak, close to the end of the particle range. Moreover, hadron beams are characterized by a lower lateral scattering with respect to x rays, resulting in a more conformal irradiation of the tumour volume. Despite the recognized therapeutic benefit, the complexity, dimensions, and costs (e.g., construction operation and maintenance) of the facility have hindered a large-scale diffusion of particle therapy centres, until progress in accelerator technologies and treatment plan implementation has changed course. Nowadays, there are 109 particle therapy facilities worldwide, 12 of which also use carbon ions (https://www.ptcog.ch/index.php/facilities-in-operation, December 2021) and they all rely on circular machines to accelerate particles. Most proton facilities use a cyclotron as an accelerator, while proton-carbon ones employ a synchrotron. It is generally acknowledged, however, that more compact and efficient accelerators must be developed to reduce treatment duration (hypofractionation), improve dose delivery precision, and reduce costs, with the aim to make proton facilities more profitable, thus closing the gap with x-ray machines.

At the beginning of 1990s (Hamm et al., 1991), (Nightingale et al., 1992) high frequency pulsed linear accelerators have been proposed as possible compact, lightweight, and cost-effective solution for proton therapy thanks to the small dimensions of the accelerating structures and to the use of commercially available RF power sources. In a comprehensive study, reported in (Amaldi et al., 2009), two different approaches were suggested: a hybrid cyclotron-linac (the so-called Cyclinac (Amaldi et al., 1998)) and a fully linear accelerator. The former consisted of a 62.5 MeV cyclotron injector feeding an L-band (1.28 GHz) linac booster, reaching a final energy of 200 MeV. The latter, instead, exploited a typical sequence of accelerating structures for proton linacs: a proton source; an UHF (499.5 MHz) Radio Frequency Quadrupole (RFQ) pre-accelerator; a Drift Tube Linac (DTL) operating at the same frequency (up to an energy around 70 MeV); and a sequence of Coupled Cavity Linacs (CCL), operating in the microwave S-band (2.997 GHz), to a final energy between 230 MeV and 250 MeV. Following this approach, in 1995

ENEA patented a 200 MeV fully linear compact proton accelerator (Picardi et al., 1995). It employed a novel and lightweight S-band accelerating structure named Side Coupled Drift Tube Linac (SCDTL) to be used for particle energies between 5 MeV and 65 MeV.

In 2012 the Innovation Department of Regione Lazio approved a project named TOP-IMPLART (Terapia Oncologica con Protoni - Intensity Modulated Proton Linear Accelerator for Radio Therapy) (Ronsivalle et al., 2011), with the aim to realize and validate a prototype of linear accelerator, built with SCDTL technology, dedicated to proton therapy. The accelerator is under development at the ENEA research centre in Frascati, in collaboration with the Italian Institute of Health, and the Oncological Hospital IFO. Following the criteria presented in the original patent, in the actual design SCDTL modules constitute the accelerating sections between 7 MeV and 71 MeV.

The use of high frequency proton linacs has several advantages over circular machines. For instance, the output charge rate can be flexibly and actively varied (i.e. without the use of degraders and collimators) either changing the injector current, shortening the current pulse duration or changing the optics parameters in the injection line. Output energy can be varied switching off some of the modules and adjusting the RF power level in the last one (as described in (Amaldi et al., 2009), (Ronsivalle et al., 2011)). Thus, intensity and energy could be changed ideally at each pulse (i.e. every 5÷10 ms), resulting in a fast and effective modulation of the output beam. In the clinical practice, this allows to move from one tumour slice to the next much faster than the several hundreds of milliseconds needed by circular machines, provided that the magnetic elements of the transport line and gantry can react at the same velocity. Moreover, linear accelerators can achieve very low beam emittance (rms normalized 0.2 π mm-mrad in TOP-IMPLART, or even better with a lower emittance injector). This allows smaller apertures for magnets and considerably reduces the weight of the gantry. As far as the radiation protection is concerned, the use of linear accelerators is less demanding since the radiation losses occur at low energy.

The TOP-IMPLART project foresees a proton final energy of 150 MeV (phase 1, funded with 11 M€), limited by the maximum bunker length available (30 m) at Frascati site (where clinical experimentation is not allowed), with the possibility to upgrade the machine to 230 MeV directly in the hosting medical centre (phase 2). Nevertheless, 150 MeV proton beam has sufficient penetration depth to treat at

least half of all lesions eligible for proton therapy (including ocular melanoma, head - neck and paediatric tumours).

2.2 ACCELERATOR DESCRIPTION

The TOP-IMPLART accelerator is designed to produce a proton beam, emitted at high repetition frequency pulses (100-200 Hz), whose characteristics (position, energy and intensity) can be varied actively (i.e. without the use of degraders and collimators) from pulse to pulse. The short pulse width (~ 3 μs) and high repetition rate make the beam time structure similar to the electron LINACS employed for conventional radiotherapy. Presently the maximum repetition frequency is limited to 50 Hz. The maximum beam current obtained in the commissioning of the accelerator is 30 μA at 55 MeV, three times higher than the upper clinical requirement.

2.2.1 ACCELERATOR LAYOUT

The TOP-IMPLART linac is constituted by a 7 MeV commercial injector (Duoplasmatron Source, RFQ and DTL) produced by ACCSYS-Hitachi (PL7 model) operating at 425 MHz (Picardi et al., 2000), and a high frequency linear accelerator operating at 2997.92 MHz completely designed by ENEA. This latter segment is composed by SCDTL structures up to 71 MeV and CCL structures up to 150 MeV. A Medium Energy Beam Transport line (MEBT) with four electromagnetic quadrupoles is placed between the injector and the first SCDTL module; it also includes a 90° magnet that can deflect the beam in a short vertical beam line dedicated to radiobiology experiments. A schematic layout of the TOP-IMPLART linac is shown in Figure 1.

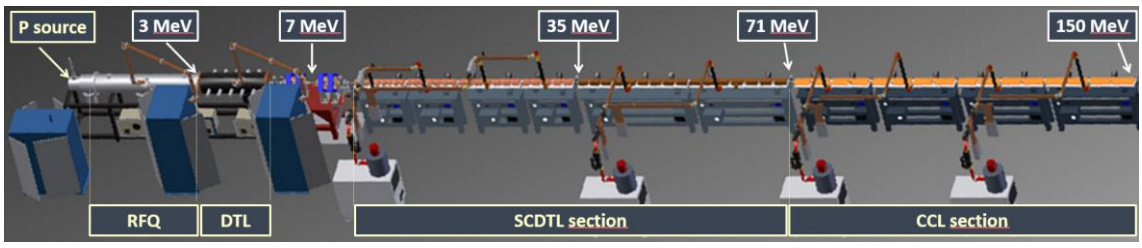

Figure 1 Schematic layout of the TOP-IMPLART accelerator

2.2.1.1 INJECTOR

Figure 2 The PL-7 injector installed in the Frascati bunker

The injector, originally designed for radioisotopes production, consists of a 2.3 m long RFQ and a 1.5 m long DTL. The protons are extracted from a Duoplasmatron source (with a maximum extraction voltage of 30 kV) and are focused by an einzel lens into the RFQ. The RFQ accelerates the beam up to 3 MeV and the DTL up to 7 MeV.

A copper aperture is inserted to limit the proton source current (10 mA) to a maximum value of 1.5 mA. The current from the injector can be varied either controlling the extraction voltage, or the einzel lens voltage. The injector control electronics provides feedback loops in the source and in the RF amplifier to stabilize the output beam. The RF amplifier of the RFQ and DTL operates in closed loop with active feedbacks on amplitude, frequency and phase.

2.2.1.2 MEBT & VERTICAL LINE

A transport line with four quadrupoles matches the 7 MeV beam in the transverse planes to the following accelerating structure; an adequate space between the two

couples of quadrupoles is left in order to include a 90deg vertical bending magnet required extract the beam on the so-called Vertical Extraction Line, originally designed as a facility for radiobiology. The vertical (upward pointing) beam is especially suited to irradiate cells deposited on very thin Mylar films where Mylar constitutes the bottom of a Petri dish. This arrangement allows disregarding the cell distribution deformation due to the gravity in horizontal beam arrangements. Nevertheless, the vertical line can also be employed for other low energy applications, such as Proton Induced X-ray Emission (PIXE) analysis which is an advanced diagnostic technique employed in fine arts ((Vadrucci et al., 2017)). The energy range on the vertical extraction line is 3 to 7 MeV: the minimum energy is obtained powering only the RFQ and transporting the beam in the DTL; intermediate energies 3 to 7 MeV, are achieved by varying the relative phase and/or the input rf power level of the DTL and selected thanks to the 90° dipole magnet which acts as a spectrometer.

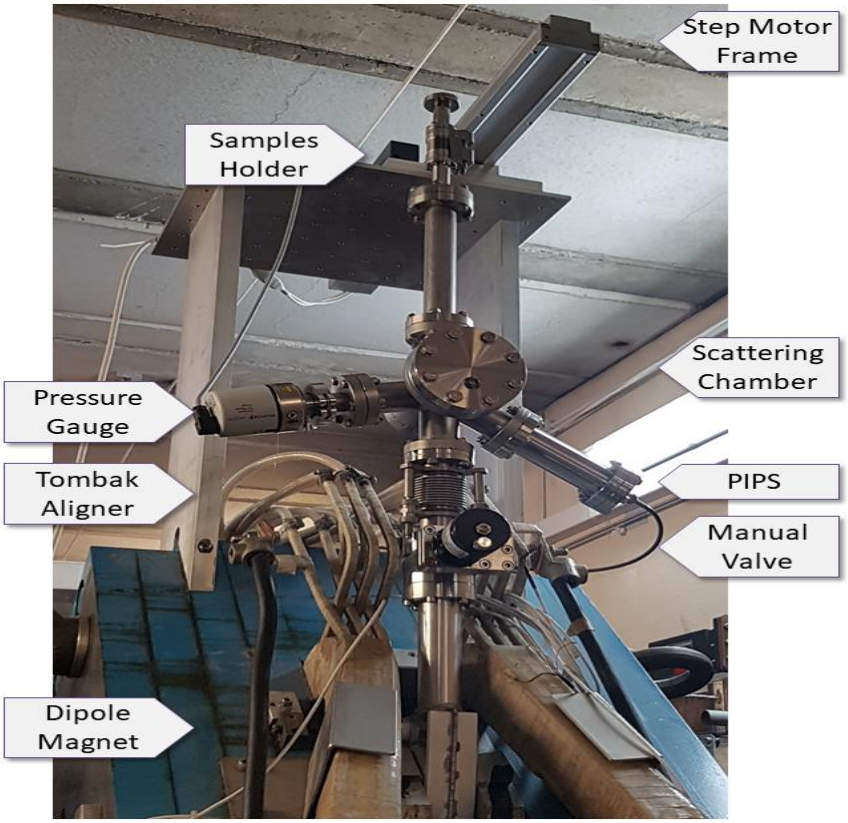

Figure 3 Vertical extraction line

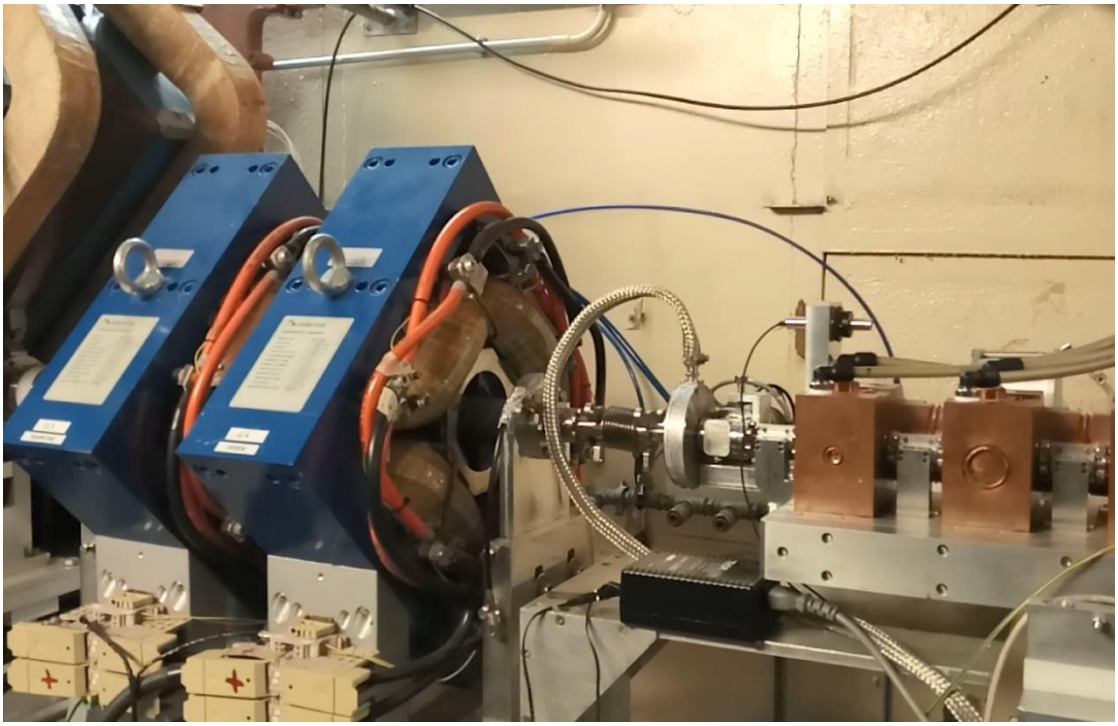

Figure 4 Medium Energy Beam Transfer line

2.2.1.3 HIGH FREQUENCY SECTION (SCDTL & CCL ACCELERATING STRUCTURES)

The SCDTL accelerating structure was developed by ENEA (Picardi et al., 1995) to satisfy the requirement of a high shunt impedance in the low-beta part of the TOP Linac; it compacts UHF-DTL structures typically used in proton linear accelerator medium-energy sections with the aim to make them work at frequencies as high as 3 GHz. The corresponding reduction of the structure axial hole for beam transport, from centimetre size to millimetre size, is compatible with the very low currents required by proton therapy. Obviously, the reduction in size of the drift tubes prevents the accommodation of the permanent magnet quadrupoles (PMQs) inside them. The accelerating action of the DTL tanks has therefore been spatially separated from the focusing action by splitting DTL tanks in smaller units and placing PMQs in the intra-tank space. The tanks are rf coupled together by side coupling cavities, explaining the name SCDTL. They are grouped in modules of about 1.5 m length to optimize their mechanical fabrication and installation in the accelerator site. The tanks belonging to the same module have similar internal geometry and the same number of drift tubes. The cells inside a tank (i.e., the

distance between the middle of two neighbouring drift tubes) have the same length $\beta\lambda$, where β corresponds to the average velocity value for that tank.

The analysis in terms of accelerating efficiency of the high frequency structures used in the TOP-IMPLART scheme shows that SCDTL can be usefully employed in the energy range between a few MeV up to roughly 80 MeV. Below this energy, the other competing structure, the CCL composed by side coupled cavities with $\beta\lambda$=2 cell length, has a cell length too short compared to the cavity diameter. This geometry reduces the shunt impedance of the structure and, hence, its efficiency. Above this energy, DTL-like structures show a strong reduction of the average gradient due to the larger cell length $\beta\lambda$.

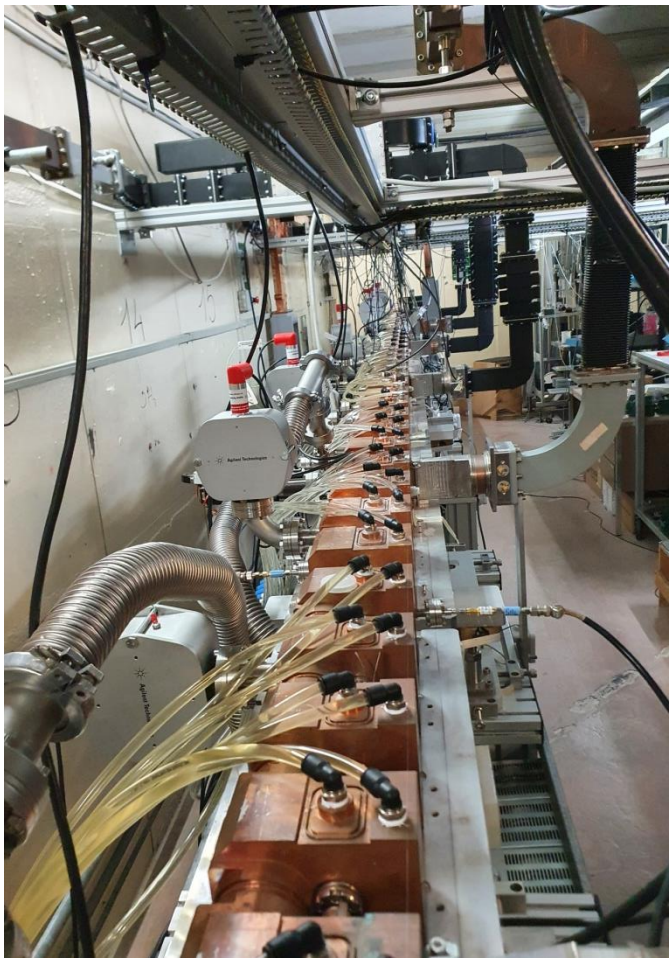

Figure 5 Top view of the SCDTL accelerating structures

For the above considerations, the 3 GHz accelerating section consists of SCDTL-type structures up to 71 MeV and Cavity Coupled LINAC (CCL) modules up to 150 MeV and, potentially, up to 230 MeV.

2.2.1.4 RF SYSTEM

The accelerator RF system works in pulsed mode. The pulse length is 15 μs – 80 μs for the injector and 1 μs – 4 μs for the high frequency linac. The maximum repetition frequency is currently designed to be 100 Hz, mainly due to the limits of the injector currently in use. A single FPGA-based timing unit synchronizes injector and booster operation, generating a set of triggers with a jitter below 10 ns. The availability of off-the-shelf proton injectors working at 425 MHz and of standard European S-band (2998.5 MHz) klystrons and RF components already procured in the past led to a RF frequency for the injector that is not a sub-harmonic of the SCDTL/CCL one. This implies that there is no longitudinal matching between low and high frequency modules, leading to large particle losses at 7 MeV in the first SCDTL module.
Nevertheless, the injected current is sufficient to produce a current at the output of the high frequency linac much larger than what is required for proton therapy. Moreover, the beam losses rise no particular concern as to radiation protection limits since they all occur at low proton energy.
The high frequency power part foresees the use of several identical RF plants each based on a 10 MW klystron and its power supply (modulator). In each RF unit the power is split in 4 for the SCDTL sections and in 3 parts for the CCL sections up to 150 MeV. Four such plants will therefore be necessary to supply the 7-150 MeV section of the TOP-IMPLART accelerator.
The RF split in 4 branches is achieved as follows: a first split in two by means of a commercial [Mega Industries, LLC] variable power divider with a power range between -0.1 dB and -30 dB composed by a sequence of a 3 dB hybrid, a phase shifter and another 3 dB hybrid; a second level of splitting is obtained by two home-made, very efficient riblet-based splits the first delivering power to SCDTL-1 and 2 and the second to SCDTL-3 and 4. Several -55/-60 dB calibrated directional couplers are placed in the RF line to retrieve information on the phase and amplitude of the signals driving the structures, and thus allowing the implementation of a stabilization loop. Each structure is also provided with a cavity field sensor and a motor actuated tuner for frequency control.

In Figure 6 the layout of the first RF power module feeding the 4 SCDTL structures is shown.

The RF amplitude and phase stability requirements of the accelerating field are within ±2% and ±2 degrees respectively. The SCDTL structures have typical a QLoad factor between 3500 and 5000, therefore a ±2 degrees phase tolerance corresponds to a request of frequency stability within ±10 kHz. Thermal dilation effects on copper in the 3 GHz frequency range may induce detuning of the order of 50 kHz /°C. To this end each SCDTL module is provided with a thermo-controller based on Peltier elements that keeps the temperature at the proper value with a ± 0.02 °C stability in stationary conditions.

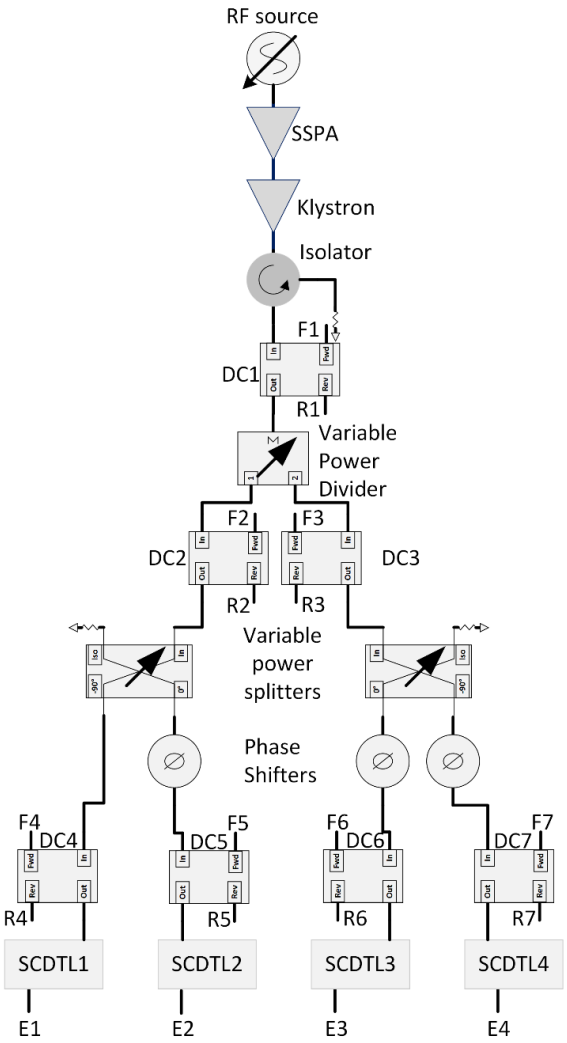

Figure 6 RF distribution to SCDTL structures

2.2.2 35 MeV ACCELERATOR CONFIGURATION

The successful commissioning of four SCDTL modules from 7 to 35 MeV, powered by a single 10 MW klystron, has a crucial importance for all proton therapy linacs. In fact, it constitutes the demonstration that this type of structures can be employed as building blocks of a high frequency linear accelerator for cancer therapy applications as was demonstrated in (Picardi et al., 2020). One of the peculiarities of the TOP-IMPLART accelerator is its intrinsically extendable modularity: it can deliver an exploitable beam any time while under construction. The immediate characterization and virtually continuous improvement of its performance is thus possible even for energies far from those suitable for therapy treatments. Following this approach, machine development in terms of energy upgrade, stability and repeatability control, has been complemented by both dosimetry and radiobiology experiments that validate the quality of the beam, and testing and calibrating specific instrumentation for pulsed beams (large instantaneous dose rate even at low average dose rate). Efforts were addressed at optimizing the beam parameters such as stability or homogeneity with a view to its use in radiotherapy applications.

The 35 MeV configuration has thus been extensively investigated, and it is furthermore the accelerator set-up relevant for the irradiation activities presented in this thesis. Here are therefore reported the 35 MeV proton beam main characteristics and the beam monitoring equipment.

2.2.3 35 MeV BEAM CHARACTERISTICS

TOP-IMPLART pulsed beam reaches an energy of 35 MeV at the exit of SCDTL4 with a maximum repetition rate of 50 Hz, the repetition frequency being manly limited by the older injector equipment. The peak pulse current (flat-top) ranges between 0.5 μA and 50 μA. After the titanium vacuum window, the beam spot is very small (< 5 mm in both x and y directions), with a vertical elliptical shape consistent with the FODO periodicity of the Permanent Magnet Quadrupoles. Figure 8 35 MeV extracted beam: pulse profile (left) and spot imaging (right)Figure 8Figure 7 shows the typical beam current profile and the beam spot imaging obtained on an alumina disk. Beam characteristics are summarized in Table 2.

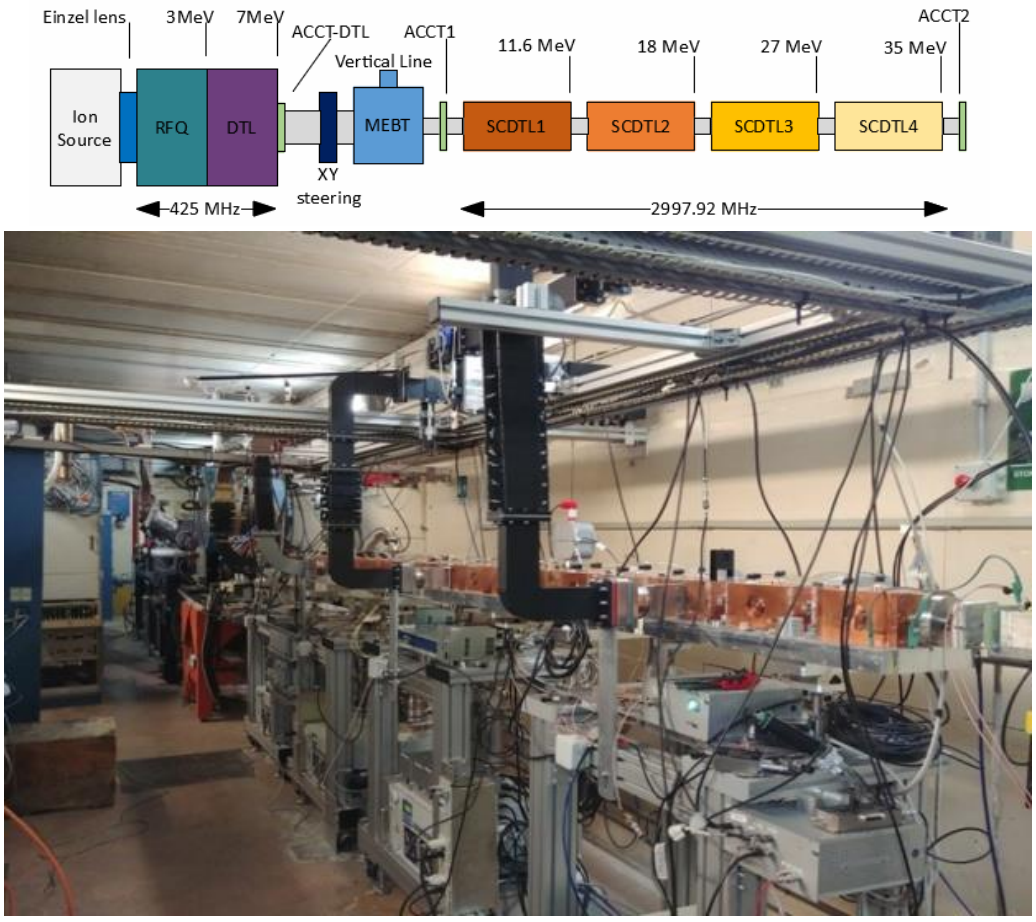

Figure 7 Schematic layout (top) and picture of the TOP-IMPLART accelerator installed and commissioned up to 35 MeV

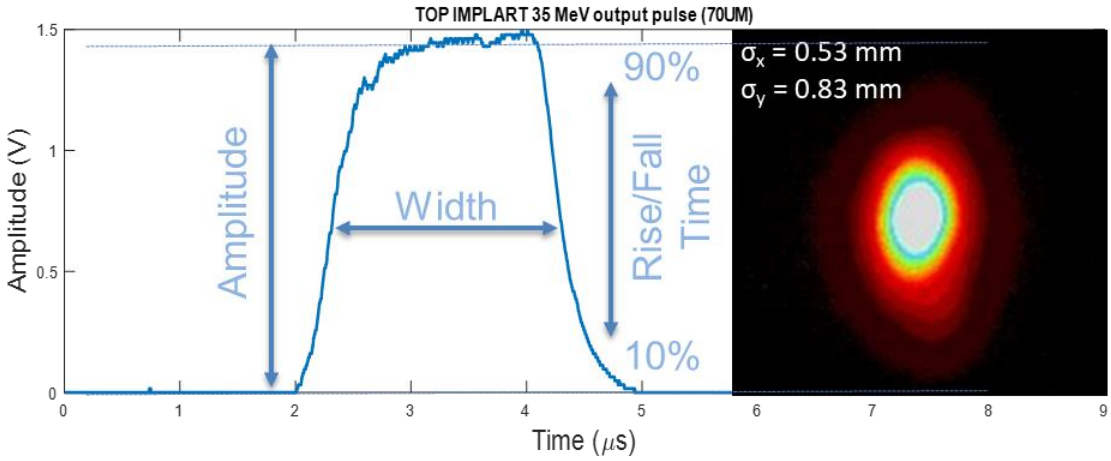

Figure 8 35 MeV extracted beam: pulse profile (left) and spot imaging (right)

Table 2 35 MeV extracted beam parameters (at SCDTL4 exit)

Parameter	Value	Unit
Pulse width	1 – 4	μs
	2.7 (typical)	
Pulse Repetition Frequency	100 (max)	Hz
	25 (typical)	
Peak current	50 (max)	μA
Charge per pulse	135 (max)	pC
Protons per pulse	8.4 10^8(max)	p
Spot size	0.5 (σ_x)	mm
	0.8 (σ_y)	

2.3 BEAM MONITORING

Different monitoring devices, both interceptive and non-interceptive, provide online measurements of the beam position and intensity. For the purposes of this work, we will only focus on a set of detectors used for beam characterization at the exit of the last SCDTL module, set-up and operation for irradiation procedures.

An AC current transformer (ACCT) is installed after SCDTL4 and operated in air. It is followed by a small, thin Ionization Chamber (IC) a Faraday Cup (FC) and a fluorescent screen coupled with a CCD camera. Except for the fluorescent screen, which is the only detector dedicated to profile measurement, the other devices can be used simultaneously for comparative measurement of the beam intensity and stability.

The beam current in the first SCDTL section ranges between 50 μA, for commissioning purposes, and 1 μA, for radiobiology experiments and, eventually, patient treatment, close to the sensitivity and resolution limit of the ACCT. Measurement of proton beam current and charge includes two different types of diagnostics, optimized for different current ranges. The first type, typical of the accelerator field, is based both on non-interceptive (current transformer) and interceptive (Faraday Cup - FC) monitors. These devices are sensitive in the beam current range of 5-50 μA. At lower intensities (which are typical of radiobiology and radiotherapy applications), dedicated detectors for radiation dosimetry (ionization chambers) have been implemented. These are specifically designed to control the delivered dose also on a pulse-by-pulse basis. The integral IC (IC) ionization chamber has been developed for the monitoring of the single pulse

beam charge, down to 1 pC/pulse (Cisbani et al., 2016) and is used as fast and sensitive beam charge monitor in air. Its readings are periodically compared against the Faraday Cup: at fixed position (and constant beam transverse size) the charge collected by the IC is linearly proportional to the single pulse beam intensity in the 1 – 116 pC range.

2.3.1 HIGH CURRENT DIAGNOSTIC TOOLS

The main diagnostic tools used in the actual TOP-IMPLART accelerator have been shown in the schematic layout of Figure 7. The beam current at the entrance and at the exit of the high frequency linac is measured by two identical AC current transformers (referred to as ACCT1 and ACCT2 in Figure 7). These are produced by BERGOZ Instrumentation, equipped with calibrated amplifiers to obtain an overall gain of 1V/mA over a 1MΩ load, with a negligible droop for μs-duration pulses. The output transformer is placed in air and can be moved following the accelerator assembly progresses. The length and the bore hole diameter (20 mm and 6 mm respectively) have been realized according to ENEA specifications, to fit in the linac available space.
The beam current is also measured by a custom designed Faraday cup. The signal generated by the Faraday cup is amplified by a FEMTO DHPCA-100 current amplifier, configured for a nominal transimpedance gain of 10^4 V/A on a 50 Ω load. The actual gain accuracy is ±1%.

2.3.2 HIGH SENSITIVITY CHARGE DETECTORS

Two thin integral ionization chambers and one multistrip chamber (IC_2D), that measures beam position and intensity profile of each beam pulse, are specifically designed and developed for TOP-IMPLART beam. These are high sensitivity devices able to detect charge as low as 1 pC/pulse. The two integral chambers operate at a bias voltage of 250 V (variable) and are realized with aluminized mylar electrodes (12 μm mylar, 4 μm aluminium) spaced by 2 mm of air. They have different geometries and mechanical supports: ionization chamber 1 is designed to fit at the exit of the beam pipe (Figure 9 a and b), while ionization chamber 2 can be placed anywhere along the beam axis beyond the accelerator exit in air (Figure 9 c and d).

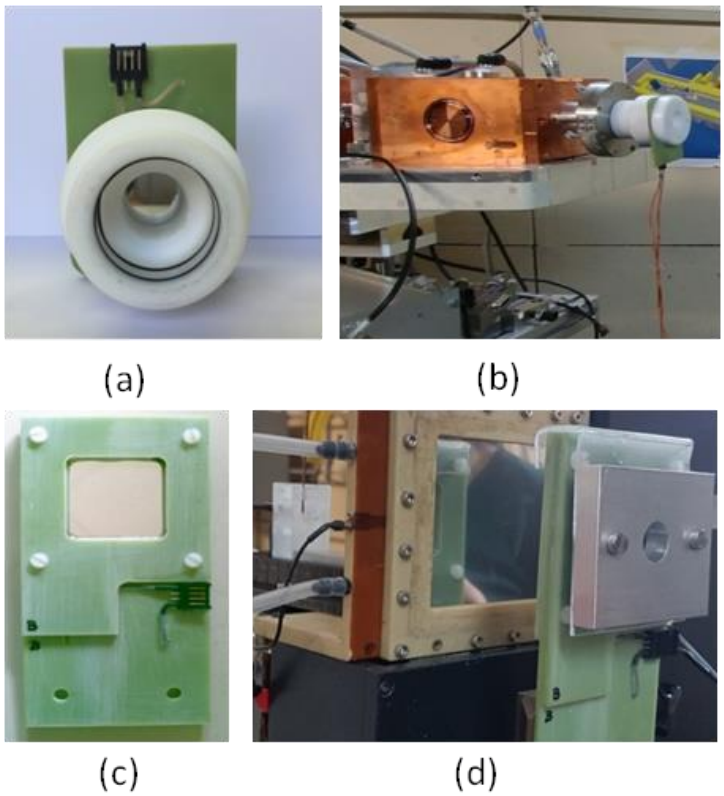

Figure 9 (a) Ionization chamber 1, (b) IC 1 mounted at the exit of SCDTL-4 after ACCT2, (c) Front view of ionization chamber 2, (d) IC 2 mounted after a collimator during an irradiation session at the end of the beamline in air.

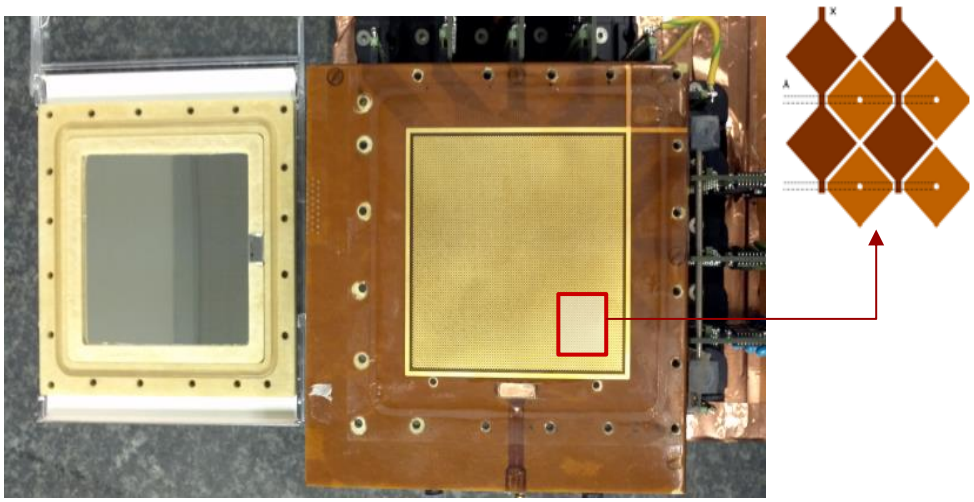

Figure 10 Multistrip IC-2D chamber prototype components: (left) the anode aluminized mylar window glued on the glass fibre epoxy Permaglas frame; (centre) the segmented cathode made by a layer of kapton and copper pads connected by strips along x and y (upper-right drawing).

The IC_2D ionization chamber, shown in Figure 10, is made of a highly segmented strip-like cathode that exploits the micro-pattern technology
The chamber measures the single beam pulse intensity profiles simultaneously along x and y axes, with spatial resolution at the level of 0.3 mm (strip pitch 0.875 mm), with a sensitivity of 100 fC and a dynamic range larger than 10^4. This is obtained by means of dedicated electronics, that automatically adapts the gain on each segment (channel) according to the amount of collected charge.

2.3.3 BEAM TRANSVERSE IMAGING

The on-line imaging of the beam spot is performed with an alumina fluorescent screen, placed after the vacuum window, and a Basler ACE camera with a monochrome 12-bit CCD sensor, used to digitally acquire the spot position and size. The CCD sensor size is 3.7 mm x 2.8 mm with a pixel dimension of 5.6 μm x 5.6 μm. The camera is hardware triggered for synchronous acquisition and exposure control.

2.3.4 BEAM IMAGING AND ENERGY MEASUREMENT WITH PHOTOLUMINESCENCE OF COLOUR CENTRES IN LIF CRYSTALS

Commercially available (10x10) mm^2, 1 mm thick polished lithium fluoride (LiF) crystals are used as passive detectors for proton beam imaging (Piccinini et al., 2019). Protons lose energy in the crystal and create F_2 and F_3^+ aggregate colour centres, stable at room temperature, which emit red and green photoluminescence (PL), respectively, under optical excitation in the blue spectral range. By using a fluorescence microscope equipped with a camera, the visible fluorescent proton beam transversal spatial image stored in the irradiated LiF crystal is acquired. Their photoluminescence intensity has been found to be directly proportional to the dose absorbed by the LiF material over at least three orders of magnitude up to 105 Gy.
This property allows multiple beam diagnostic procedures: dose measurement, transverse beam spot imaging and dose depth distribution measurement. When the LiF crystal is positioned with the polished faces parallel to the beam propagation direction, (see Figure 11), as the PL intensity is proportional to the energy lost by protons in the crystal, the beam energy is obtained by comparing

the measured distance between the crystal edge and the PL intensity. Thanks to the LiF crystal high intrinsic spatial resolution, micrometric precision in the Bragg curve imaging is obtained. An analytical model of the LiF crystal response allows reconstruction of the spectral content (Nichelatti et al., 2019) . This technique is used in the accelerator commissioning to validate numerical calculation of the beam energy both in vacuum and after transport through matter.

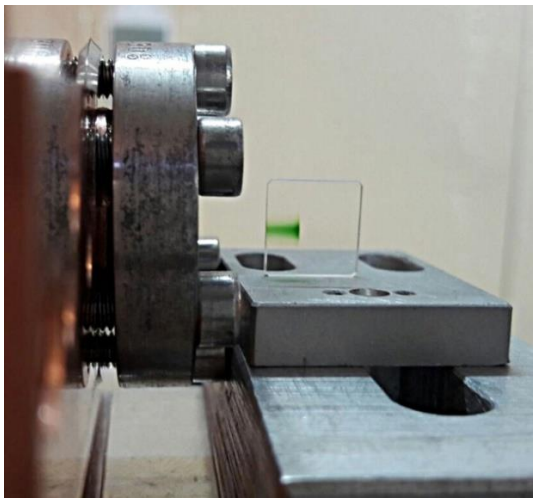

Figure 11 LiF crystal positioned after the current monitor ACCT2 with the polished faces parallel to the beam propagation direction just after proton irradiation. The green coloration, observed by naked eye, is due to the broad absorption bands of proton-induced aggregate colour. centres.

2.4 BEAM CHARACTERIZATION AT THE TARGET POSITION

Since an active scanning system is not yet implemented, irradiation of samples for radiobiological studies exploits scattering of the proton beam through a 210 μm Lead foil followed by free expansion in air to obtain a gaussian transverse profile in both x and y. The target position is typically 1.5 - 2 m downstream the exit window. No collimators are used in this configuration. Figure 12 and Figure 13 show an example of such a configuration.

Dosimetry techniques developed for in-vitro radiobiological experiments (de Angelis et al., 2019) were applied for the beam characterization at the target position for RHA activities. In this paragraph we will give an overview of the method and leave detailed examples of irradiation set-up characterizations to the next chapters.

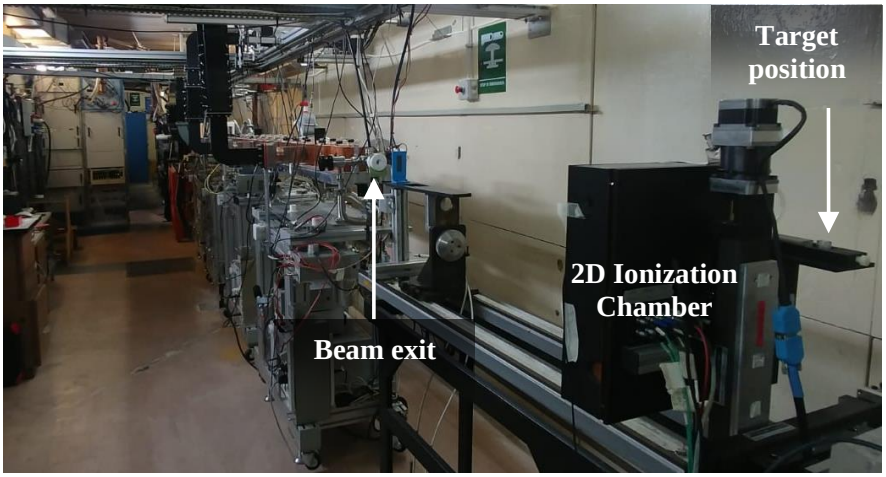

Figure 12 Beam monitors and dosimetric equipment from the beam exit to the target position 155 mm after the 2D Ionization chamber

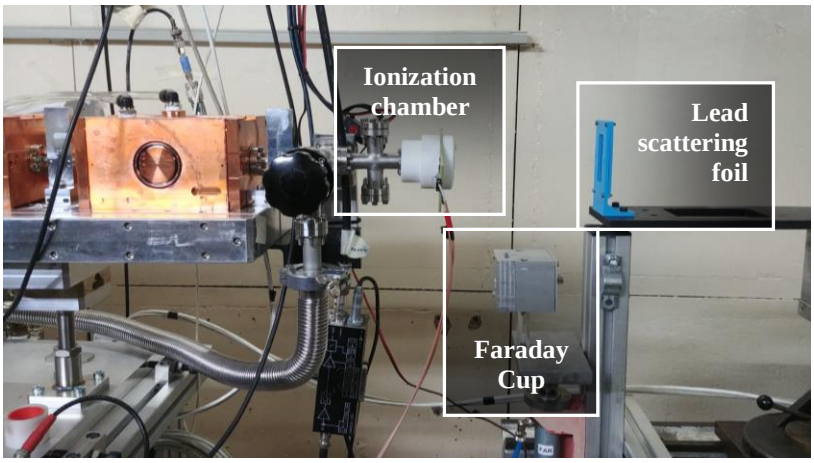

Figure 13 Beam monitors and dosimetric equipment; detail at the exit window of SCDTL4: integral ionization chamber, Faraday Cup and lead scattering foil

The beam parameters relevant for both in-vitro radiobiology and radiation hardness assurance are the following:

- The homogeneity of the beam intensity at the target position
- The energy of the particles impinging on the target
- The flux, that is the number of protons hitting the target per unit area per second
- And the fluence, that is the integrated flux over the irradiation time.

The desired accuracy to comply with ESCC standard guidelines is plus or minus 10% on all parameters, whereas typical Irradiation of radiobiological samples requires spatial beam homogeneity better than 5% in a spot of 40 mm diameter.

Numerical computation is a powerful tool to define an irradiation set-up. The beam properties at the target position can be calculated combining the parameterization of the beam extracted from the accelerator given by the code LINAC (Crandall & Weiss, 1994)and the beam transport through matter with the code SRIM (Ziegler et al., 2010). Computed and measured parameters typically agree within 5 and 10 percent for energy and homogeneity and within 10 and 15 per cent for the flux and fluence. The reason for this larger discrepancy on the flux and fluence is that these parameters are strongly dependent on the actual pulse by pulse proton charge delivered to the target.

2.4.1 TRANSVERSE SIZE AND HOMOGENEITY

The beam size, position and homogeneity at the target position are described in terms of the μ and σ parameters of a 2D Gaussian transverse intensity distribution. Due to the beam gaussian profile, the useful irradiation spot radius r depends on the desired homogeneity h and the sigma:

$$h = 1 - e^{-\frac{r^2}{2\sigma^2}}$$

Beam-target transverse alignment is preliminary verified (without the scattering foil) with the 2D segmented ionization chamber: a beam barycentre μx; μy < 1 mm is considered adequate for the typical spot size and homogeneity. Figure 14 portrays an example of such an acquisition with 55.5 MeV proton beam. The 2D ionization chamber also measures the beam σ, both as RMS of the distribution and form fit of the profiles, but due to its limited size (40 x 40 mm2) it cannot assess the broad beam sigma with the required precision.

Profile of the diffused beam at the target position is calculated with SRIM and compared against EBT3 Gafchromic films acquisitions (Ashland ISP Advanced Materials, NJ, USA) as described in (de Angelis et al., 2019). Millimetric precision on the beam sigma is obtained with this technique.

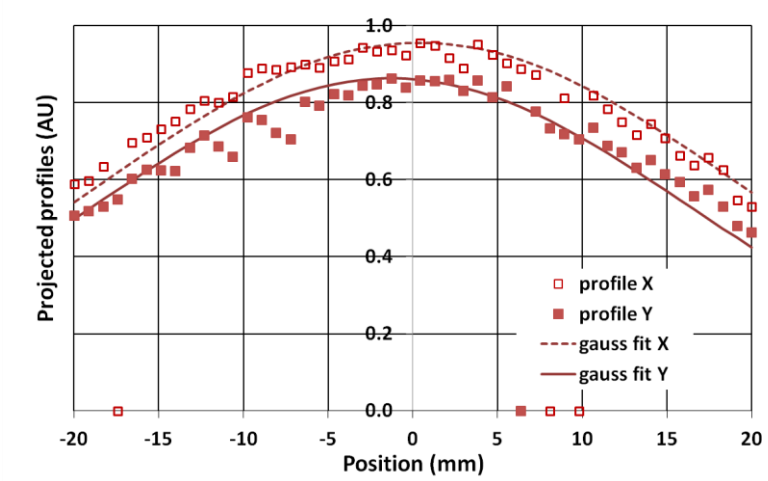

Figure 14 Horizontal and vertical beam profiles acquired with the 2D Ionization Chamber for beam-target alignment (55.5 MeV proton beam)

2.4.2 ENERGY AND ENERGY SPREAD

Beam energy and spectrum is measured by experimental Bragg Peak imaging of visible photoluminescence centres in LiF crystals with the same technique described in 2.3.4.

2.4.3 FLUX, FLUENCE AND DOSE MONITORING

An estimation of the flux at the target position can be obtained once the transverse geometry and homogeneity have been assessed at least with SRIM calculation: assuming an ideally constant beam extraction current, flux can be evaluated with an uncertainty around 10 – 15 %. To achieve higher accuracy, flux and fluence are monitored online and machine parameters are tuned to obtain the desired values.

The integral ionization chambers are presently the main online beam delivery monitor. The proton flux at the target position can be changed varying either the charge per pulse or the repetition frequency (typical repetition frequency is 25 Hz). In principle, this allows a variation of flux values of over two orders of magnitude. Irradiation of samples is charge driven: the proton beam is switched off once the desired total charge, recorded by the integral ionization chamber, is delivered. The ionization chamber readings are periodically compared against measured dose (i.e. Total Ionizing Dose) in water at the target position using a calibrated

μDiamond dosimeter 600019 (PTWFreiburg, Germany) (Mandapaka et al., 2013) as described in (de Angelis et al., 2019). Dose delivery to target has been characterized at different dose rates in the typical range of the radiobiological studies (few Gy/min), showing a reproducibility of ≈ 2% and an accuracy better than 4% within the same irradiation session of up to few tens of minutes.

The 2D Ionization Chamber, positioned a few centimetres before the target, acts as an independent supervisory monitor recording the beam total charge and charge per pulse during the irradiation session. Comparison of the 2D Ionization Chamber readings with the μDiamond dosimeter are in very good agreement, at least within a single dosimetric characterization session: response of the ionization chamber is proportional to the total dose assessed by the μDiamond and deviation from linearity is less than 1%. Figure 15 shows an example of a characterization curve obtained with 55.5 MeV proton beam.

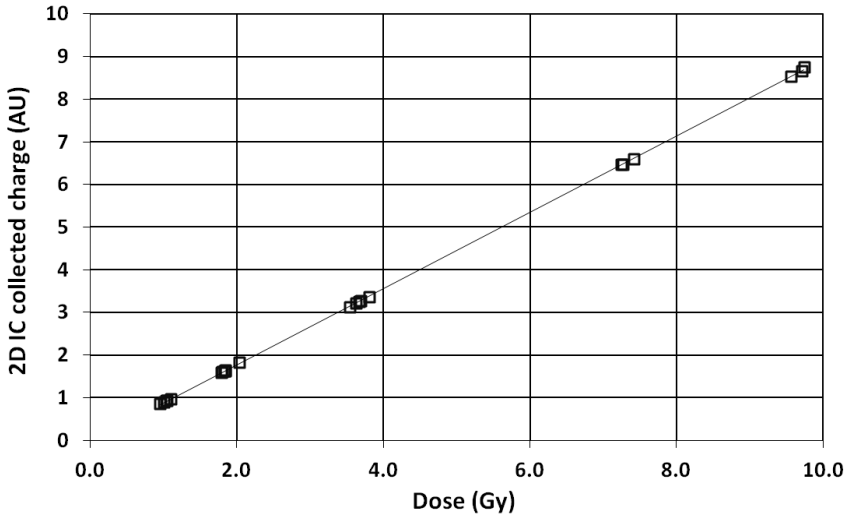

Figure 15 Comparison of 2D Ionization Chamber readings and μDiamond dose measurements within a beam qualification session.

Dose and dose rate measurements are converted, for the purposes of radiation tolerance tests, to fluence and flux thanks to the relation:

$$\Phi = \frac{1}{K} \cdot \frac{D}{\left(\frac{S_{coll}}{\rho}\right)} \quad [p\ cm^{-2}]$$

where Φ is the particle fluence expressed in protons cm−2, K = 1.602 × 10−10 is a scale factor, and the mass-collision stopping power S_{coll}/ρ, which has units of MeV·cm2/g, is computed from PSTAR ((Berger et al., 2005)) assuming a monochromatic beam energy incident on the *μDiamond* and taking into account the energy degradation induced by the 1mm–water equivalent material in front of the dosimeter sensitive area. When calculating the fluency with this method we must combine the uncertainty on the dose and the uncertainty on the energy and Linear Energy Transfer, which is typically around 2-3 %. To fulfil a requirement of ± 10% accuracy on fluence determination, the monitoring system should therefore guarantee a better dose accuracy. In the clinical practice, the required dose accuracy is typically 3-4 %.

Chapter 3

A P-I-N DIODE ONLINE DOSIMETRY SYSTEM FOR DISPLACEMENT DAMAGE MEASUREMENT

As discussed in the introduction, dosimetry for Total Ionizing Dose, Displacement Damage and Single Event Effects relies on measurement of fundamental beam properties such as energy and fluence. It was demonstrated in Chapter 1 that a monitoring system developed for proton therapy, that is to monitor TID in water, is sufficient to characterize the beam delivery also for RHA activities. Nevertheless, specifically for the purposes of electronic components testing, we implemented an additional online dosimetry system for Displacement Damage measurement. It is based on a cheap, COTS component whose applications have been investigated at CERN since the early nineties and is now routinely used also in other laboratories. Its simple procurement and use, together with the availability of literature data on its behaviour, make it a good candidate for a first "case study" to test our beam qualification system.

3.1 DISPLACEMENT DAMAGE DOSE MONITORING WITH BPW34F P-I-N DIODES

The investigated device is the commercial BPW34 silicon p-i-n diode, which is commercially produced by several companies such as OSRAM, VISHAY, SIEMENS. Its availability and low cost, together with a high spatial resolution are its main advantages that often overcome the limited accuracy and batch by batch reproducibility which are typical of COTS products.

In the field of radiation oncology, and particle therapy in particular, this device has been employed as an ionization monitor (that is, in RHA terminology, a TID monitor) at the Canadian proton therapy facility TRIUMF (Oelfke et al., 1995) and at the German hadrontherapy centre HIT (Kaiser et al., 2010) for dose depth dose distributions characterization in water with protons and carbon ions beam. In these applications, the p-i-n diode is either biased or unbiased and acquired with an electrometer, such as those used for standard Quality Assurance protocols, thus operating as a "solid state ionization chamber".

The possibility to employ this type of diode as large range, low sensitivity dosimeter for Displacement Damage Dose (DDD) was investigated at CERN since the early nineties (Malfante, 1992); after systematic research by Ravotti (Ravotti, 2006) (Ravotti et al., 2008) and Mekki (Mekki, 2009) on the definition of a readout protocol this device is included in the catalogue of radiation monitoring sensors for the LHC experiments (Ravotti, Glaser and Moll, 2005). The methodology developed at CERN is applied in other laboratories: at LANSCE, the Los Alamos 800 MeV proton LINAC source, real time measurement of the beam profile and fluence is performed through employment of a 7 x 7 array of BPW34F diodes (Palni et al., 2013); at the ISIS Proton Synchrotron of the Rutherford Appleton Laboratory the BPW34F was included in a prototype of online radiation damage monitor for components and systems of the accelerator (Harryman & Pertica, 2016).

In the readout procedure developed at CERN BPW34F p-i-n diodes are used in forward bias mode by applying a constant readout current of short duration pulse to avoid self-heating effects. Using this method, sensitivity to fast hadrons has been observed with linearity of response for $\Phi_{eq} > 2\ 10^{12}$ cm^{-2} and up to high fluences ($\Phi_{eq} \approx 4\ 10^{14}$ cm^{-2}) by measuring the variation of the forward voltage versus equivalent fluencies Φ_{eq} in units of 1-MeV neutron equivalent fluence with typical data to model reproducibility of ± 20% (Ravotti et al., 2008). In the characterization procedure, different batches of BPW34F diodes had been irradiated with very high energy protons (23 GeV) of CERN IRRAD1 facility and neutrons provided by the IRRAD2 facility (Gkotse et al., 2015) to verify that the sensor response is consistent with the NIEL scaling and insensitive to rate effects, and with Co^{60} γ-rays to verify that the device is insensitive to TID contribution when operated with the developed procedure. Figure 16 reproduce Figure 8 from (Ravotti et al., 2008) summarizing the existing data of radiation response of the BPW34F diode.

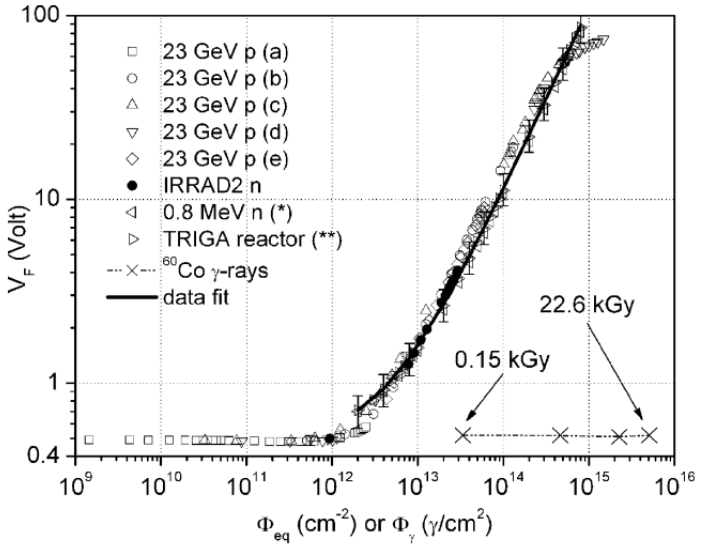

Fig. 8. Radiation response of BPW34F diodes at room temperature. The diode's forward voltage at 1 mA is plotted versus the Φ_{eq}. The width of the readout current pulse was of 700 ms. The experimental data taken in IRRAD1 at CERN has been recorded at different proton rates: (a) 2.4×10^{11} cm$^{-2} \cdot$h^{-1}, (b) 3.7×10^{12} cm$^{-2} \cdot$h^{-1}, (c) 8.1×10^{12} cm$^{-2} \cdot$h^{-1}, (d) 2.0×10^{13} cm$^{-2} \cdot$h^{-1}, (e) 2.5×10^{13} cm$^{-2} \cdot$h^{-1}. In the same pictures data from [21](*), [22] (**) and following exposure to γ-rays have been also reported. For the photon data, the x-axis corresponds to the number of photons per square centimetres. Error bars of $\pm 20\%$ have been reported to show the accuracy of the data best-fit.

Figure 16 Summary of BPW34F diode response as reported in (Ravotti et al., 2008)

While more sensitive devices exist to measure Φ_{eq} in our typical range of use, thanks to the peculiar application for both particle therapy TID dosimetry and RHA Displacement Damage dosimetry, together with its cost and availability, the BPW34F diode was selected as a case study for this research thesis. The device accuracy, as demonstrated at CERN, is at the limit of the prescription of RHA standard irradiation monitoring and its appropriateness as candidate for an independent irradiation supervisory system is to be evaluated. Nevertheless, thanks to its small size, it could be routinely employed in RHA test as the equivalent of an "in vivo" dosimeter in radiation therapy: installed on the irradiation board next to the Device Under Test it would guarantee an independent measurement of dose and provide redundancy. To this end was to implement a remote acquisition system compliant with the DD dosimetry procedure developed at CERN and compared our result, obtained after irradiation with low energy protons, with literature results which are obtained from neutrons and very high energy protons. In this chapter we report:

- a summary of the readout protocol developed at CERN,
- the implementation of a remote acquisition system for the TOP-IMPLART accelerator,
- the qualification of a batch of BFW34F diodes, and the pre-irradiation procedure of one diode by passive accumulation during radiobiology activities,
- discussion of the results and comparison with the expected behavior based on the existing literature

3.2 READOUT PROCEDURE FOR BPW34F AS A DISPLACEMENT DAMAGE DOSIMETER

The readout procedure defined in the sensor catalogue at CERN (Ravotti et al., 2005) is defined for pre-irradiated BPW34F p-i-n diodes. Pre-irradiation consists in the accumulation of an equivalent fluence of $\Phi_{eq\ min} \approx 2\ 10^{12}$ cm^{-2} 1 MeV neutrons. After this threshold, the forward voltage of device increases, with respect of the forward voltage of the unirradiated diode, grows linearly with the equivalent fluence, as seen in Figure 16, according to the relation (Ravotti et al., 2008):

$$\Delta V_F = c \cdot k \cdot \Phi = c \cdot \Phi_{eq} \qquad 6$$

where $1 / c = 9.1 \times 10^9$ cm^{-2}/mV is the device sensitivity and k is the hardness factor.

The reported device sensitivity, which is the minimum equivalent fluence to cause an increase of 1 mV in the forward voltage, is obtained when the diode is excited with a test current of 1 mA with a pulse length of less than 1 s (typically 100 ms). The test current value was selected to maximize the useful operating range of the device ($\Phi_{eq\ max} = 4\ 10^{14}$ cm^{-2} 1 MeV neutron equivalent): use of higher current values reduces the maximum useful range and increases the sensitivity factor, i.e. increases the minimum equivalent fluence to produce an increase of 1 mV in forward voltage. While all investigated useful operating range are more than adequate for TOP-IMPLART application, where expected fluxes are much lower than those of the LHC tunnel environment, it is advantageous to select the readout procedure that minimize the sensitivity factor. For this reason, we adopted the "standard" test current value of 1 mA, applied not only at CERN but also at LANSCE and RAL, in the applications previously mentioned.

The optimal pulse length was also investigated. Self-heating effects, resulting in V_F reduction up to 10%, were observed for pulse length of the order of 1 s in diodes with accumulated $\Phi_{eq} \approx 10^{13}$ cm^{-2} 1 MeV neutron equivalent. The pulse length should thus be the minimum compatible with a stable V_F reading and is typically of the order of 100 ms.

Characterization of the BPW34F was carried out at CERN with a Keithley 2400 Source Measurement Unit (SMU), a precision instrument to supply a wide range of current pulses and measure voltage up to 200 V.

To perform a correct readout, the BPW34F diode shall be shielded from the light and shorted during the irradiation exposure. A remote relay system is therefore needed to switch the diode from exposure mode to measurement mode.

3.3 IMPLEMENTATION OF A REMOTE ACQUISITION SYSTEM FOR BPW34F DIODES AT THE TOP-IMPLART ACCELERATOR

Should the device respond according to the NIEL hypothesis also at proton energies of the order of tens of MeV, such is the case for TOP-IMPAT beam, the expected corresponding proton fluence sensitivity shall depend on the hardness factor for silicon (the material that constitute the sensitive part of the p-i-n diode). The hardness factor is reported in literature by different authors on different materials relevant for electronic components (namely Si, SiO_2, GaAs) and with different radiations (p, n, π ...) and energies. For protons in the MeV range the main sources are the works of G.P. Summers (Summers et al., 1993) and other authors, often as private communications. A comprehensive summary of such data is available online (Vasilescu and Lindstroem, https://rd50.web.cern.ch/NIEL/default.html). Table 3 lists data for the hardness factor of proton on Silicon for energies relevant for the current configuration of the TOP-IMPLART accelerator. In Figure 17, data are represented and interpolated with the best-fit curve:

$$k_{protons}(E_{kin}\,[MeV]) = 11.542 * E[MeV]^{-0.472} \qquad 7$$

which reproduces the experimental data within a 6% tolerance.

In the energy range of our interests the hardness factor k is always greater than 1, meaning that protons of tens of MeV are more effective than 1 MeV neutrons in creating displacement damage defects.

Table 3 NIEL hardness factor for protons on Si from Summers and Huhntinen (Vasilescu and Lindstroem)

Ekin [MeV]	D/(95MeVmb)	Source
15.00	3.38	Huhntinen
25.00	2.56	
35.00	2.13	
45.00	1.88	
55.00	1.71	
10.00	3.87	Summers
20.00	2.63	
30.00	2.35	
50.00	1.91	
70.00	1.55	

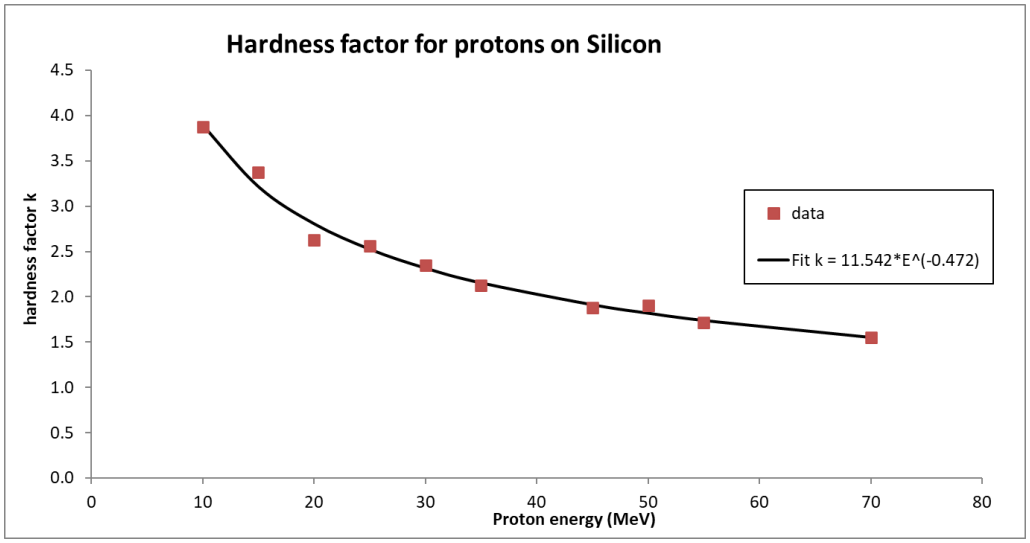

Figure 17 NIEL hardness factor for proton on Si from Summers and Huhntinen (Vasilescu and Lindstroem)

A standard SMU was not available in the TOP-IMPLART laboratory when this research activity was initially proposed. Based on indications found in (Harryman & Pertica, 2016) we developed a remote acquisition system based on a National

Instrument single board RIO sbRIO 9636 and an in-house voltage controlled current source which is described in Appendix A.

The prototype acquisition system was developed to acquire signal from two diodes. It should provide a switch system for the diodes between a shortened mode, for irradiation, and a measurement mode. A calibration mode is also requested to periodically check the scaling factor between the supplied voltage and generated current.

3.4 EXPERIMENTAL ACTIVITY ON DIODES PRE-IRRADIATION

3.4.1 DIODES SELECTION

We procured 10 diodes BPW34F manufactured by OSRAM. As a prerequisite for the experimental activity, we verified the homogeneity of our samples of non-irradiated diodes in terms of forward voltage drop after application of the test current of 1 mA. The starting value $V_{F,0}$ homogeneity is expected to be of the order of ≈ ± 11% based on data (on much larger samples) reported in (Ravotti, 2006).

As our current generator lacks the accuracy of a SMU, and has limited reproducibility, to obtain a consistent set of data we consider for each diode the following quantity:

$$V_{F,0} = V_F / i_{test}$$

Where V_F is the voltage drop measured at an i_{test} close, but not equal to, 1 mA. V_F and i_{test} are obtained from the V_{drop} and i_{pulse} traces as the average value of 800 samples from the flat-top. Table 4 summarizes the collected data.

The average value on our sample is therefore:

$$V_{F,0} = 0.529 \pm 0.022 \text{ V}$$

and the uncertainty of ± 0.022 V is a total uncertainty (computed as max- min value). It corresponds to a homogeneity better that 5%. All procured diodes are therefore accepted.

Table 4 Summary of pre-irradiation characterization of the BPW34F diodes sample

	V drop		i pulse		
Diode nr	**aver**	**rms**	**aver**	**rms**	**$V_{F,0}$ @ 1 mA**
1	0.5275	0.0005	1.0023	0.0017	0.5262
2	0.5282	0.0004	1.0036	0.0013	0.5263
3	0.5316	0.0005	1.0043	0.0015	0.5293
4	0.5324	0.0005	1.0041	0.0014	0.5302
5	0.5381	0.0003	1.0049	0.0011	0.5355
6	0.5304	0.0005	1.0051	0.0010	0.5277
7	0.5180	0.0002	1.0036	0.0011	0.5161
8	0.5402	0.0004	1.0046	0.0010	0.5377
9	0.5310	0.0003	1.0038	0.0013	0.5290
10	0.5340	0.0002	1.0039	0.0011	0.5319

3.4.2 CHARACTERIZATION OF THE EXPERIMENTAL SET-UP FOR DIODE PRE-IRRADIATION

In March 2019 diode nr 5 was positioned in the bunker. No dedicated beam time was allotted for its pre irradiation, but passive dose accumulation was still possible during ordinary dosimetry and radiobiology sessions. For this reason, the diode was placed on a PFB "finger" that allowed a reproducible positioning out both on beamline axis and out of the direct beamline, not to interfere with the other activities, intercepting only the beam tails.

Here we describe the irradiation geometry and the procedure employed for fluence estimation at the diode position: it is a detailed example of the procedure outlined in 2.4 and later applied for all irradiation reported in this thesis.

3.4.2.1 IRRADIATION GEOMETRY

The p-i-n diode was housed on the mechanical structure of the 2D ionization chamber as shown in Figure 18. It is aligned vertical with the chamber (and the beam), but horizontally displaced by 40 mm from the beam line.

The beam line geometry and budget of materials encountered by the beam was as described by the following Figure 19 and Table 5.

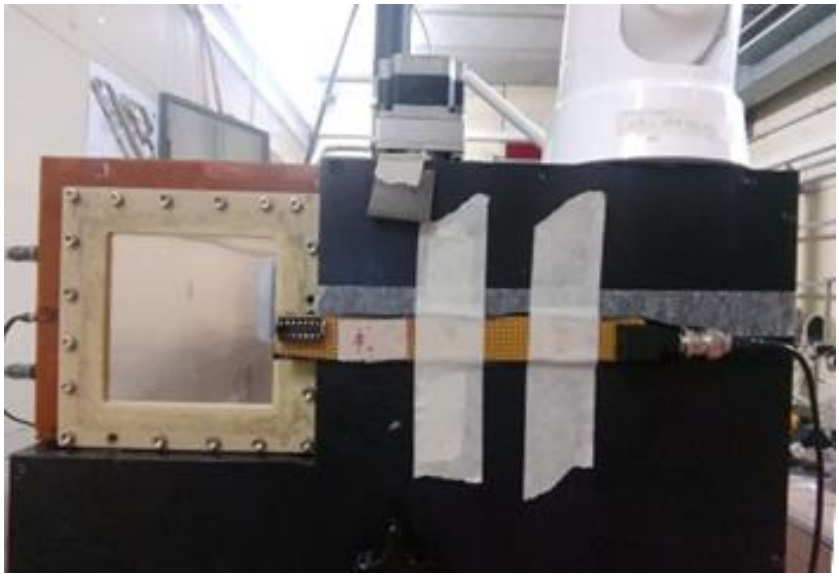

Figure 18 Diode nr 5 positioned off-axis on the 2D ionization chamber in the march 2019 irradiation campaign

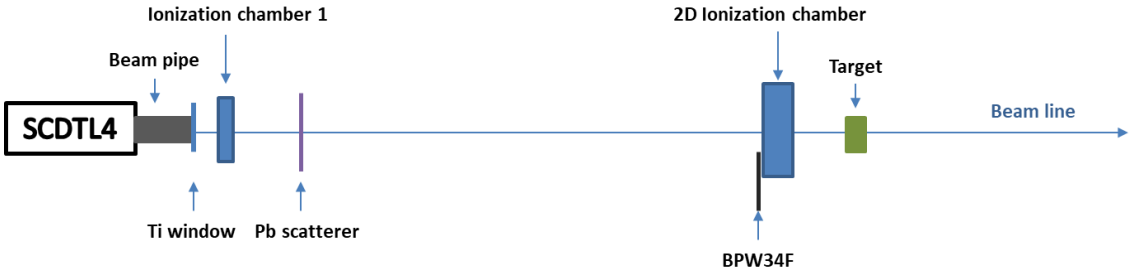

Figure 19 Schematic layout of the irradiation setup for March 2019

Table 5 List of materials encountered by the proton beam

	Distance from SCDTL4 (mm)	Thickness (mm)	Material
Beam pipe	181	181	vacuum
Titanium window	181.05	0.050	Titanium
Lead scatterer	300	0.210	Lead
BPW34F	1570	----	----
2D Ionization chamber	1595	0.170	Water equiv.
Target / µDiamond	1750	-----	-----

3.4.2.2 BEAM PROPERTIES SIMULATION WITH SRIM AND LINAC CODES

Beam parameters at the target position are calculated with SRIM (Ziegler et al., 2010) .

The energy and kinematic information of the beam are included in a TRIM file generated at the SCDTL4 exit (i.e., before the Titanium window) with the LINAC code (Crandall & Weiss, 1994) (Figure 20).

The transverse distribution obtained with SRIM at the BPW34F position is shown in Figure 21: the FWHMs for both x and y profiles are 99 mm, corresponding to a standard deviation $\sigma \approx 42$ mm. At the diamond dosimeter position the calculated standard deviation is 46 mm.

The expected mean energy value at the diode position is 30.3 MeV; at the diamond position is 29.6 MeV and at the target position, after 3 mm of PMMA, is 23.8 MeV.

Please note that at the diamond position the computed energy of 29.6 MeV is the energy of the protons impinging on the dosimeter encapsulation. The actual sensor is placed at 1 mm tissue equivalent depth. Therefore, the proton energy seen by the μDiamond dosimeter is 27.6 MeV

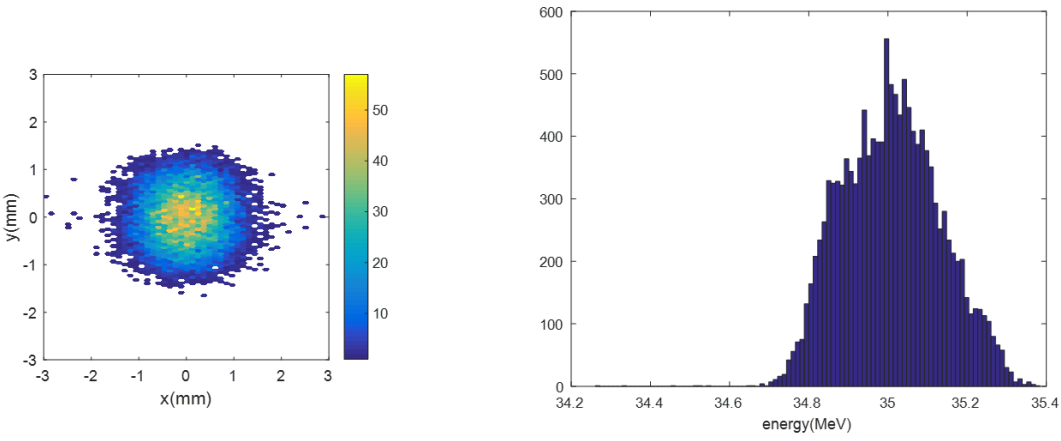

Figure 20 Beam parameters at the SCDTL4 exit computed with LINAC: transverse position distribution (left) and energy distribution (right)

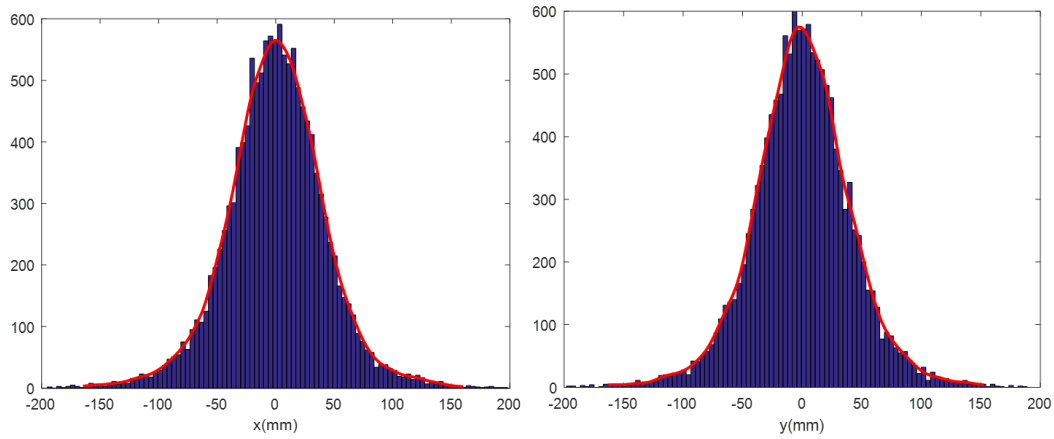

Figure 21 Transverse distribution at the BPW34F / 2D ionization chamber position calculated with SRIM/TRIM

3.4.2.3 BEAM SIZE AND HOMOGENEITY AT THE BPW34F / 2D CHAMBER POSITION

The beam transverse homogeneity mapping at the 2D chamber position was measured with an EBT3 radiochromic film placed in front of the 2D ionization chamber with the diode support removed.

The digitized image was analysed to compare the uniformity on a small (≈ 0.5 cm^2) Region Of Interest (ROI) at the beamline centre and at off- centre diode position:

- dose uniformity at the centre: ± 4 % (3 σ)
- dose uniformity off centre: ± 6 % (3 σ)

The dose uniformity on the relevant area is therefore adequate and there is no significant difference in the two irradiation positions in terms of homogeneity.

Conversion to dose with Co^{60} calibration data (Vadrucci et al., 2015) to evaluate the beam transverse intensity distribution on the horizontal and vertical axis is shown in Figure 22. Profiles are fitted with a gaussian distribution resulting in a standard deviation of $\sigma_X \approx \sigma_Y = 40$ mm. As the gafchormic acquisition only captures a portion of the gaussian profile, we consider acceptable the 5% agreement between experimental and calculated values. Comparison of simulated (SRIM) and experimental (EBT3 gafchromic) profiles is shown in Figure 23.

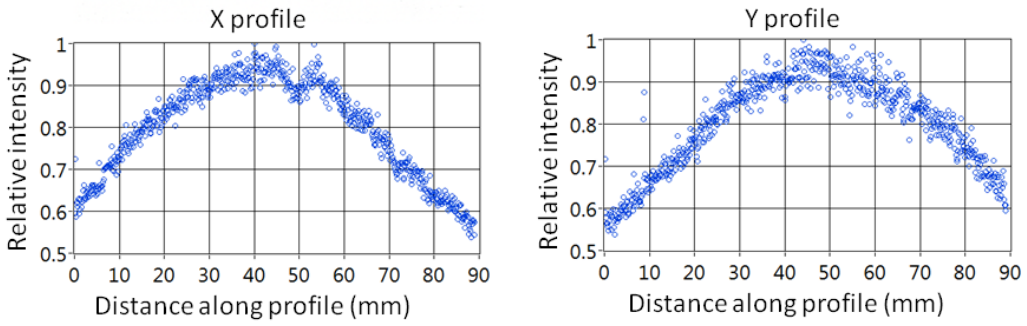

Figure 22 EBT3 gafchromic film acquisition with a Region Of Interest of 44.45 mm radius: elaborated beam x and y profiles

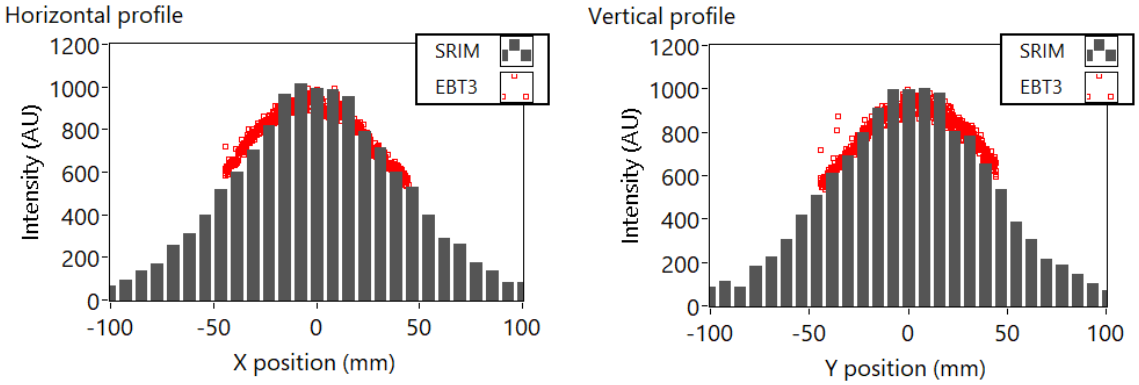

Figure 23 Comparison of calculated (SRIM) and experimental (EBT3) transverse beam profiles at the BPW34F position

3.4.2.4 ENERGY MEASUREMENT WITH LIF CRYSTALS

Beam energy was measured by experimental Bragg Peak imaging of visible photoluminescence centres in LiF crystals. The energy measurement was performed at the target position, after 3 mm of PMMA. Figure 24 shows the acquired dose depth profile in a 10 mm long LiF crystal and the corresponding spectral content obtained from the analytical model and best fit of data. Mismatch in measured/fitted curves are due to artefact in the air/crystal interface (at depth 0 mm) and pedestal due to residual light contribution from the blue lamp used to excite the luminescence.

Measured peak energy is 24.07 ± 0.15 MeV, that is within 1% agreement with the computed values. We therefore consider acceptable the computed values along the irradiation line.

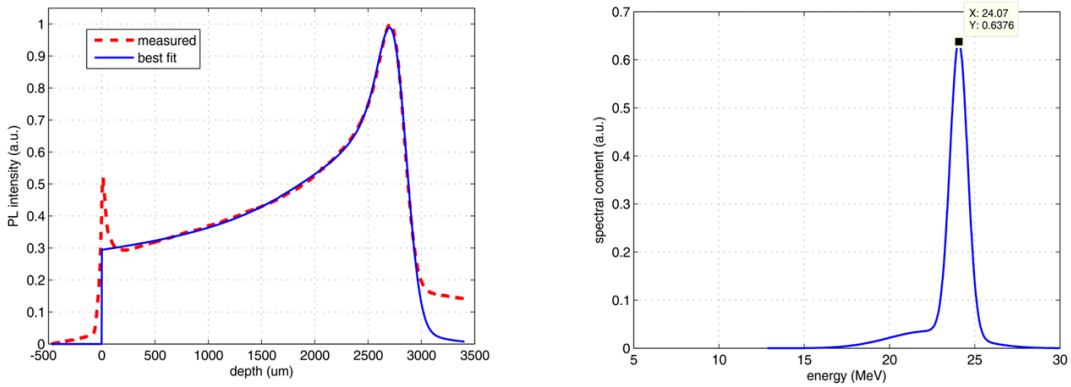

Figure 24 LiF crystal energy measurement: acquired Bragg Peak profile in LiF crystal (left); proton beam spectral content from analytical model and best fit of data (right)

3.4.3 FLUENCE EVALUATION AND BPW4F DIODE RESPONSE

3.4.3.1 FLUENCE EVALUATION AT THE μDIAMOND AND DIODE POSITIONS

The beam characteristics at the diode position are summarized in Table 6.

For a proton energy of 30.3 MeV we obtain with equation 7 the hardness factor:

$$k_{protons}\ (30.3\ MeV) = 2.31$$

that is, protons of this energy are 2.31 times more effective in inducing Displacement Damage with respect to 1 MeV neutrons.

Table 6 Beam characteristics at the diode position

Parameter	Value	Unit
Energy	30.3	MeV
Beam transverse size (gaussian) – 1 σ	42	mm
X position – "on axis"	7	mm
X position – "off axis"	47	mm
Relative intensity – "on axis"	98.6	%
Relative intensity – "off axis"	53.3	%

Applying 6 we thus expect to measure an increase of Forward voltage of 1 mV after irradiation with a 30.3 MeV proton fluence of:

$\Phi_{p\ 30.3\ MeV} = \Delta V_F / c \cdot 2.31$

$\approx 3.9 \times 10^9\ cm^{-2}$

for $\Delta V_F = 1$ mV ; $1 / c = 9.1 \times 10^9\ cm^{-2}/mV$

The minimum equivalent fluence to be accumulated (pre-irradiation) before the device responds linearly with displacement damage dose is:

$\Phi_{eq\ min} \approx 2\ 10^{12}\ cm^{-2}$ [1 MeV neutrons] $\approx 8.7\ 10^{11}\ cm^{-2}$ [30.3 MeV protons]

The beam characteristics at the μDiamond dosimeter sensitive area position are summarized in Table 7

Table 7 Beam characteristics at the μDiamond position (at the sensitive area)

Parameter	Value	Unit
Energy	27.6	MeV
LET (in water)	20.16	MeV $cm^2\ g^{-1}$
Beam transverse size (gaussian) – 1 σ	46	mm
X position – "on axis"	0	mm

Evaluation of the cumulated fluence at the diode position relies on the measurement of dose in water at the μDiamond position by means of the usual relation

$$D[Gy] = 1.602\ 10^{-10} \cdot\ \Phi\ [cm^{-2}] \cdot \frac{S}{\rho}[MeV\ cm^2 g^{-1}]$$

Additionally, a scaling factor should be applied to compensate for the beam divergence and the relative intensity.

$$\Phi_{diode} = \Phi_{diamond} \cdot \left(\frac{\sigma^2_{diamond}}{\sigma^2_{diode}}\right) \cdot (relative\ intensity)$$

3.4.3.2 BPW34F DIODE RADIATION RESPONSE

Data collected in March – April 2019 for the BPW34F diode nr 5 are shown in Figure 25. The diode forward voltage variation (with respect to the original, unirradiated value) is plotted against the cumulated equivalent fluence calculated as described in the previous paragraph. The observed behaviour is qualitatively consistent with what expected from literature: the initial response is a decrease in Forward Voltage followed by an inversion of the response, which becomes linear for fluences above 2 10^{12} cm^{-2} 1 MeV neutron equivalent.

When we consider data point for fluences above 2 10^{12} cm^{-2} 1 MeV neutron equivalent a linear fit results in an experimental sensitivity factor of:

$$1 / c_{exp>2e12} = 1 / (9.3\ 10^{-11}\ mV/cm^{-2}) = 10.8 \times 10^{9}\ cm^{-2}/mV$$

When only data above 2.5 10^{12} cm^{-2} 1 MeV neutron equivalent are considered

$$1 / c_{exp>2.5e12} = 1 / (1.1\ 10^{-10}\ mV/cm^{-2}) = 9.1 \times 10^{9}\ cm^{-2}/mV$$

which is the sensitivity value reported in literature.

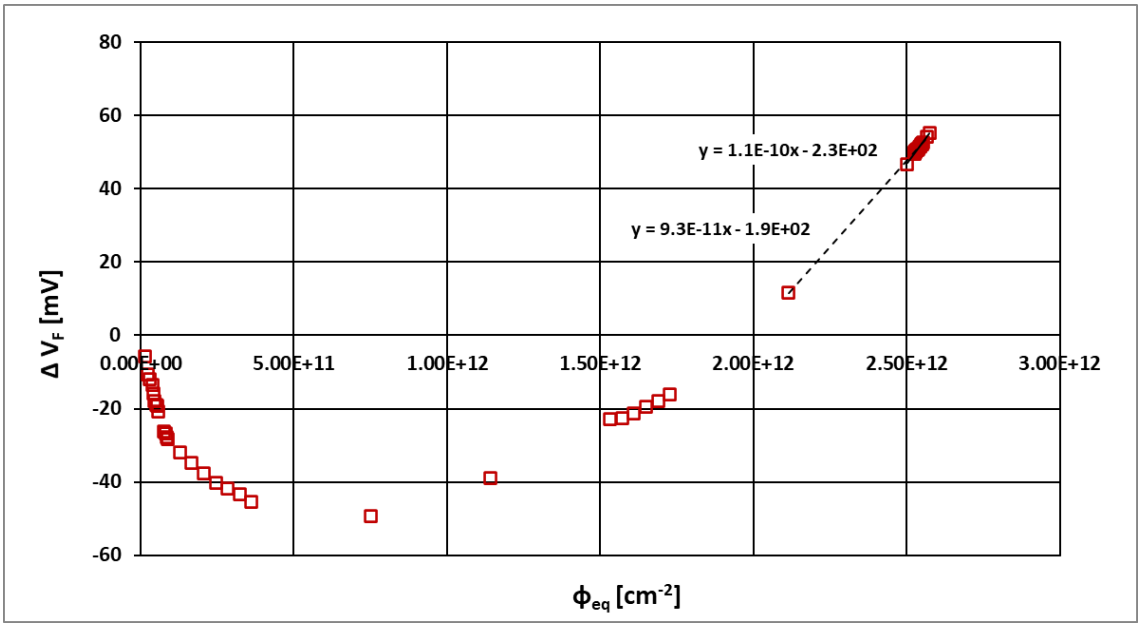

Figure 25 Radiation response of BPW34F p-i-n diode nr 5 as a function of the accumulated equivalent fluence

3.5 DISCUSSION

Despite many limitations both in procedure and accuracy, we consider this preliminary result satisfactory. The latest acquired set of data, though small, is consistent with the sensitivity value reported in literature of 9.1 10^9 cm^{-2}/mV; therefore we can consider the diode to be properly pre-irradiated and apt for dosimetry purposes.

Procedural issues emerged that were addressed in later iteration of the system:

- **Test current repeatability**

The diode response is strongly dependent on the test current value. Readings were consistent if the test current value was 1 mA ± 3uA and a compensated $V_{F,0} = V_F / i_{test}$ was considered, as already described in 3.4.1. Due to the limitations of our current source, ensuring test current repeatability and stability requires frequent calibration and repeated measurements on the diode. The latter should be avoided not to induce annealing.

As a single, accurate measurement is not achievable with the present acquisition system, we decided to implement a measurement scheme based on an I-V scan of 5 acquisitions around the 1 mA value. The diode expected behaviour is exponential: the $V_{Forward}$ value at 1 mA is calculated from the fitted curve. This scheme is a compromise between the need to perform multiple measurement and the repeatability.

- **Long term annealing**

The BW34F diode is known to suffer long term annealing, with typical decrease in $V_{Forward}$ value of the order of ≈ 25% per week. While this behaviour is of concern when one wishes to monitor ambient dose (such as in the LHC tunnel) on a months or years' time span, for our intended application, that is to cross-check the delivered fluence to a device, it is not as critical. In fact, we measure the forward voltage variation before and immediately after the irradiation. On the other hand, as our system may not be exposed to radiation for lengthy periods, we shall verify that diode behaviour is still linear with the accumulated displacement damage dose, and it did not revert to a pre-irradiated stage.

Chapter 4
RADIATION TESTING OF A 6-AXIS MEMS INERTIAL NAVIGATION UNIT WITH PROTONS AND X-RAYS

This chapter reports irradiation activities on a commercial Inertial Navigation Unit which includes a 3-axis accelerometer, a 3-axis gyroscope, and an ASIC for digital communication with the device manufactured with MEMS/CMOS technology by ST Microelectronics. Tests were conducted with protons in summer 2019 and with X-rays in summer 2020. Both irradiation campaign results were presented at the International Astronautical Conference of the same year and are published in the conference proceedings (Bazzano et al., 2019) (Bazzano et al., 2020); additionally, the proton irradiation campaign was published in a peer review journal (Bazzano et al., 2021). This chapter is mainly based on those already published contributions.

4.1 INTRODUCTION

Small satellite space missions are an important asset, and their relevance is increasing in recent years, not only for educational purposes, but also as technological demonstrators, and for realizing constellations of a huge number of nanosatellites for communication and internet providers (Lal et al., 2017) (Pang et al., 2016) (Williams et al., 2018). This kind of missions would greatly benefit from the use of commercial components. MEMS technology has made a wide variety of

cheap, lightweight sensors for attitude determination and control available on the market, often combining multiple axes and multiple sensors on a single chip and providing digital IO interface through the embedded Application Specific Integrated Circuit (ASIC). These devices have been successfully used as sensors for attitude determination in University CubeSat missions. As an example, the Radio Aurora Explorer (RAX) is a CubeSat mission developed to study space weather in Earth's ionosphere (Klesh et al., 2009), (Springmann et al., 2011) which employed a COTS MEMS Inertial Measurement Unit (IMU) by Analog Devices. While COTS parts are an attractive alternative to RadHard space qualified components, due to their lower cost and shorter procurement time, their proper qualification following standard RHA protocols would be so expensive and time consuming as to eventually overcome the benefits. As highlighted in (*RADIATION REQUIREMENTS GUIDELINES FOR MEMS DEVICES*, 2009), radiation resistance characterization of MEMS devices poses the additional challenge of probing both electrical and mechanical domain, further increasing the complexity of the procedure. As indicated in previous studies (Knudson et al., 1996), the specific architecture of the mechanical part of the sensor can lead to very different outcome in radiation resistance. The burden of RHA on COTS components cannot be sustained in particular on the typical limited resources of Universities' SmallSats projects, which is the framework of our research. Many authors in recent years have proposed novel RHA strategies, especially tailored for COTS parts and Low Earth Orbit (LEO), thin-shielded missions ((Alia et al., 2017);(Rousselet et al., 2017); (Sinclair & Dyer, 2013)). These novel, simplified testing strategies also consider the growing complexity of components (di Mascio et al., 2018), which hinders the applications of standard testing guidelines, especially, as is often the case, when details of the device architecture are not made available by commercial components manufacturer. Proton, which allow probing simultaneously cumulative (TID and NIEL) and stochastic (SEE) effects, could provide a trade-off between rigorous, but expensive, standard qualification process and usage of untested parts with unpredictable fault modes. Additionally, protons as a radiation source are representative of the trapped particles environment that the device could actually be subjected to in LEO orbits, the most common for this kind of satellites.(Pitt et al., 2017) investigated the radiation response of a commercial 3-axes MEMS accelerometer to be used in a robotic system deployed in extreme radiation environments. The research aimed at highlighting the system performance degradation with increasing level of total ionizing dose due to gamma irradiation. Even without proper understating of the device-level

degradation or failure mechanism, based on the irradiation data the authors could provide a mitigation strategy that increased the system useful operating time. Here we report a generalization of such a methodology with proton beams to evaluate the radiation response of a commercial 6-axis integrated inertial navigation system (accelerometer, gyroscope) LSM6DS33 of CMOS/MEMS technology manufactured by STMicroelectronics. The use of proton beams allows to investigate in the same session combined TID and DD degradation; additionally, qualitative and quantitative analysis of non-destructive SEE at a system level (namely Single Event Functional Interrupt) can be investigated and, possibly, destructive SEE screening. As far as the beam energy is concerned, higher energy protons of a few hundreds of MeV are more efficient in inducing SEEs through indirect ionization; conversely, protons of a few tens of MeV, thanks to their higher Linear Energy Transfer (LET) and hardness factor, are more effective in probing cumulative damage. In the present investigation, the choice of beam energy is limited by the current availability of the source. The procedure combines both offline measurements, to analyse the effect of cumulative degradation before and after the radiation exposure in terms of accelerometer calibration change, and online testing through I2 C acquisition of the sensor's parameters during the irradiation. Information thus collected allow component screening based on mission parameters: minimum required TID/DD resistance and acceptable frequency of SEFI (as an order of magnitude); additionally, acquisition of the online behaviour of the component allows implementation and test of a fault identification and recovery strategy that could improve the component reliability.

4.2 IRRADIATION SET-UP DESCRIPTION

In summer 2019 two samples of Mini IMU-9 v5 were irradiated at ENEA Frascati Research Centre. The extraction line set-up and budget of materials is the one employed in spring 2019 and already described in 3.4.2. This set-up was selected to capitalize on the dosimetric characterization already performed, it is however not optimized for this specific target. In particular, the large beam size (sigma ≈ 46 mm) determines a uniform irradiation area (60 mm diameter for a ± 10% uniformity) which is very large compared to the DUT size of about 5 x 5 mm^2. This setup is therefore characterized by a very low flux, typical of radiobiology, which is instead inefficient for proton TID irradiation.

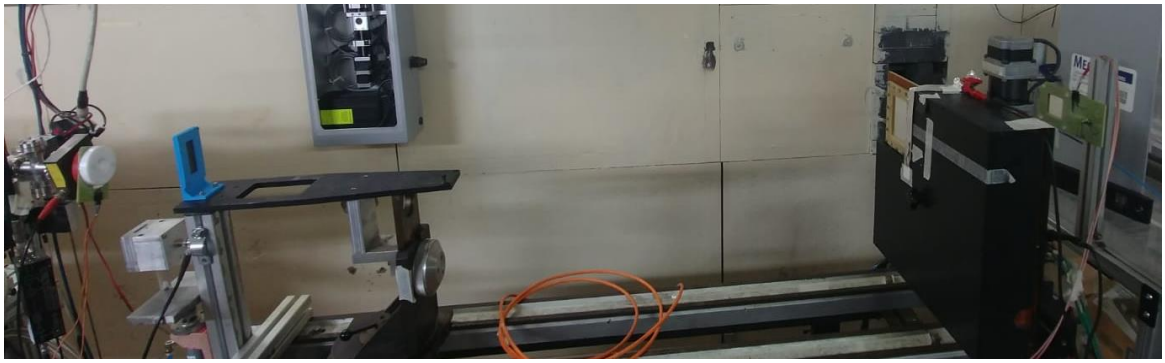

Figure 26 shows the beam extraction configuration in ENEA Frascati bunker and the beam instrumentation. The target position for electronic equipment irradiation was set at 1.8 m downstream the vacuum window, 15 cm behind the segmented ionization chamber (2D IC) which allows intensity and profile measurement of the beam. The 2D IC is used to measure any transverse displacement with respect to the beam axis and can be moved horizontally and vertically for alignment with the proton beam. The device under test is positioned in a dedicated holder, integral to the 2D IC structure, to guarantee its transversal alignment and positioning repeatability (Figure 27).

Beam properties at the target position are summarized in Table 8. Figure 28 shows the acquired dose depth profile in a 10 mm long LiF crystal and the corresponding spectral content obtained from the analytical model and best fit of data. Mismatch in measured/fitted curves are due to artefact in the air/crystal interface (at depth 0 mm) and pedestal due to residual light contribution from the blue lamp used to excite the luminescence.

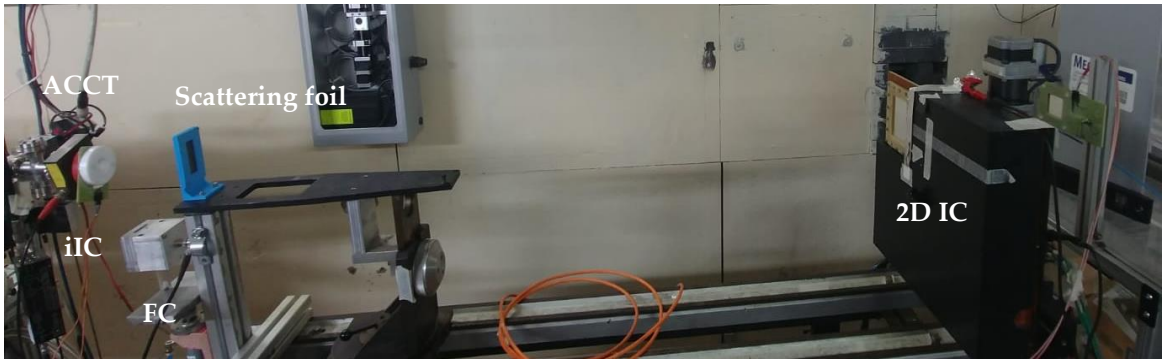

Figure 26 Beam extraction configuration in ENEA Frascati bunker and beam instrumentation: AC current transformer (ACCT), integral Ionization Chamber (iIC), Faraday Cup (FC), scattering foil, 2D Ionization chamber (2D IC)

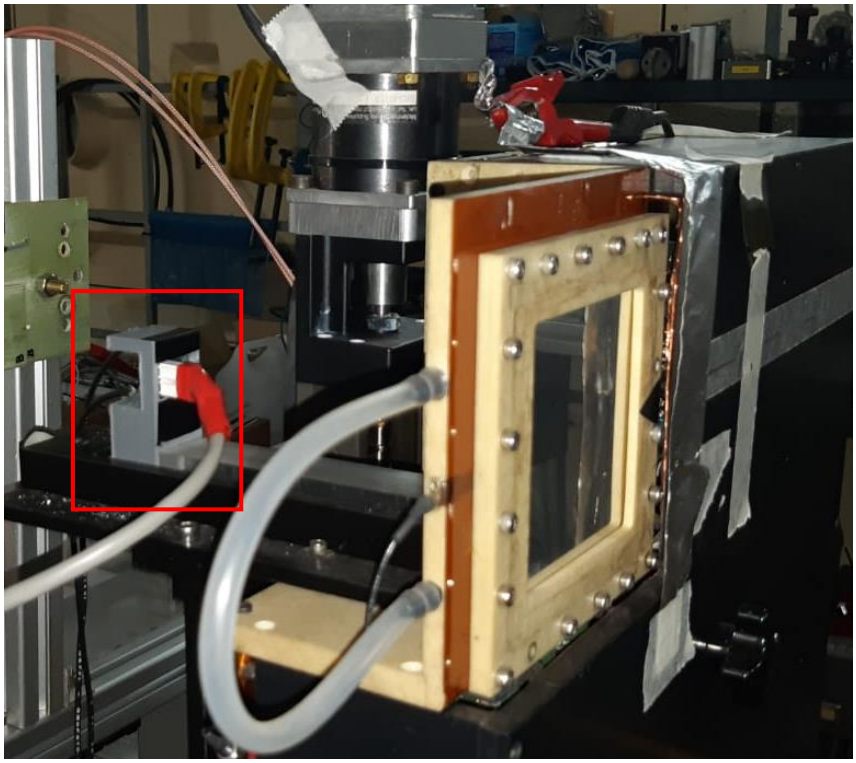

Figure 27 DUT positioned behind the 2D IC

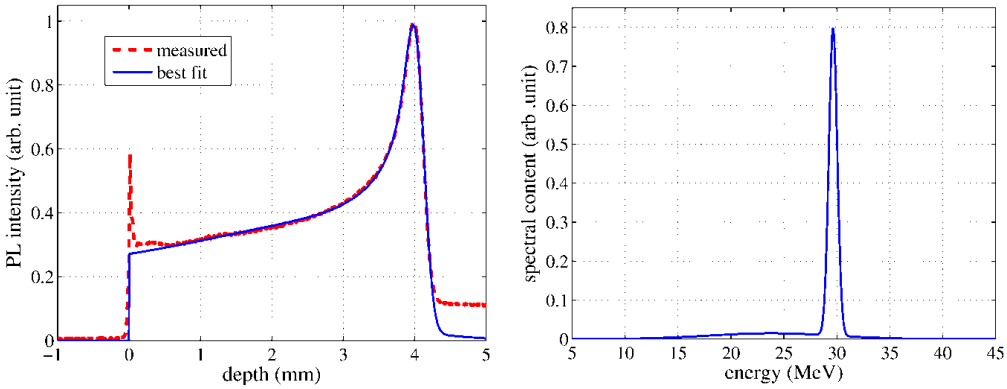

Figure 28 LiF crystal energy measurement: acquired Bragg Peak profile in LiF crystal (top); proton beam spectral content from analytical model and best fit of data (bottom)

Table 8. Beam parameters at DUT

Parameter	Value	Unit
Beam Energy	29.6 ± 0.8 (2σ)	MeV
Transverse size: sigma	46	mm
LET in water	18.9	MeV cm^2 g^{-1}
LET in silicon	14.8	MeV cm^2 g^{-1}
Proton range in Si	4.8	mm
Flux range	10^7 – 10^8	p cm^{-2} s^{-1}
TID range Si (f_{rep} = 25 Hz)	2 - 20	rad s^{-1}

4.3 MEMS INERTIAL NAVIGATION SYSTEM IRRADIATION

The IMU board mounts a LSM6DS33 3-axes gyroscope and 3-axes accelerometer of CMOS/MEMS technology and a LIS3MDL 3-axes magnetometer, both manufactured by STMicroelectronics.

Tests focused on accelerometer and gyroscope behaviour of the LSM6DS33 chip. LSM6DS33 sensors can operate in different ranges and operative modes, the one used for the irradiation test are summarized in Table 9 *(*LSM6DS33 datasheet, https://www.st.com/resource/en/datasheet/lsm6ds33.pdf*)*:

Table 9 LSM6DS33 selected operative mode

Parameter	Value	Unit
Accelerometer range	± 2	g
Linear acceleration sensitivity	0.061	mg/LSB
Gyroscope range	± 245	deg/s
Angular rate sensitivity	8.75	mdeg/s/LSB
Angular zero-rate level	± 10	deg/s
Rate noise density	7	mdeg/s/√Hz
Operating mode	normal	n.a.
Communication protocol	I^2C	n.a.

4.3.1 EXPERIMENTAL METHOD

Characterization of the device degradation in our experimental setup mainly relies on online reading though I2C acquisition of the sensors' parameters. As the DUT is tested in a mechanically static condition, this implies that for the gyroscope only angular velocity offsets can be investigated. For the accelerometer, online data in a fixed position are integrated with offline measurements in the ± 1g range,

allowing investigation of zero-g bias and sensitivity variation of each axis, as will be explained in the next paragraph.

Experimental investigation focuses on the following degradation/failure mechanisms:

- Progressive sensor degradation due to combined TID/DD cumulative effects,
- Device failure dose level,
- Recoverable SEEs,
- Potential disruptive SEEs.

Combination of online and offline monitoring allows following the device parameters degradation, even if only in a specific operating condition, and removing the DUT from the irradiation position for offline characterization only after a certain degradation threshold actually occurs. It prevents unnecessary removal and repositioning of the device, compared to a discrete dose levels characterization scheme. This is especially relevant when there is no prior knowledge of the device expected failure dose level, as is the case for COTS accelerometers that have been reported in literature to show failure levels as low as ~ 10 krad(Si) (Oudea et al., 2009) and up to over 150 krad(Si) (Pitt et al., 2017).

Recoverable SEEs, if detectable at this proton energy, could happen in the form of Single-Event Upsets (SEUs) or Multiple-Bit Upsets (MBUs) in the device ASIC which supervise the calibration of the device analogue signal and its communication with I2C protocol. These could be detected as sudden parameters variation (due to calibration table corruption) or loss of communication. In the current acquisition layout, as the device is monitored on a system level only though the processed parameters, these events could be broadly classified as SEFI: Single Event Functional Interrupt. Identification of these events is left to the operator as no automated fault detection software was implemented in this preliminary experimental setup. At the available acquisition timescale, no transient effect will be investigated.

Disruptive SEEs, namely Single-Event Latch-up (SEL), are considered and monitored through recording of the board current consumption for completeness, even if extremely unlikely to happen at the available proton energy.

4.3.1.1 ACCELEROMETER CHARACTERIZATION

Following the procedure described by (Pitt et al., 2017) the accelerometer readings in 14 different static positions are recorded on a polyhedric support placed on a flat, horizontal surface. The support (Figure 29) was specifically designed to host the IMU board and manufactured in PLA (PoliLactic Acid) with 3D printing technique. With this procedure, several measurements on the ± 1g range are acquired allowing the characterization of the device in terms of zero-g bias and sensitivity of each axis assuming a linear response. In each position the three axes values are acquired 200 times at a 23 Hz rate (which is the pulse repetition frequency of the accelerator); the average sensor reading is used for the characterization. The aim of the characterization is to highlight radiation induced degradation of the device response prior to failure.

A batch of 10 Mini IMU boards was purchased for the experiment. Preliminary measurements of the accelerometers reading in the ± 1g range was performed at Università La Sapienza Guidance and Navigation Laboratory to assess uniformity of the sample IMU board batch. No board was rejected.

Accelerometer characterization is always repeated at ENEA Frascati before the irradiation, 30 minutes after the irradiation (i.e., as soon as activation of the target is below 5 μSv h^{-1}) and one week later. If accelerometer parameters show degradation during the irradiation phase, the DUT is removed and re-characterized offline at different dose steps.

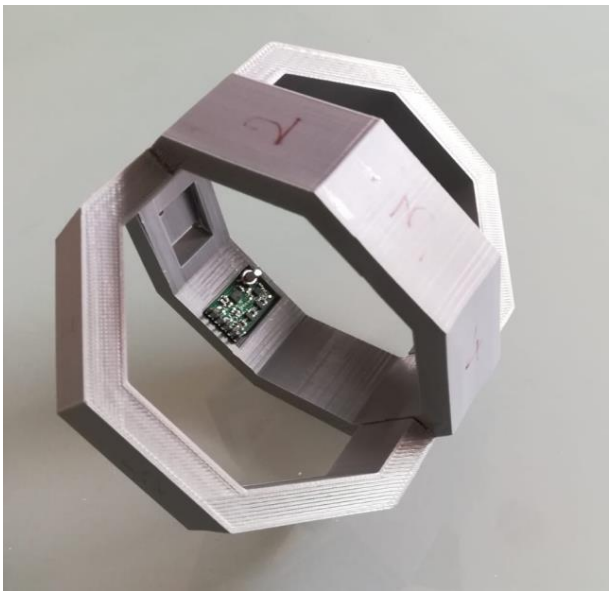

Figure 29 Polyhedric support for accelerometer characterization

4.3.1.2 IRRADIATION PROCEDURE

During irradiation the IMU board is hosted in a dedicated plastic holder obtained with 3D printing (Figure 30). Its external size matches the dimension of the Plexiglas holder used for μDiamond dosimeter calibration at the target position. With this setup, the geometrical centre of the IMU board lies on the beam axis and the board is normal to the incident beam. The LSM6DS33 chip is therefore entirely contained into a 10 mm diameter area centred on the beam axis. As the beam profile at the DUT position is Gaussian with a sigma of 46 mm, the fluence experienced by the DUT differs from the nominal fluence at the beam centre, characterized with the μDiamond dosimeter, less than 1%.

The following IMU parameters are monitored online:

- accelerometer reading (3 axes),
- gyroscope reading (3 axes),
- temperature sensor,
- board current.

The IMU board communicates to an Arduino module via digital (I^2C) interface; a dedicated Matlab user interface shows and records IMU data on a PC in the accelerator control room via Ethernet connection. Data acquisition and transfer are synchronous with the accelerator repetition frequency, 25 Hz. This timing configuration was chosen to be able to correlate any sudden accelerator anomaly with device behaviour.

In the first irradiation experience (sample No 1), no remote power cycling was implemented. As the first set of data suggested evidence of recoverable single-event effects, remote power cycling was later implemented and employed for irradiation of sample No 2. Remote power sampling was non automated and operated manually by the user after a suspected SEFI event was observed,

Beam is delivered in pre-set amounts of total charge, expressed in monitor units of the integral ionization chamber, and recorded by the iIC. Once the total charge is reached, beam extraction is suspended. While it is possible to manually stop the irradiation, the presently available beam delivery interface does not allow automatic beam vetoing.

Dose was delivered in ~2 krad(Si) steps, corresponding to a fluence of ~ 8 10^9 proton cm^{-2}. Average dose-rate for sample nr. 1 was 15 rad(Si) s^{-1}; average proton flux was 6 10^7 p cm^{-2} s^{-1}; sample nr. 2 was irradiated at lower dose-rate of 10 rad(Si) s^{-1} corresponding to a proton flux of 4 10^7 p cm^{-2} s^{-1}. For both samples total proton fluence was 2.2 10^{11} cm^{-2}, corresponding to a TID of ~ 55 krad(Si) and a 50 MeV proton equivalent fluence of ~ 2.8 10^{11} cm^{-2}.

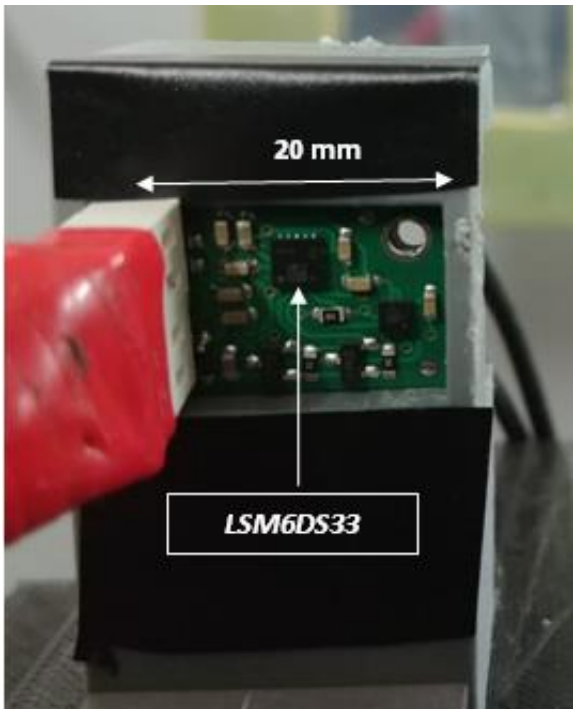

Figure 30 Mini IMU board in plastic holder used for irradiation tests

4.3.2 EXPERIMENTAL RESULTS

Figure 31 and Figure 32 summarize data from the irradiation of the first and second IMU samples. Data are represented versus cumulated dose.

In both samples, gyroscope and accelerometer show a consistent behaviour, at least form a qualitative point of view: accelerometer reading is stable, except for abrupt transitions; gyroscope offset instead drifts with increasing dose and is also affected by abrupt transitions.

As previously mentioned, in the first irradiation no power cycling of the device was operated; at dose ~ 20 krad(Si) the gyroscope reading shifts abruptly, followed

by a loss of communication (i.e. all output data are equal to 0.0). Similarly, at dose ~ 50 krad(Si), the accelerometer output parameters change abruptly. The device does not recover unless a power cycle is operated. Irradiation of sample No 2, where remote power cycling was implemented, showed that power cycling of the device after such transitions always resulted in recovered functionality therefore we can conclude that both IMU samples were still operating after a TID irradiation of over 55 krad(Si).

The temperature sensor reading is very sensitive to radiation as it can be seen in Figure 33: its average value decreases and rms noise increases when irradiation is on. Note that the increasing trend is due to actual temperature increase in the accelerator bunker, which was monitored independently, as shown in Figure 34. The last few data points of Figure 11 were recorded at double dose-rate irradiation, eventually resulting in the device loss of communication for a few hours. The measured temperature spike (nearly 40 °C, still well within the device operative limits) might therefore not be physical but due to effects not yet understood.

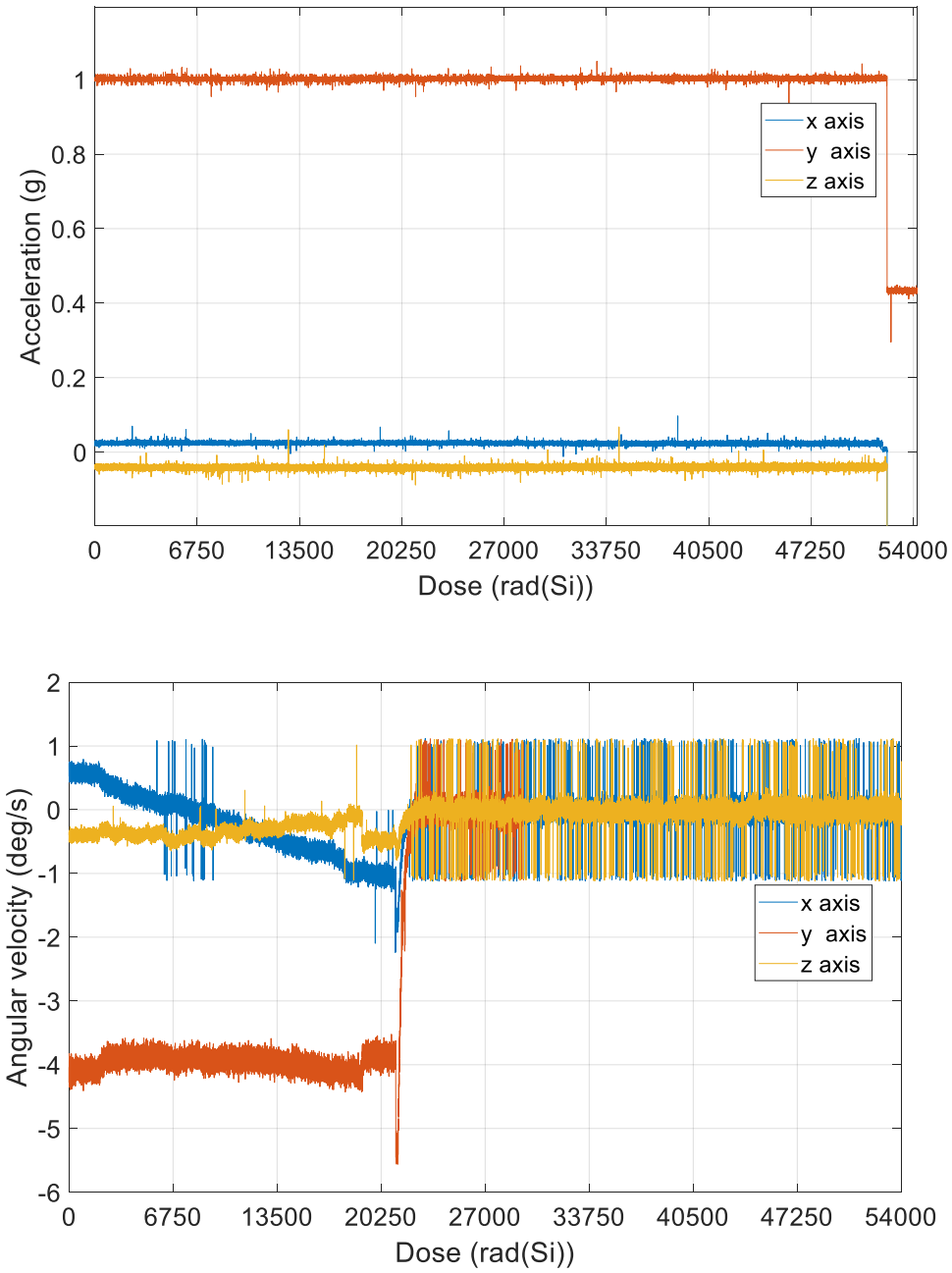

Figure 31 Accelerometer (top) and gyroscope (bottom) data from sample no. 1

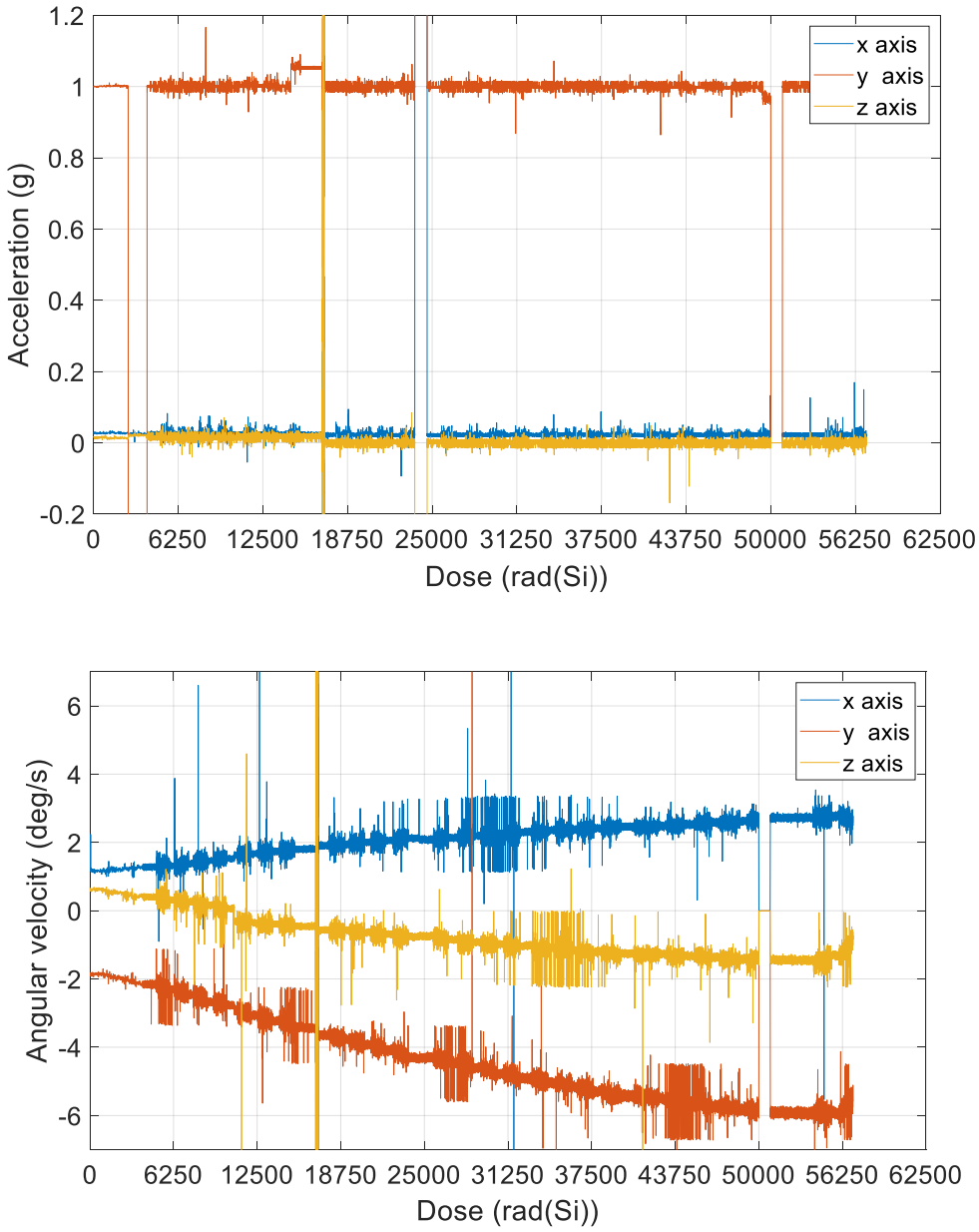

Figure 32 Accelerometer (top) and gyroscope (bottom) data from sample no. 2

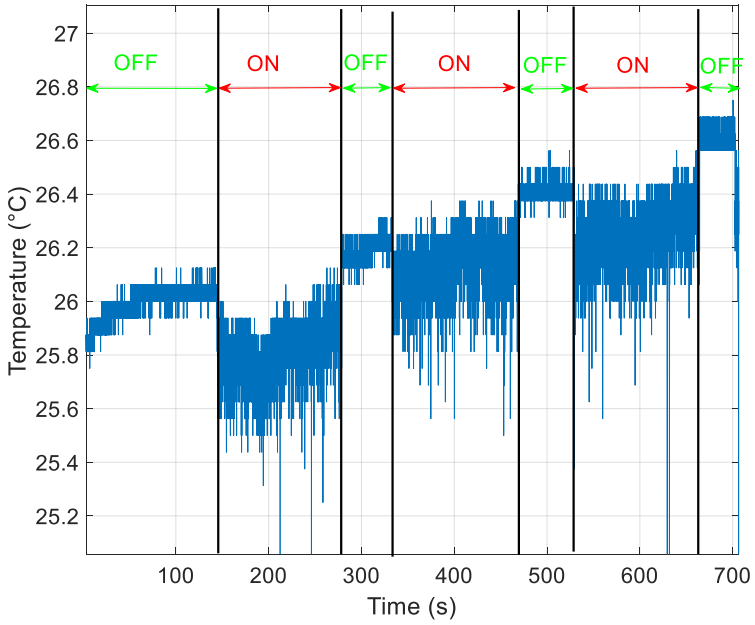

Figure 33 Detail of temperature sensor behaviour in beam on/off conditions (sample no. 1 irradiation)

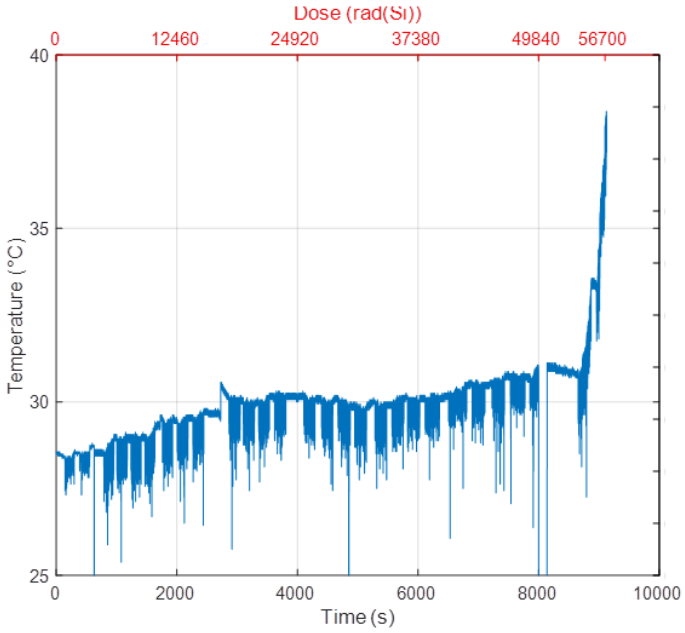

Figure 34 Temperature sensor data - sample no. 2 irradiation

4.4 SENSORS DATA DISCUSSION

Experimental data of gyroscope and accelerometer can be interpreted as a combination of deterministic and stochastic effects. The first category includes progressive sensor degradation due to combined TID/DD cumulative effects and eventual device failure, which was not observed. In the latter category are recoverable SEEs, as no disruptive events were recorded.

4.4.1 DETERMINISTIC EFFECTS

Accelerometer and gyroscope outputs are affected by proton irradiation in a deterministic way. These effects can be due to both TID, DD or a combination of the two, but it is beyond the scope of this research to separate the two effects. A new irradiation campaign with photons, either few MV X-rays or Co^{60} γ-rays, could highlight the TID-only contribution. Both devices show an increase in rms noise when the beam irradiation is ongoing, much in the same way as the temperature sensor. Typical noise levels are recovered immediately after irradiation. Please note that "beam off" and "beam on" conditions differ only in the proton extraction from the source: other sources of electromagnetic noise, especially RF power, are the same. Dependence of noise level with dose-rate seems likely but has not been investigated yet.

The two sensors instead differ deeply in measured value response, as discussed in the following section.

4.4.1.1 ACCELEROMETER The accelerometer output values on the 3 axes are not affected up to the maximum dose of 55 krad(Si), as already shown in Figure 31 and Figure 32. This dose is well over the typical requirement for university CubeSat projects, corresponding, as an order of magnitude, to over 3 years of operation in polar LEO orbit with very light shielding, but it is still well below the TID failure level assessed for other COTS MEMS accelerometers, as already mentioned.

Characterization measurements before and after irradiation confirm the findings on the ± 1g range at least within the sensitivity of such a procedure. Figure 35 shows calibration data for sample nr. 2.

4.4.1.2 GYROSCOPE

Due to the static nature of the irradiation setup only angular velocity offsets could be investigated in this first experiment and no calibration procedure was foreseen beforehand.

The gyroscope output values are immediately affected by the beam presence, as highlighted in Figure 36 where the first few seconds of irradiation of sample nr. 1 are shown.

The beam presence induces a drift in the angular offset values which is different in amplitude and sign for the tree axes. The two samples showed the same qualitative behaviour, but amplitude and sign of the drift appears to be random. After an irradiation step, drift can persist in the short term. A few hours after irradiation, offset values settle, as demonstrated by comparison of data at the end of the irradiation session (Figure 32, bottom) and 12 hours afterwards (Figure 37). Power cycling does not affect the drift process. Please note that for both IMU samples the final angular velocity offset was still within the datasheet specifications (± 10 deg/s).

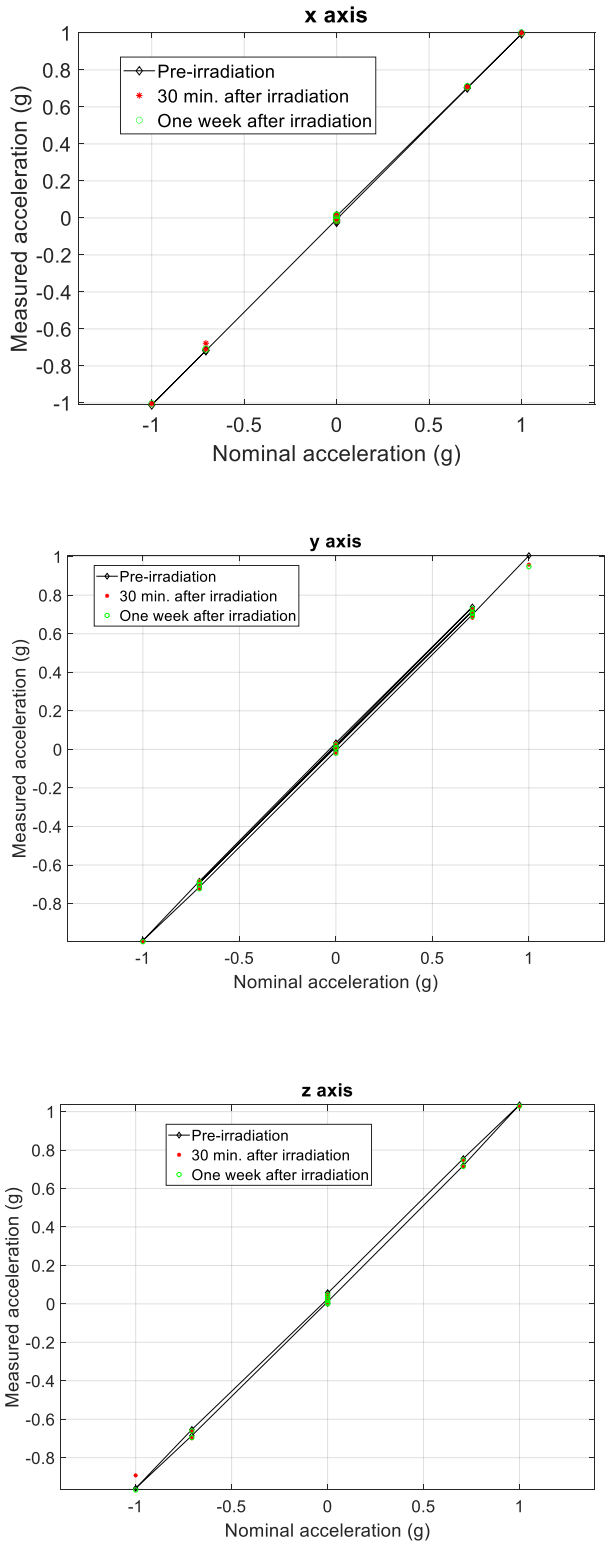

Figure 35 x-axis (top), y-axis (middle) and z-axis (bottom) accelerometer calibration data before and after 55 krad(Si) irradiation – IMU sample no. 2

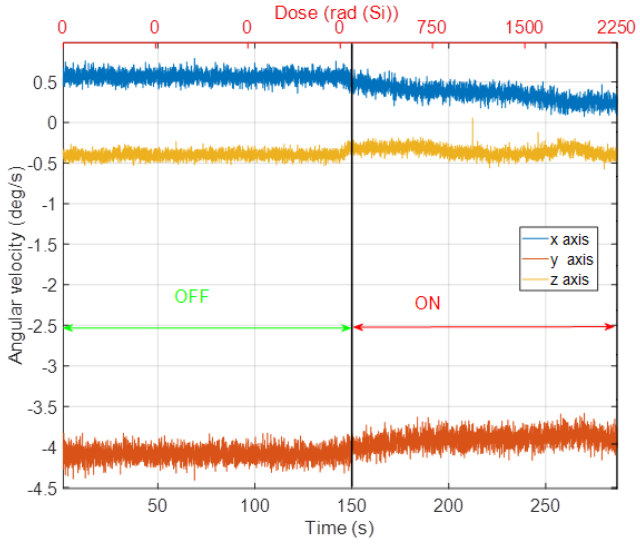

Figure 36 Detail of gyroscope offset values behaviour at irradiation beginning – IMU sample no. 1

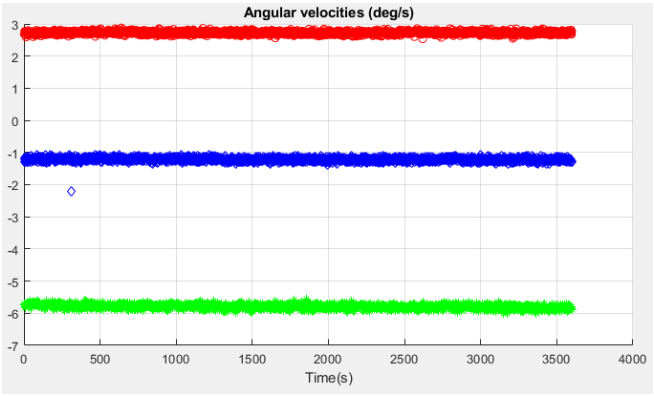

Figure 37 Gyroscope offset values behaviour 12 hours after irradiation – IMU sample no. 2

The gyroscope noise trend from sample no 2 is investigated as a function of time comparing beam on and off conditions. Standard deviation is calculated in 100 samples step (at 25 Hz acquisition frequency 100 samples are a 4 seconds time window). Figure 38 shows the comparison of the two data sets: in beam off condition the standard deviation increase is compatible with temperature increase dependence given by the datasheet (0.05 deg/s/°C); in beam on condition, no trend in standard deviation is visible and the absolute value is always at least twice the datasheet value (7 mdeg/s/√Hz ~ 0.039 deg/s at 32 Hz cutoff frequency).

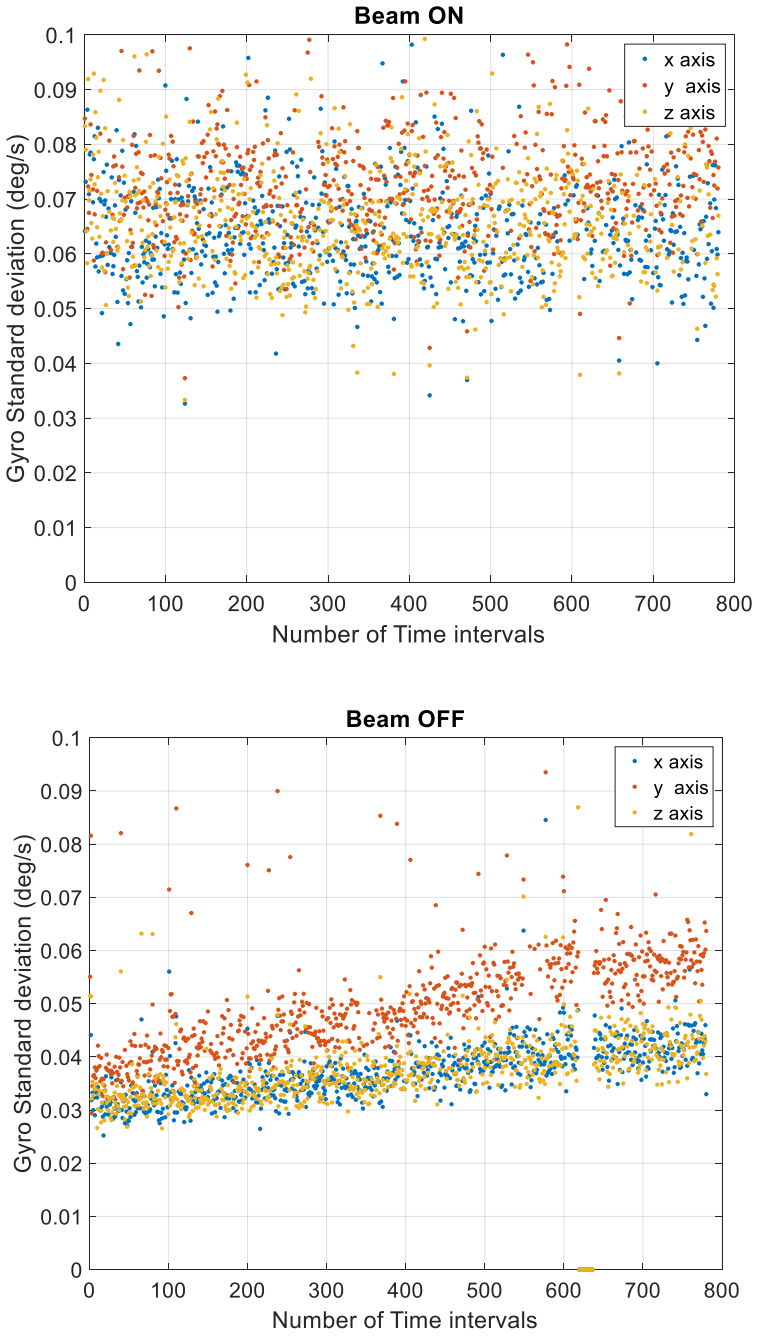

Figure 38 Gyroscope standard deviation values at 4 seconds time interval: beam on (top) and beam off (bottom) comparison.

4.4.2 STOCHASTIC EFFECTS

Single-event effects are triggered by charge deposition in sensitive volumes of electronic equipment due to the incident ionizing radiation. The higher the linear energy transfer of the radiation, the higher the probability to induce SEE.

Proton beams may induce SEE either by direct ionization or by inelastic scattering with a target nucleus or by nuclear reaction, resulting in the emission of a higher LET particle. Low energy protons, such as used in our experiment, have relatively higher LETs but are less likely to produce secondary, highly ionizing particles than high energy protons (> 200 MeV) typically used for SEE tests.

4.4.2.1 DESTRUCTIVE SEE (SEL)

Analysis of destructive single-event effects on critical parts is the minimum risk evaluation requirement even for very short mission in benign environment (eg. 1-year lifetime in LEO equatorial orbit) (Campola & Pellish, 2019). While extremely unlikely to happen with proton beams of this energy, in our experiment we did monitor single-event latch-up events through acquisition of the device power consumption: sudden increase of power consumption followed by device failure would be classified as a SEL event.

No SEL events were observed in the two irradiation sessions after irradiation of over $2\ 10^{11}$ p/cm^2. This sets therefore the following limits:

$$\text{SEL proton } E_{threshold} > 29.6 \text{ MeV}$$

for irradiation at room temperature.

4.4.2.2 NON-DESTRUCTIVE SEE (SEFI)

The device under test is made up of two different sensors built with MEMS technology and an ASIC for digital communication, control, and acquisition of the sensors. Our system level analysis does not allow precise investigation of the different specific effects that happen at part level.

What we can instead detect are SEFI, i.e. a soft error that causes the component to reset, lock-up, or otherwise malfunction, by the definition of (*ESCC Basic Specification No. 25100 - SINGLE EVENT EFFECTS TEST METHOD AND GUIDELINES*, 2014). While non-destructive, SEFI events directly affect the component reliability and availability in mission condition and the evaluation of

their rates is an important part of risk assessment. Two main types of SEFI are distinguished depending on the actions required to restore operability: reset by software or by power cycling. In our case, no reset by software was implemented therefore only direct power cycling is taken into account in our examination.

Recorded events occurred into two main categories:

- reading error events:
  at least one axis reading of one sensor experience an instantaneous (i.e. in less than 40 ms, our time resolution) change in output value; "out of range" events (i.e. accelerometer stuck at +2*g* or – 2*g*);

- communication impairing events:
  the device ceases to communicate or communicates only null values for both sensors.

Quantitative analysis is limited by the very low number of events and by the irradiation procedure itself as no automatic SEFI detection and power cycle procedure was implemented. Moreover, cross section data are limited to sample no. 2 irradiation, since no power cycling was implemented in the first irradiation. Assuming a poissonian uncertainty on the number of recorded events and 10% fluence uncertainty:

$$\sigma_{SEFI}\ (29.6\ \text{MeV}) = 3.0\ 10^{-11} \pm 1.3\ 10^{-11}\ \text{cm}^2$$

A correlation between SEE events frequency and TID could in principle exist, but the limited statistics does not allow quantitative evaluation.

4.5 PROTON IRRADIATION DISCUSSION

The test goal of the proton irradiation campaign was to evaluate a simple procedure that could be applied in typical University projects that would often rely on COTS components and boards: while lacking the completeness of standard test procedures, online and offline digital acquisition of the device parameters in static conditions allowed a qualitative and quantitative description of the component behaviour and minimum set of possible failure modes to be characterized. Degradation up to a total ionizing dose of 55 krad(Si) and displacement damage dose of 50 MeV proton equivalent fluence of 2.8 1011 cm-2

was investigated; Recoverable single-event effects were recorded and, even if with high uncertainty, cross section for SEFI was measured.

Analysis of this first irradiation campaign highlighted how the procedure can be improved.

With the plan to repeat the acquisition at higher proton energy, as the TOP-IMPLART accelerator evolves, to characterize the SEFI cross section on the largest available energy span the following action could be taken:

- development of specific software for the DUT monitoring to include a SEFI events detection and classification software. This would improve reliability of the analysis and possibly allow simultaneous irradiation multiple IMU boards
- a modification, or even the development of a specific irradiation delivery control system, separated from the one used for radiobiology studies, to allow the automatic suspension of irradiation when certain condition of the DUT are me (eg. a SEFI)
- a new mechanical set up that would either take advantage of the large homogeneous spot to irradiate simultaneously multiple board or, on the contrary, a different irradiation set up with a smaller irradiation spot but higher flux, for faster qualification
- additionally, comparison of DUT irradiation with X-rays or γ-rays, planned in a different ENEA facility, could improve the understanding of the degradation and failure mechanism separating TID effects from DD and single-event effects.

4.6 IRRADIATION WITH X-RAYS

The use of proton beams has the advantage to simultaneously probe degradation mechanism due to combined Total Ionizing Dose and Displacement Damage Dose and failure modes due to Single Event Effects. Additionally, and especially for LEO targeted missions, protons are representative of the actual radiation environment that the device could be subjected to.

On the other hand, if understanding of the specific degradation mechanisms, rather than a "simulation" of the radiation environment, are the focus of the research, protons are the least desirable radiation source. To specifically probe TID

effects, Cobalt-60 (^{60}Co) and Cesium-137 (^{137}Cs) radioisotopes are the preferred sources as they guarantee maximum reproducibility. Alternatively, X-rays and low energy electron beams produced by particle accelerators are also commonly employed as operation of these sources is flexible and more secure.

A new irradiation campaign with X-rays conducted on the same DUT at the REX Facility in ENEA Frascati in summer 2020. REX is based on a linear accelerator producing 4.8 MeV electron beams and bremsstrahlung X-rays via a removable conversion head with tungsten target. The use of complementary radiation sources (X-rays, low energy electrons and protons) allows verification of the cause of degradation on the IMU performance that have already been observed with proton irradiation by separation of cumulative from stochastic effects: noise increase, bias changes (attributed to TID) and zero or end of scale readings, loss of communication (attributed to SEE).

4.6.1 RADIATION SOURCE: THE REX FACILITY

The experimental campaign was conducted at the REX facility of ENEA Frascati Particle Accelerator Laboratory, which is based on an S-band standing wave linac which produces 4.8 MeV electron beams. The accelerator operates delivering 3 μs long charge pulses at a variable repetition frequency and with a peak current of 140 mA. The accelerated electrons are extracted in air through a 50 μm Titanium window and can be used directly or converted to bremsstrahlung X-rays thanks to a removable radiation conversion head. For the reported activity, a 1.6 mm Tungsten foil is employed for electrons to X-rays conversion. A 0.5 mm thick aluminium foil, placed downstream a conical lead collimator, absorbs any remaining electrons components. The extracted photons are characterized by a broad energy spectrum, with a maximum equal to the energy of the primary electron beam. This facility is employed in different fields, mainly cultural heritage preservation and material characterization for nuclear fusion reactors ((Vadrucci, Borgognoni, et al., 2019) (Borgognoni et al., 2017)). A detailed description of the REX facility and characterization of the available photon spectra can be found in (Vadrucci, Ferrari, et al., 2019).

4.6.2 DOSIMETRIC CHARACTERIZATION

Sample irradiation is performed in air within a 400 x 400 x 500 mm^3 chamber shielded with 10 cm thick lead walls. Dose rates and dose uniformities can be

varied (for both X-rays and electron) choosing different geometrical layout inside the irradiation chamber. Details on the dose mapping simulation and verification for the REX implant can be found in (Vadrucci, Ferrari, et al., 2019). Active and passive dosimetric techniques employed at the REX facility are calibrated for dose to water-equivalent targets. However, in the energy range of photons produced in this facility, the ratio of mass-collision stopping power for water and Silicon is such that evaluated dose is the same, at least within a typical 10% accuracy (see for instance (Ravotti, 2018)).

For the present work, a DUT distance from the extraction window of 20 cm was selected. At 20 Hz pulse repetition frequency, the nominal dose rate at the target position is 12 rad/s. This value is similar to the dose rates used in the proton irradiation campaign, i.e. 10 −15 rad/s. Total dose verification is performed with two alanine pellets irradiated together with the DUT, as detailed in the next paragraph.

4.6.3 EXPERIMENTAL SETUP

To obtain meaningful data to compare with proton ones, the experimental procedure strictly follows the one of the previous campaigns. First the accelerometer is characterized offline in the ± 1g range: thanks to a polyhedric support placed on a flat, hard surface, the acceleration components (a_x; a_y; a_z) are acquired in 14 different configurations. This allows a full characterization of each axis in terms of offset and sensitivity, assuming a linear response. Afterwards the IMU is irradiated in a fixed position, normal to the X-ray beam, and operation parameters are acquired online with the same procedure and instrumentation of the proton irradiation campaign.

Figure 39 shows the DUT mounted on the 3D printed support and the 2 alanine pellets for dose verification (highlighted in red) above and below the IMU board; Figure 40 shows the device aligned inside the irradiation chamber. The support height is such that the geometrical centre of the board lies on the beam axis.

Data acquisition from the IMU board is performed via I^2C protocol by an Arduino module. Due to the limited cable length (30 cm, same as for proton irradiation experiment) the Arduino box is placed inside the accelerator bunker, just outside the lead shielded irradiation chamber. The same module handles data transfer to

the operator PC in the accelerator control room via Ethernet connection. The PC runs a Matlab script for data visualization and logging. Acquired variables are:

- Acceleration (3 coordinates)
- Angular velocity (3 coordinates)
- Temperature
- IMU board current consumption

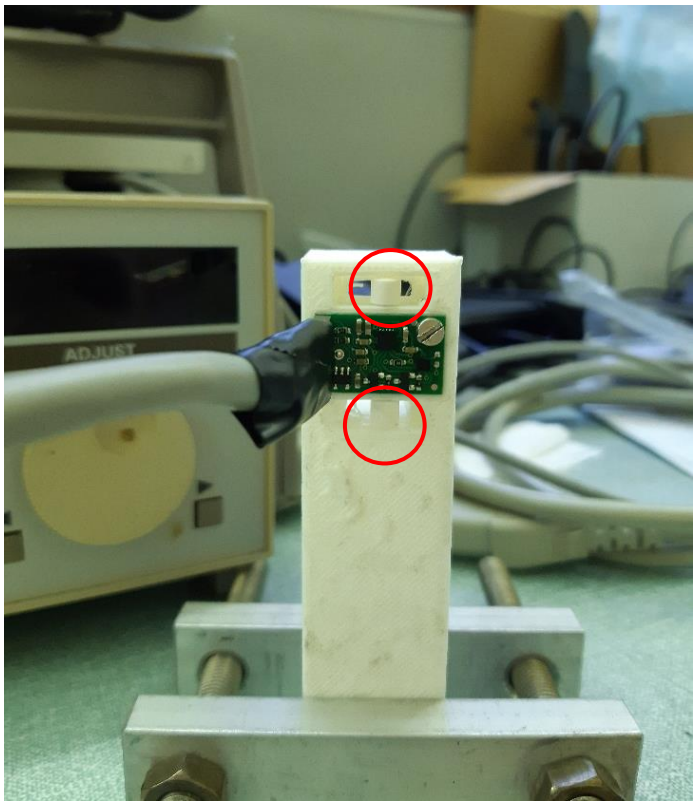

Figure 39 IMU board and alanine pellets positioned on the support (highlighted in red).

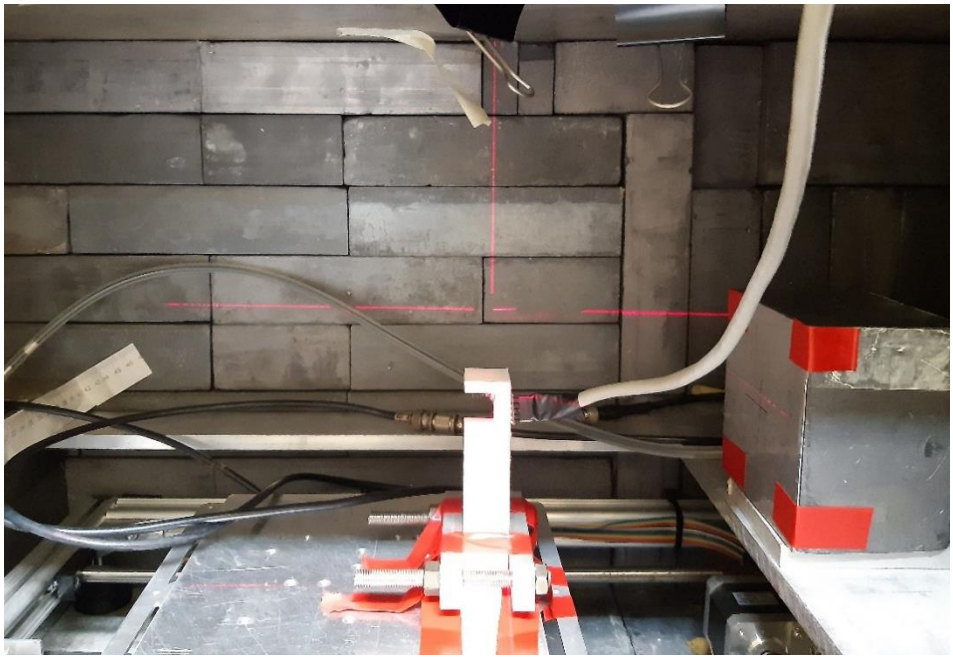

Figure 40 IMU board aligned inside the irradiation chamber.

4.6.4 IRRADIATION PROCEDURE

Irradiation procedure is similar to the one performed with proton beam and can be summarized as follows:

1. Offline characterization of the accelerometer
2. Board communication test without beam extraction
3. Irradiation at fixed time intervals (30 minutes; c.a. 20 krad(Si)) with online monitoring of the device parameters; irradiation is paused if accelerometer degradation or device failure is detected before the pre-set dose is completely delivered
4. Fixed time (30 minutes) irradiation suspension (to prevent accelerator & conversion target overheating)
5. Accelerometer offline characterization is repeated if significant degradation is detected from online measurement and always at the end of a test session.

It must be noted that even if the dose rate of protons and X-rays are the same, the whole irradiation sessions durations were rather different. This is due to the different dose delivery systems and overheating prevention requirements for the two accelerators. The overall irradiation session with X-rays lasted less than 2 hours, while with protons it lasted over 4 hours.

4.6.5 RESULTS

Two boards from the same batch were irradiated in two separate days with the same setup and procedure. Results are fairly consistent, especially considering the large variability which is typical of COTS products. Both IMUs received a full 30 minutes irradiation (i.e. ~ 20 krad(Si)) and were still operating; both showed failure in the following irradiation session, at a total dose of over 30 krad(Si).

4.6.5.1 BOARD FAILURE DISCUSSION

Online acquisition of the board parameters showed how the absorbed current and temperature sensor data can be used to identify the board failure threshold. Figure 41 show the signature behaviour of the temperature sensor, which rises abruptly, paired with a similar sudden increase in absorbed current. This sudden rise is followed by a loss of communication from the device. In Figure 42 is reported a temperature data set acquired in the proton irradiation campaign showing the same pattern. While qualitatively the observed behaviour is the same for X-rays and proton irradiation, suggesting TID is the predominant mechanism, the threshold doses for this phenomenon are quite different: over 55 krad(Si) for protons and 30 krad(Si) for X-rays. Such a discrepancy is too big to be explained as a dosimetric error; it suggests that possibly the proton effective dose rate should be accounted for, as in the proton case the whole irradiation lasted about twice as long with respect to the X-rays one.

The DUT can later regain some functionality (after ~ 2 days) if no irradiation is resumed. After recovery, the accelerometer and gyroscope readings are consistent with the latest measured values, but the absorbed current remains above 2 mA and temperature over 40 °C. Note that independent measure of the IMU board temperature with a thermoscanner show that the device never actually reached such a high temperature. From literature, such as (Pitt et al., 2017), we expected to observe a progressive degradation of the two sensors before the overall board failure. Analysis of the irradiated boards showed how the DUT malfunction was actually due to failure of the 3.3V LDO voltage regulator which caused the LSM6DS33 to operate at the limit of its specification. Once the LDO was removed from the board and a separate 3.3 V voltage supplied from the Arduino controller, the temperature sensor recovered its correct behaviour, thus corroborating our hypothesis that the DUT actual failure dose should be much higher. To correctly

assess its level the irradiation must be repeated in the future removing the LDO from the board.

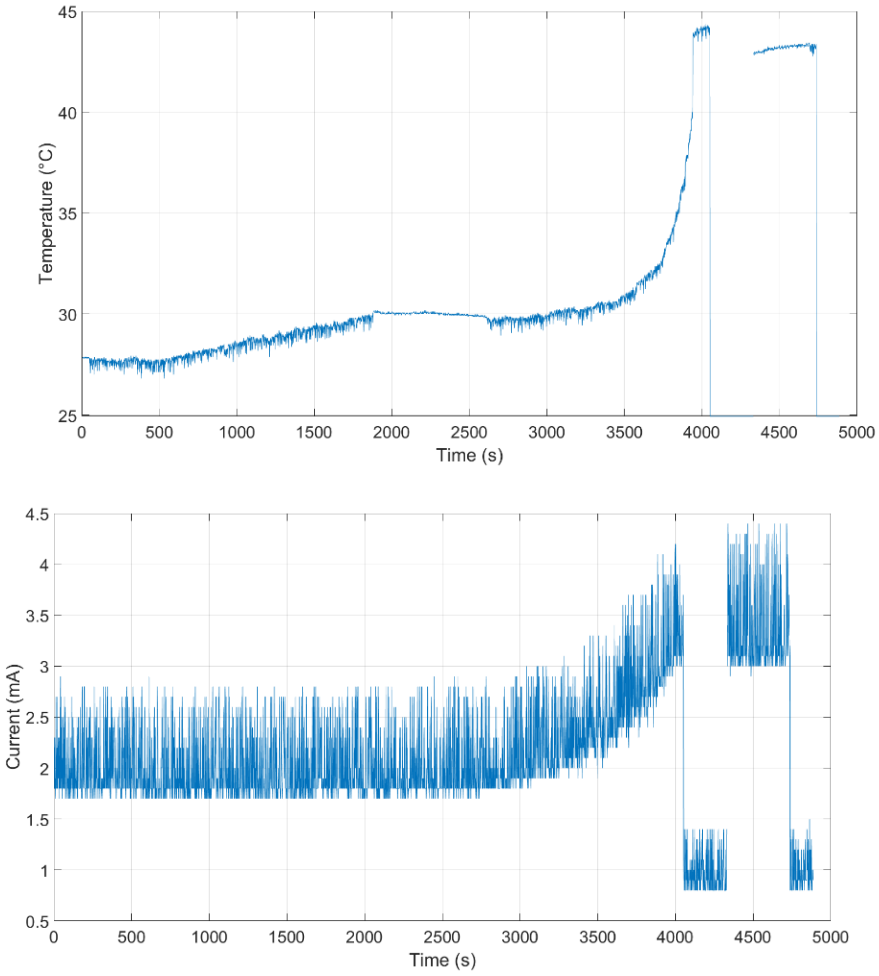

Figure 41 Absorbed current (bottom) and temperature sensor data (top).

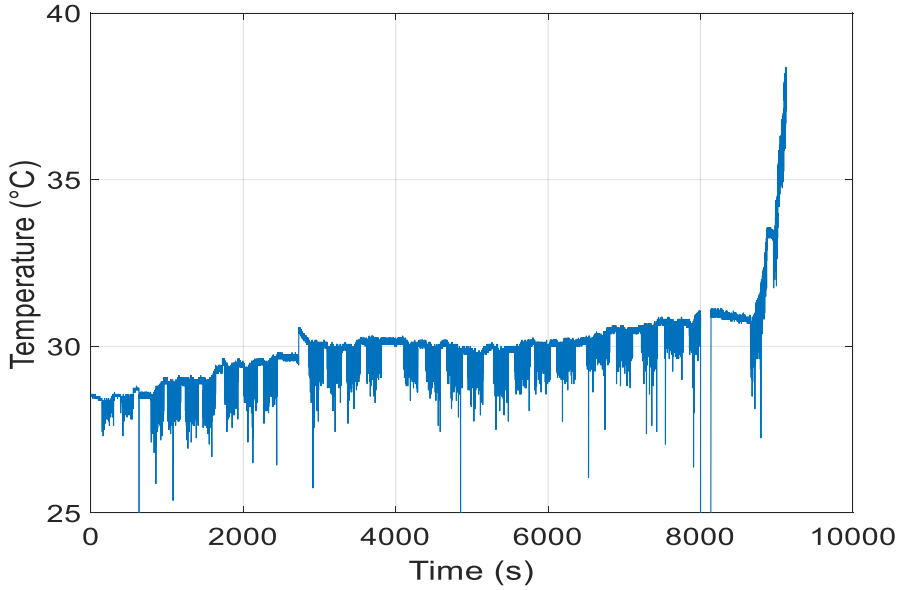

Figure 42 Temperature sensor data from a proton irradiation of the same DUT

4.6.5.2 SENSORS DEGRADATION

The accelerometer, gyroscope and temperature sensor behaviour with X-rays irradiation is qualitatively the same as with protons irradiation, suggesting the main cumulative degradation mechanism can be attributed to TID. It can be summarized as follows:

- All sensors show an increase in RMS noise only when irradiation is switched on; in Figure 43 an example is given for the temperature sensor
- The accelerometer readings are stable (at least until overall board failure at time ~ 4000 s), as shown in Figure 44
- The gyroscope shows a bias drift on the three axis which increases with increasing dose, as shown in Figure 45

Sudden, recoverable events such as zero or end of scale readings and loss of communication were not recorded with X-rays irradiation. This was expected, as such effects were attributed to SEEs.

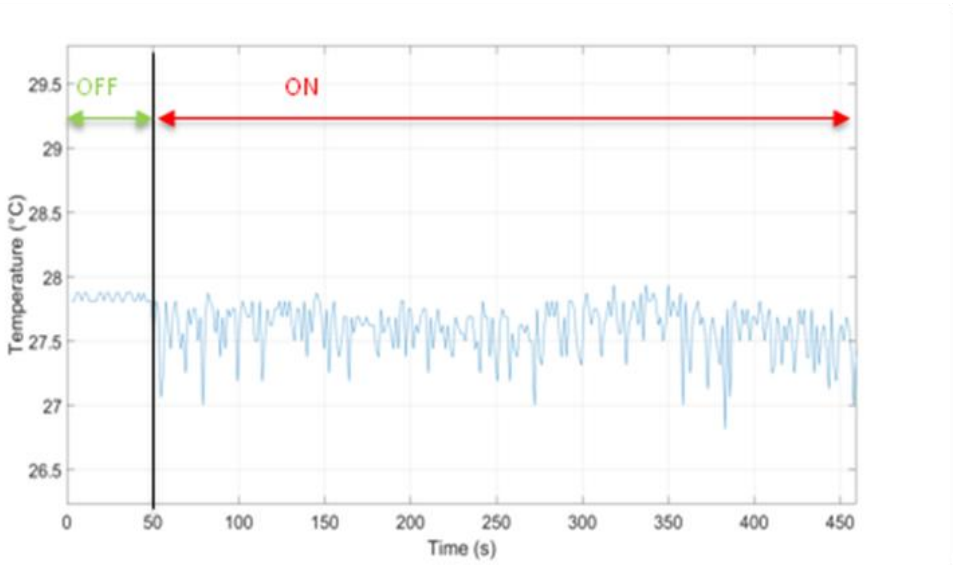

Figure 43 Temperature sensor data: detail of the noise increase effect when the irradiation is switched on

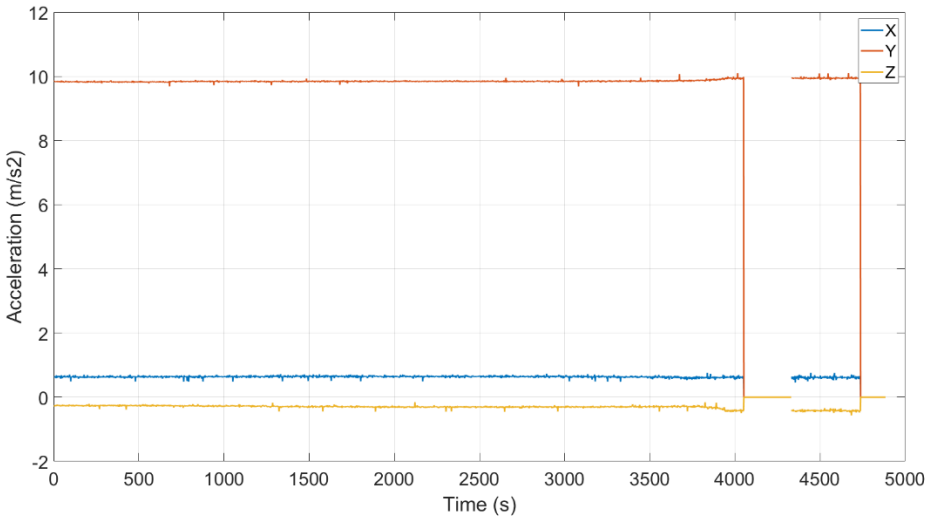

Figure 44 Accelerometer acquisition

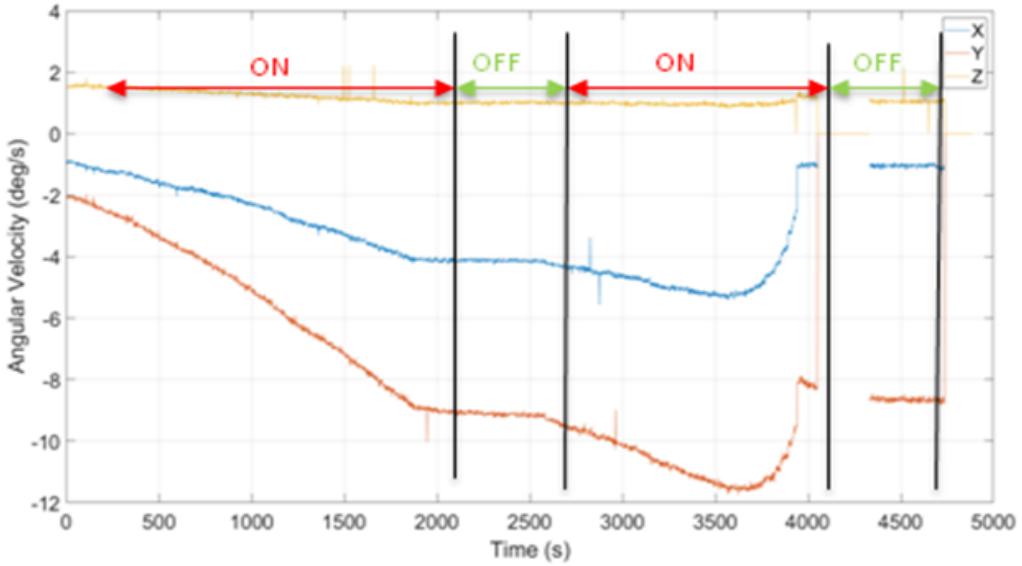

Figure 45 Gyroscope acquisition

4.7 X-RAYS IRRADIATION DISCUSSION

This pilot experiment demonstrated that TID is the main cause of the LSM6DS33 deterministic degradation. The X-ray beam produced by the REX facility is an efficient source to test the device degradation at higher dose levels once the voltage regulator is removed from the board. Irradiation with X-rays confirmed the sensitivity of the gyroscope. Mechanically static irradiation, though, only enables characterization of the angular velocity bias.

Based on these results new irradiation tests and set-ups were considered but could not be executed due to the very limited beam time availability and material procurement issues.

Planned activities are:

- New test campaigns to verify the effectiveness of the combination of online and offline measurements to properly characterize the accelerometer progressive degradation up to higher TID
- Development of a mechanical setup to allow online acquisition of the accelerometer and gyroscope data in a mechanically dynamic configuration. The IMU board is kept orthogonal to the incident beam

and moved along an arc within the 90% dose uniformity area with a motorized rotating support. The frequency of oscillation shall small (<< 1 Hz) compared to the REX linac operating frequency (20 Hz) and will be varied to simulate acceleration condition representative of either manoeuvres or gravity gradient stabilization.

- Test with 5 MeV electrons: even if they are not a typical source for radiation hardness assurance, they are still representative of the actual LEO environment, therefore we are interested in developing a suitable irradiations setup for space application. Preliminary dosimetric characterization is ongoing with the goal of finding a large enough uniform spot to perform irradiation moving the DUT but with not too high a dose rate.

Chapter 5
SEU MEASUREMENTS ON ESA MONITOR

This irradiation campaign was a collaboration with CERN R2E (Radiation to Electronics) group. The specific project was devoted to the comparison of proton and neutron induced Single and Multiple Event Upsets susceptibility of different SRAMS, including both commercial products and radiation tolerant devices developed within the RADSAGA project (https://radsaga.web.cern.ch/). Results of the irradiation campaign, which involved multiple facilities, was presented at the IEEE data workshop of NSREC2020 (Coronetti et al., 2020) and is published in (Cecchetto et al., 2021).

For the ENEA laboratory the collaboration provided the opportunity to test our dose delivery system accuracy with the ESA monitor, which acts as a cross reference tool between European facilities, and, through the interaction with the CERN colleagues, to develop internal procedures and adopt best practices apt for planning and execution of "standard" RHA irradiation campaign.

5.1 THE ESA MONITOR

The so-called "ESA Monitor" is a reference SEU monitor developed by ESA based and first introduced to the RADECS (RADiation Effects on Components and Systems) community in 2005. Due to the extensive characterization and highly reproducible manufacturing of the Atmel AT60142F SRAMS that constitute the sensitive element of the detector it is a simple and reliable beam monitor device to be used both by the accelerator facilities and the SEE experimenters. Preliminary

characterization of the detector was carried out at different ESA facilities: the Proton Irradiation Facility (PIF) in Switzerland, the Heavy ion Irradiation Facility (HIF) &Light Ion Facility (LIF) in Belgium and at the RADiation EffectsFacility (RADEF) in Finland. Additionally, the Reference SEUMonitor system has been used by Hirex Engineering, ONERA, CEA and by several projects within ESA. The ESA Monitor is also part of the Technology Demonstration Module on board the PROBA-II satellite (Harboe-Sørensen et al., 2008) launched in 2009.

The SEU cross section for the ESA monitor is now well characterized at different facilities at different proton energies and heavy ions species (Bisello et al., n.d.; Noordeh & Garcia Alia, 2014). In particular, the R2E group of CERN carried out a systematic calibration campaign with their ESA monitor detectors (Garcia Alia & Cecchetto, 2020). It is therefore a cross calibration instrument for different radiation sources: if the beam energy is well known it provides feedback on the accuracy and reproducibility of the fluence measurement system of other facilities. Measurement with the ESA Monitor constituted therefore independent verification of our beam delivery system calibration, based on methods different from those derived from clinical or radiobiological researched that are otherwise applied at TOP-IMPLART.

In Figure 46 is shown the ESA Monitor of CERN R2E group installed on the TOP-IMPLART beamline. The device is equipped with a lid that can be removed to expose the die before the irradiation. In the figure, the four SRAMs that constitute the active part are clearly visible. Each element has a size of 11.2 x 6.1 mm^2, the total sensitive area is ≈ 20 x 20 mm^2. Beam profile and homogeneity can be evaluated from the mapping of the physical locations of the SEUs.

The qualification procedure requested by the R2E group foresee a preliminary characterization of each irradiation set up with the ESA Monitor to verify transverse homogeneity and cross section consistency with the literature data. This is followed by irradiation of the SRAMs, which were the investigated devices.

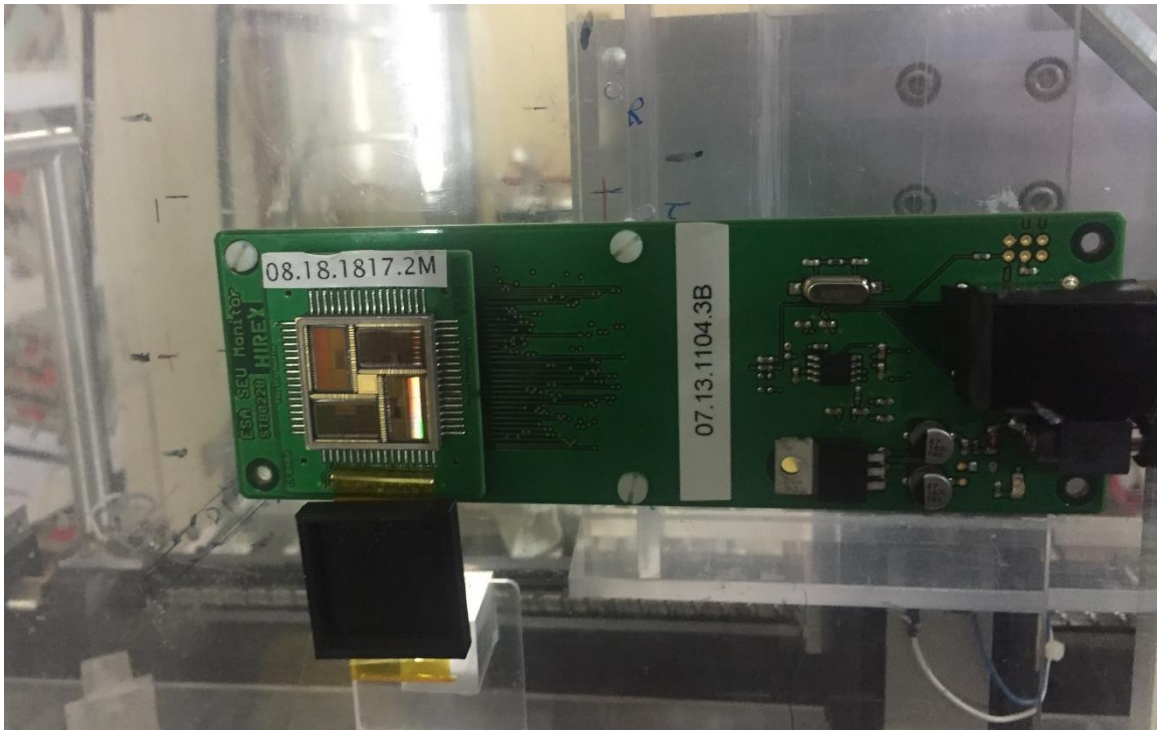

Figure 46 ESA Monitor board (owned by CERN) positioned on the TOP-IMPLART beamline

5.2 IRRADIATION SET-UP

5.2.1 BEAMLINE LAYOUT

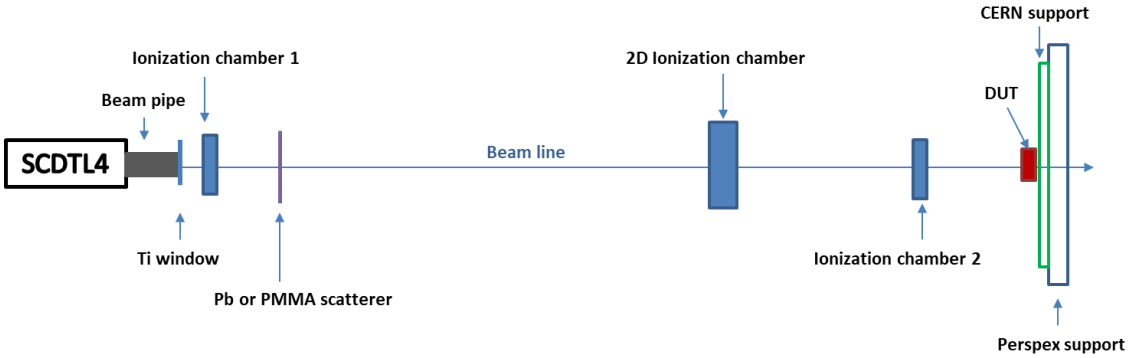

Figure 47 Beam line setup for the CERN R2E irradiation campaign

Table 10 List of materials encountered by the proton beam

	Distance from SCDTL4 (mm)	Thickness (mm)	Material
Beam pipe	181	181	vacuum
Titanium window	181.05	0.050	Titanium
Lead or PMMA scatterer	390	0.210 (Pb) / 5 (PMMA)	Lead / PMMA
2D Ionization chamber	1595	0.170	Water equiv
DUT	2015	-----	-----
Perspex support	2045	-----	-----

The schematic layout of the irradiation setup for the CERN R2E group irradiation campaign is shown in Figure 47 and Table 5 list the geometry details and budget of materials. The layout is based on a radiobiology campaign which took place a few days before this irradiation to take advantage of the dose and energy measurement already performed with this setup. The Devices Under Tests (DUT) reference position is on a Perspex plate support which belongs to a motorized phantom for radiobiology tests of the Istituto Superiore di Sanità. With this configuration the longitudinal DUT position lies 3-4 cm of air before the reference position which was qualified for the radiobiology experiments. We consider the impact of 3 cm of air in energy, fluence and uniformity determination to be negligible within the overall uncertainty of our setup characterization.

Experiments were repeated at two energy values: one (29 MeV) is obtained with the Lead scatterer as in the "standard" setup; a lower one (18 MeV) is obtained substituting the lead scatterer with a PMMA degrader of 5 mm thickness. For each energy, two current intensities were used, labelled "high flux" and "low flux" configurations, approximately a factor 4 apart.

Two ionization chambers are used for irradiation delivery: ionization chamber 1 is positioned immediately after the titanium window, ionization chamber 2 is about 10 cm before the Perspex plate. Differently from previous irradiation campaign, this setup foresees ionization chamber 2, the one closer to the DUT, as the principal beam delivery monitor. This configuration closely resembles the actual on for protontherapy where the dose delivery monitor is placed in air less than 1 m before the patient and the beam does not intercept anything else in between and should provide a better representation of the dose to the target with respect to the previously used set-up, relying on ionization chamber 1, which is positioned

immediately after the titanium vacuum window and is sensitive to the LINAC extracted charge.

5.2.2 DUT SUPPORT AND ALIGNMENT

The Perspex plate acts as a reference plane, as it is already aligned with the beam, and a mechanical support. CERN setup consists of a 24 x 24 cm² Plexiglas board mounted on a metallic frame. The board has multiple sets of holes to hosts different electronic boards and guarantee that the DUT is always positioned at the centre. For faster device switching and to limit the contact with the component immediately after their irradiation, two Plexiglas boards were available and were alternated. Alignment of the different DUTs is therefore simplified as only the metallic frame needs to be aligned on the reference Perspex support. Figure 48 shows the Perspex support dimensions and alignment details. In Figure 49 are shown the different DUTs, their sizes and positioning on the CERN Plexiglas board.

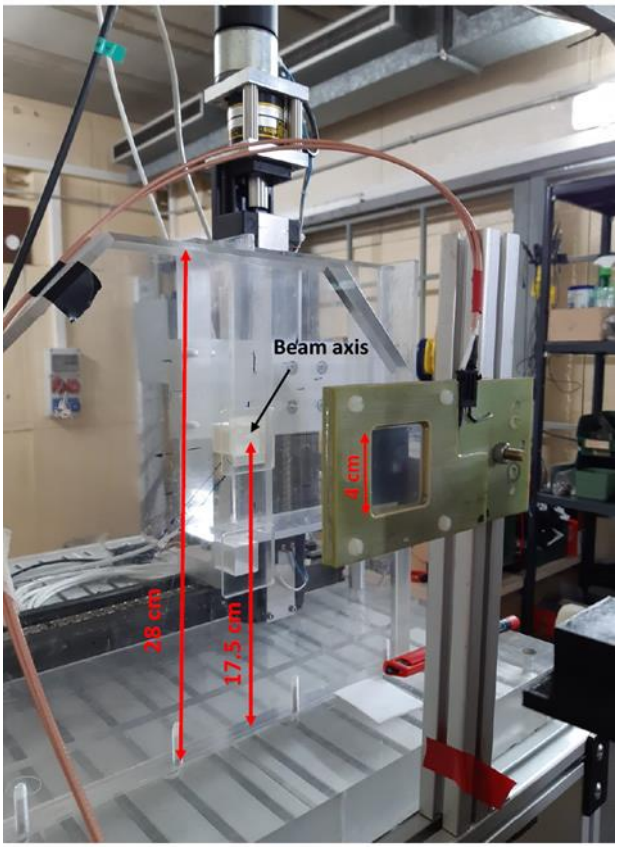

Figure 48 Alignment details for the CERN irradiation: reference Perspex plane size and beam axis position; Ionization chamber 2 is also shown

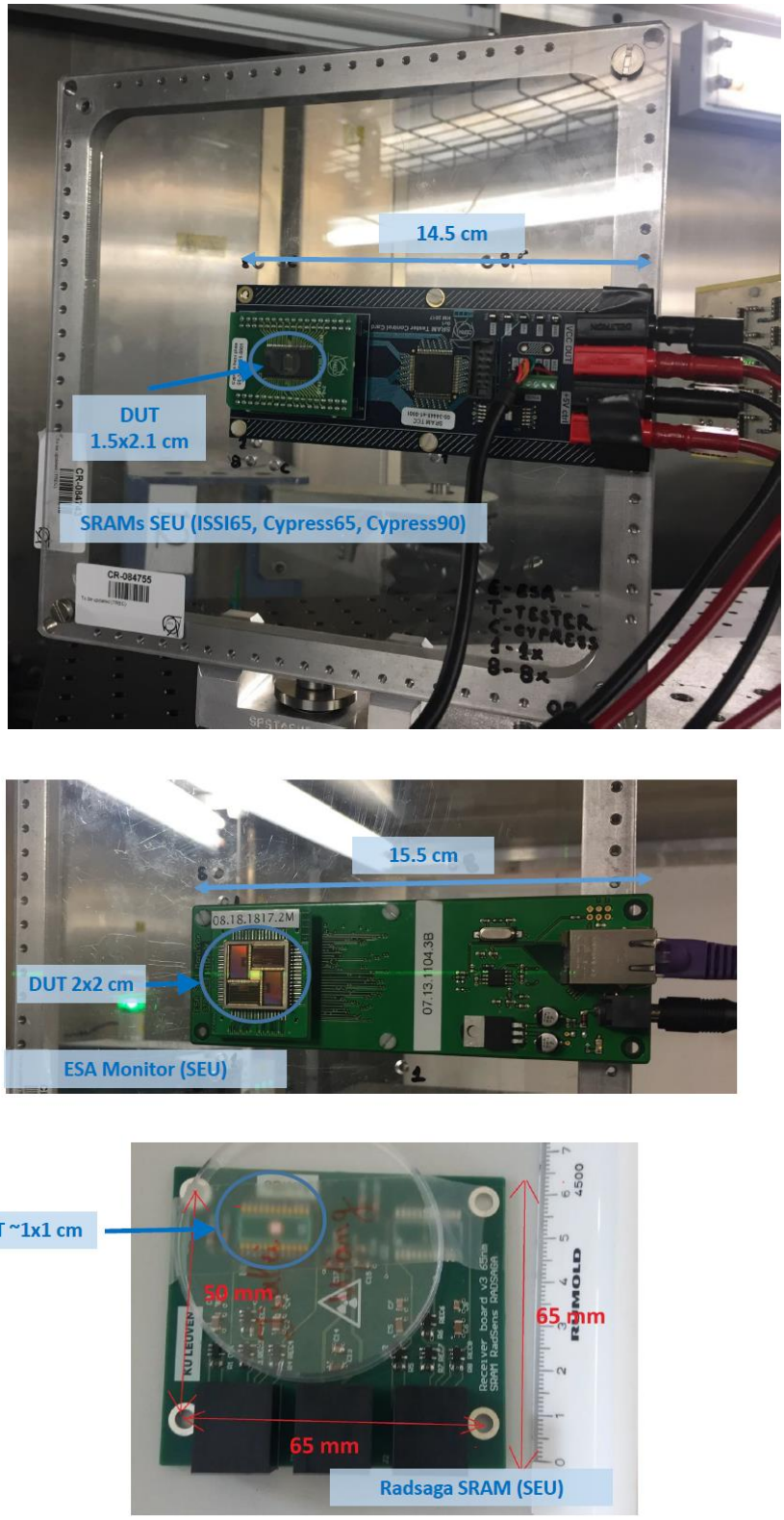

Figure 49 DUTs sizes and positioning details on the Plexiglas board: commercial SRAMs (top): ESA monitor (middle); Radsaga SRAM (bottom)

5.3 BEAM PARAMETERS AT THE DUT POSITION

5.3.1 SRIM CALCULATIONS

The figures and tables below summarize the beam properties at the DUT position as computed with SRIM/TRIM calculations: beam energy, transverse distribution and proton average LET (in water and Silicon) at the target position.

5.3.1.1 29 MEV SETTING

Table 11 Summary of beam properties at DUT position for the "29 MeV" setting: SRIM/TRIM computations

Parameter	Value	Unit
Beam Energy	29.13 ± 0.26 (1σ)	MeV
Transverse size: sigma	47	mm
Average LET in water	19.4	MeV cm^2 g^{-1}
Average LET in silicon	15.1	MeV cm^2 g^{-1}

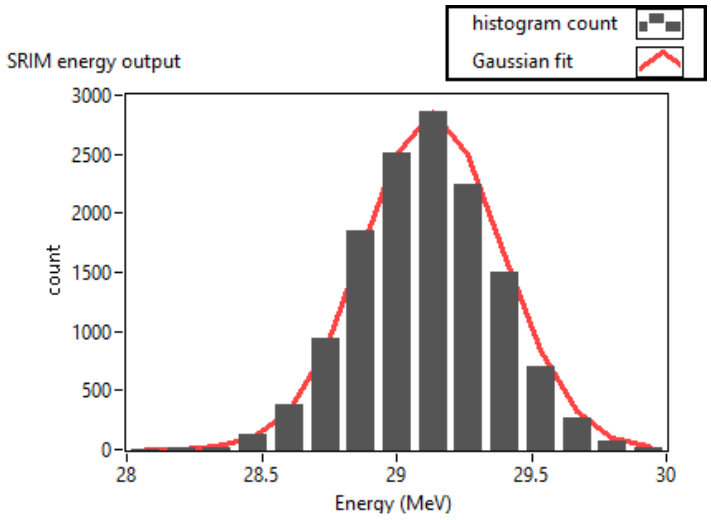

Figure 50 Beam energy distribution at the DUT position for the "29 MeV" setting: SRIM/TRIM computations

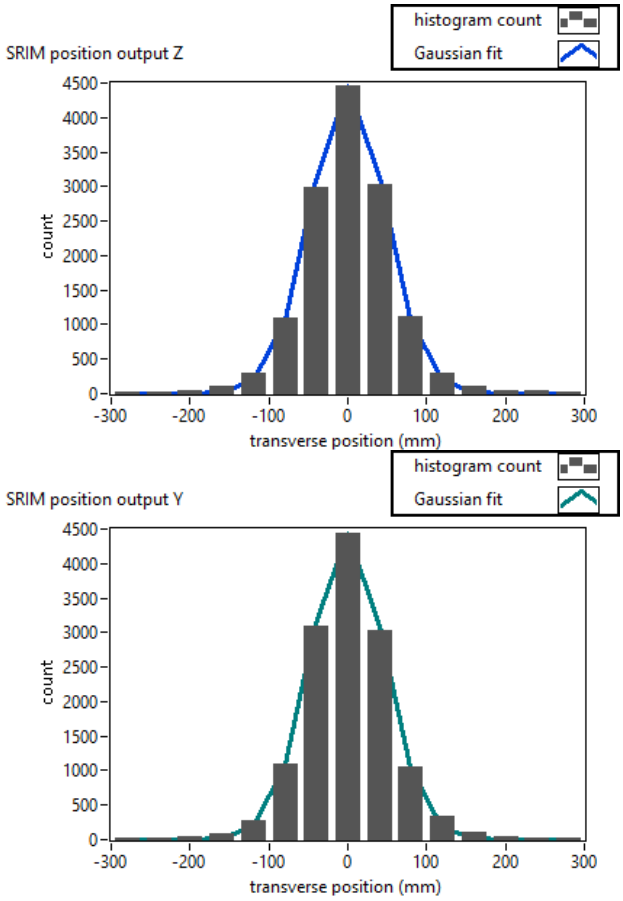

Figure 51 Beam transverse distribution at the DUT position for the "29 MeV" setting: SRIM/TRIM computations

5.3.1.2 18 MeV SETTING

Table 12 Summary of beam properties at DUT position for the "18 MeV" setting: SRIM/TRIM computations

Parameter	Value	Unit
Beam Energy	18.80 ± 0.44 (1σ)	MeV
Transverse size: sigma	34	mm
Average LET in water	27.4	MeV cm^2 g^{-1}
Average LET in silicon	21.2	MeV cm^2 g^{-1}

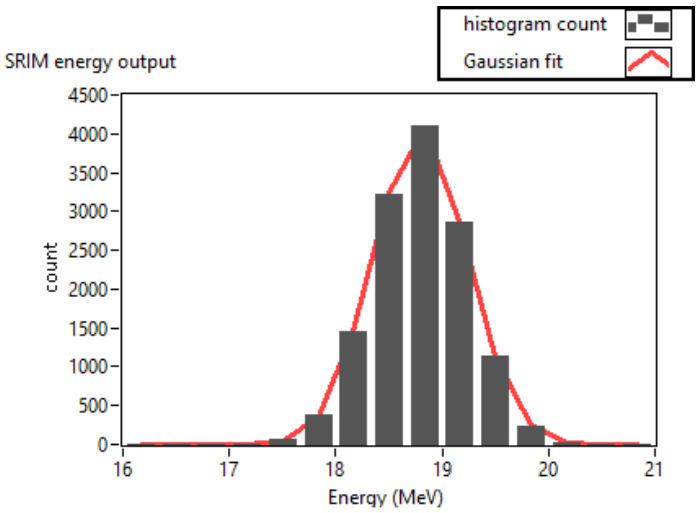

Figure 52 Beam energy distribution at the DUT position for the "18 MeV" setting: SRIM/TRIM computations

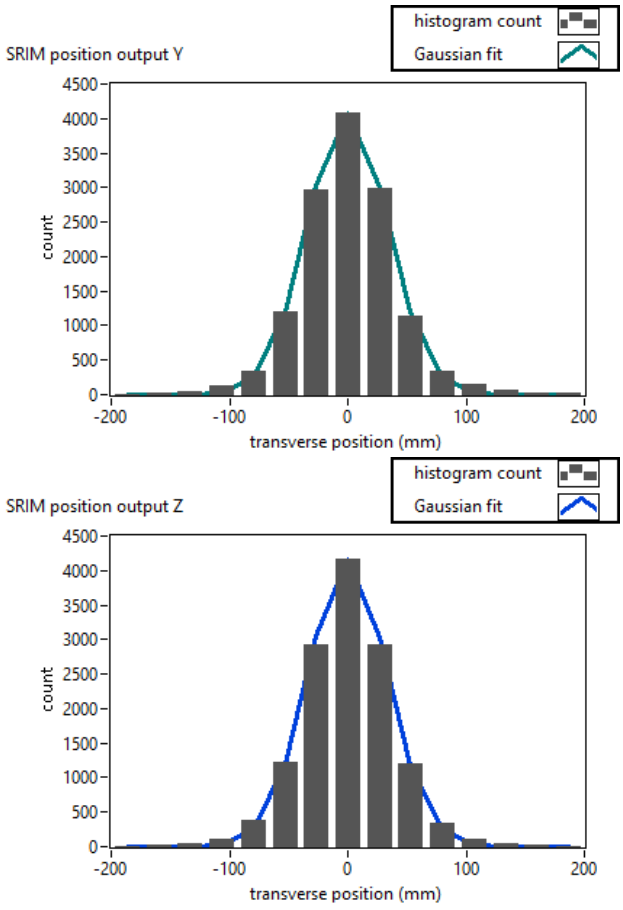

Figure 53 Beam transverse distribution at the DUT position for the "18 MeV" setting: SRIM/TRIM computations

5.3.2 TRANSVERSE HOMOGENEITY

The transverse homogeneity in the "29 MeV" setup, i.e., with the Lead scattering foil, was verified for the radiobiology experiment demonstrating a uniformity better than ± 5% on a 40 mm diameter. In the "18 MeV" case we rely on SRIM calculations: the expected beam sigma at the DUT position is 34 mm, corresponding to a homogeneity of ± 10% on a 30 mm diameter. This result is more than acceptable for electronic equipment test, especially given the small size of the DUTs.

5.3.3 ENERGY MEASUREMENT AND CALCULATION

Beam energy in the two setups is verified by experimental LiF crystal Bragg peak imaging. The LiF crystal position is 409 mm of air downstream the 2D ionization chamber. Bragg Peak profile in LiF and the corresponding spectral content is shown in Figure 54.

Agreement with the measurement is found for both setups within a typical uncertainty of less than ± 0.2 MeV, as summarized in Table 13.

Beam energy at the μDiamond dosimeter sensitive area position (i.e., 1 mm water equivalent depth) is then calculated with SRIM. The μDiamond is positioned 375 mm of air downstream the 2D ionization chamber; the DUT is positioned ≈ 5 mm of air before the μDiamond, but this difference is negligible within the energy verification uncertainty of ≈ ± 0.15 MeV. The energy at the μDiamond sensitive position is given in Table 13.

Table 13 *LiF measurement and SRIM calculation comparison for the two energy setups*

Extracted beam configuration	**Beam energy @ LiF position (LiF measurement)**	**Beam energy @ DUT position (SRIM output)**	**Beam energy @ μDiamond position (SRIM output)**
Lead scattering foil ("29 MeV" setup)	28.79 ± 0.18 MeV	29.1 MeV	27.0 MeV
Plexiglass degrader ("18 MeV" setup)	18.72 ± 0.11 MeV	18.8 MeV	15.8 MeV

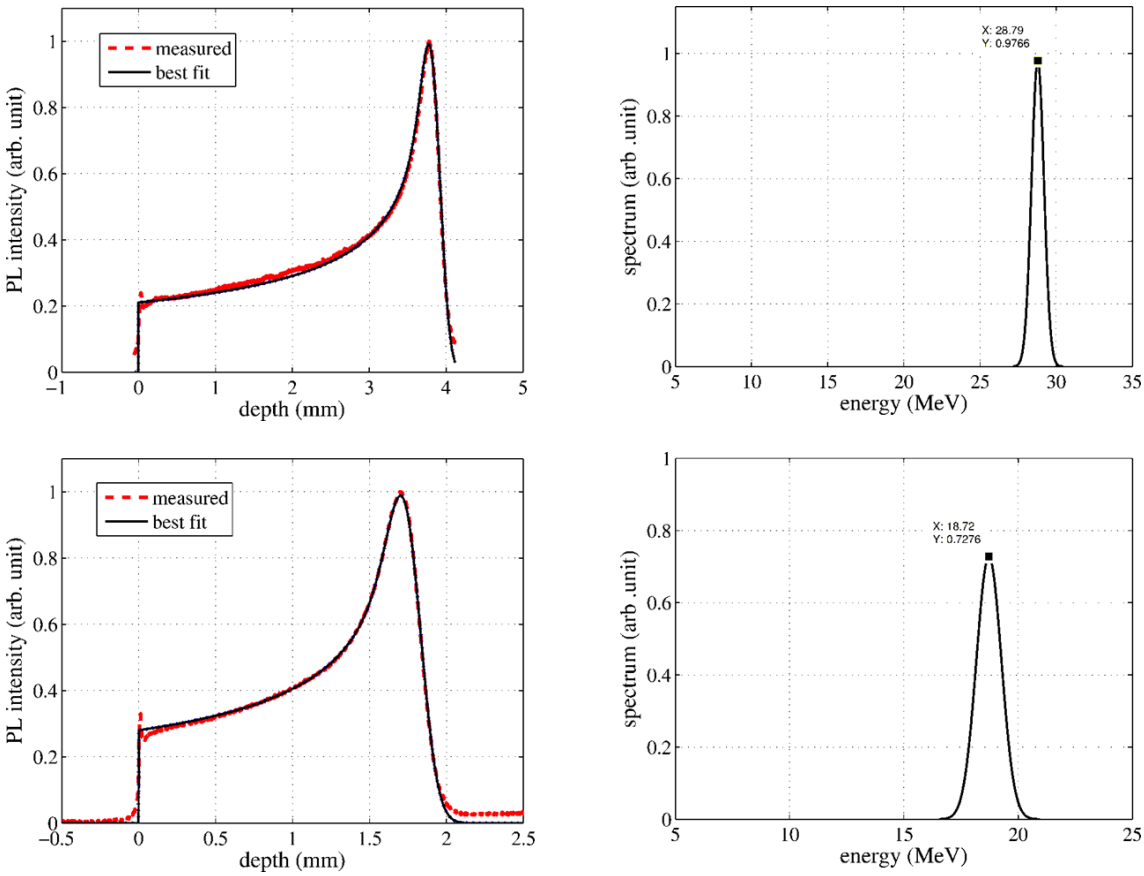

Figure 54 Energy measurement with LiF for the two energy configurations: "29 MeV" (top) and "18 MeV" (bottom)

5.3.4 FLUENCE DETERMINATION

Energy at the μDiamond dosimeter is used to convert dose reading in water to the equivalent proton fluence Φ with the usual relation:

$$D[Gy] = 1.602\ 10^{-10} \cdot\ \Phi\ [cm^{-2}] \cdot \frac{S}{\rho}[MeV\ cm^2 g^{-1}]$$

where S/ϱ_{water} is the stopping power in water.

Dose and Stopping power uncertainties set therefore the lower limit on fluence determination accuracy with this procedure.

5.3.4.1 STOPPING POWER UNCERTAINTY

The stopping power value for the relevant proton energy is retrieved by either SRIM or pSTAR databases. Values listed by the two databases are in agreement, in the energy range of our interest, within 2 %, i.e., the typical accuracy of stopping power determination.

An additional contribution to S/ϱ_{water} uncertainty derives from the energy uncertainty: in the energy range of our interest, an error of ≈ ± 0.2 MeV in the energy evaluation at μDiamond position determines an energy uncertainty at μDiamond sensitive position of about the same entity. This in turn corresponds to a S/ϱ_{water} uncertainty that depends on the LET-energy dependence in the neighbouring interval. We will consider SRIM stopping power values in the following calculations:

- "29 MeV" $\Delta S/\varrho_{water} / \Delta E_{proton} \approx 0.7$ g^{-1} cm^2 ;

  $\Delta S/\varrho_{water} \approx 0.14$ MeV g^{-1} cm^2 for a typical $\Delta E_{proton} = 0.2$ MeV ;

  S/ϱ_{water} (27.0 MeV) = 20.7 MeV g^{-1} cm^2 ;

  $\Delta S/\varrho_{water} / S/\varrho_{water} \approx \pm 1\%$

- "18 MeV" $\Delta S/\varrho_{water} / \Delta E_{proton} \approx 1.8$ g^{-1} cm^2 ;

  $\Delta S/\varrho_{water} \approx .36$ MeV g^{-1} cm^2 for a typical $\Delta E_{proton} = 0.2$ MeV ;

  S/ϱ_{water} (15.8 MeV) = 32.1 MeV g^{-1} cm^2 ;

  $\Delta S/\varrho_{water} / S/\varrho_{water} \approx \pm 1\%$

The total uncertainty in Stopping power evaluation can be conservatively estimated as sum of the two contributions and thus ≈ 3%.

5.3.4.2 DOSE UNCERTAINTY

Dose measurement is performed with a calibrated PTW μDiamond detector acquired with a Keithley 6517B.

Very small dose rate and LET dependence of this detector with proton beams of clinical energies (i.e. > 60 MeV) and dose rates (i.e. up to ≈ 5.5 Gy/min) has been reported in literature (Marsolat et al., 2016).

Comparison of μDiamond and alanine dose measurement with TOP-IMPLART 31 MeV proton beam showed an agreement better than 2% (de Angelis et al., 2019).

For the reported application, we have used the μDiamond detector as dose sensor at even lower energy (18.8 MeV) and moreover significantly higher dose rates, up to 20–22 Gy/min, corresponding to a dose per pulse of nearly 15 mGy/pulse.

While in the 29 MeV and low dose rate set-up periodic calibration and, additionally, comparison with alanine guarantees a dose accuracy of the order of ± 2% or better, in the other set-ups reliability of the detector is not guaranteed. The μDiamond detector has nevertheless been already tested in TOP-IMPLART 27 MeV proton beam and linearity of response was verified varying the extracted proton current and the μDiamond distance from the beam exit, as reported in (Bazzano et al., 2016). Dose rate up to 80 Gy/minute was thus measured, as shown in Figure 55 showing from the original data set.

5.3.5 4.3.4 μDIAMOND AND IONIZATION CHAMBER INTER-CALIBRATION

As happened for each irradiation campaign reported in this thesis, also the R2E irradiation took place a few days after a radiobiology session. This on one hand limited the beam line set-up that could be allowed for the positioning of the electronic components; on the other hand, it provided a numerous sample of calibration data, at least for the 29 MeV – low flux setting, acquired over the course of one week, demonstrating the accelerator stability and reproducibility.

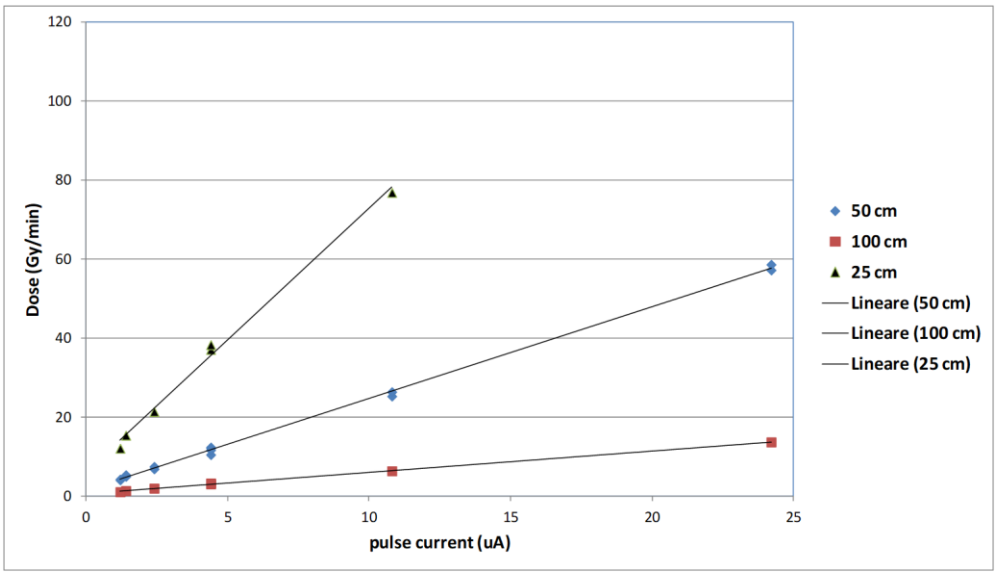

Figure 55 ***Proton dose rate vs the pulse current (uA) – Pulse current was measured with the ACCT. the dose rate with a µDiamond dosimeter*** (Bazzano et al., 2016)

The procedure established with radiobiology experiments exploits inter-calibration of the integral ionization chambers with the µDiamond readings. The calibration procedure focuses on establishing a Monitor Unit (MU) to Gy_{water} correspondence at a reference irradiation position and at a typical dose rate. In this framework, total dose and total fluence are thus determined by the total MU delivered to the Device Under Test (DUT) while assuming the dose rate remains constant. The Monitor Unit to fluence correspondence determined with the calibration procedure is summarized in Table 14. Dose reproducibility is defined as the ratio of the standard deviation (1 sigma) to the average value of repeated dose measurements. Please not that while the 29 MeV – low flux sample is made up of nearly 30 data points, the other 3 settings, employed exclusively for the RHA campaign, are instead made up of less than 10 points each.

Unfortunately, the calibration procedure showed that in the high flux settings ionization chamber 2 readings saturated. Therefore, to avoid repeatedly switching from one ionization chamber to the other as "master" delivery monitor it was decided to use ionization chamber 2 as delivery monitor for the 29 MeV – low flux configuration and ionization chamber 1 for the other three configuration, effectively operating the accelerator as in previous irradiation campaign (including the IMU one). Ionization chamber 1 never saturates because it is instead

affected by high recombination, as detailed in the paper (Ampollini et al., 2020), and is prone to higher fluctuations due to its sensitivity to the smallest variation of the beam spot reproducibility.

However, save for one calibration measurement at very high flux which had to be discarded, careful analysis of the LINAC logs from both the calibration data and the irradiation data allowed to derive a second calibration based on ionization chamber 2 also for the settings "29 MeV – high flux" and "18.8 MeV – low flux". They are reported in italics in Table 15.

Table 14Monitor Unit (MU) to fluence @ DUT calibration for the four settings

Setting	Monitor IC	Fluence/MU (cm^{-2})	Dose reproducibility (1 sigma)
29 MeV - low flux	2	2.74E+03	3%
29 MeV - high flux	1	1.03E+04	6%
18.8 MeV - low flux	1	1.63E+04	9%
18.8 MeV - high flux	1	1.73E+04	9%

Table 15 Monitor Unit (MU) to fluence @ DUT calibration from ionization chamber 2 derived from LINAC log data

Setting	Monitor IC	Fluence/MU (cm^{-2})	Dose reproducibility (1 sigma)
29 MeV – high flux	*2*	*1.90E+03*	*6%*
18.8 MeV - low flux	*2*	*2.56E+03*	*9%*

5.4 CERN ESA MONITOR CALIBRATION CAMPAIGN

CERN R2E group conducted an extensive calibration campaign of ESA monitor between 2011 and 2014 (Noordeh & Garcia Alia, 2014). This activity is still ongoing and data findings for proton and neutron mono-energetic data can be found in (Garcia Alia & Cecchetto, 2020). Figure 56 shows the collection of proton data gathered in this project.

For the purposes of our experiments, we refer to the "1817" data code set reported in CERN Radiation Test report. As can be seen, data for energies lower than 30 MeV relies exclusively on RADEF data. "1036" data set is also relevant as cross section evaluation with and without lid was performed with our beam.

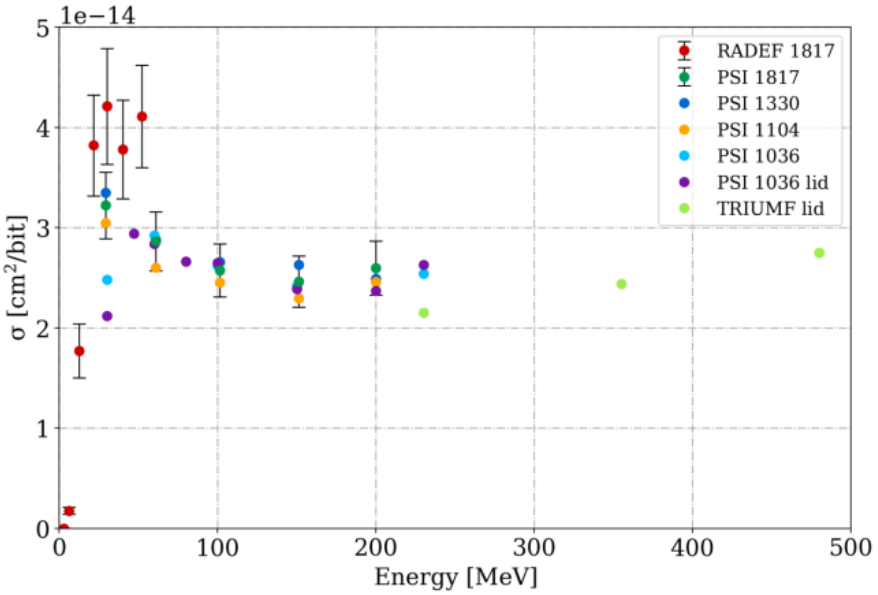

Figure 56 ***Proton tests comparison between date codes and facilities RADEF – PSI –TRIUMF (cross section axis in linear scale). Error bars showed only for RADEF 1817 and PSI 1817 for readability of the graph*** **(Garcia Alia & Cecchetto, 2020)**

The raw data for inter-facility comparison relevant for our test are the following:

Date code	Lid	Facility	Energy [MeV]	σ [cm2/bit]	% [2stdv]
1817	no	PSI (PIF)	29.3	3.22E-14	10
1817	no	RADEF	6.0	1.78E-15	20.31
1817	no	RADEF	12.5	1.77E-14	15.17
1817	no	RADEF	21.5	3.82E-14	13.21
1817	no	RADEF	30	4.21E-14	13.68
1036	no	PSI (PIF)	30	2.48E-14	14
1036	yes	PSI (PIF)	30	2.12E-14	15

Monoenergetic proton energy data were used on multiple ESA monitor detectors to build the experimental Weibull response function:

$$W(E) = 1 - e^{-(\frac{E-E_0}{W})^S}$$

The following fit parameter were calculated:

E_0 = 3.0 MeV

W = 9.1 MeV

S = 2.2

The experimental reference cross section value for protons resulted:

$\sigma_p = 2.66\ 10^{-14}\ cm^2/bit$

Therefore $\sigma_{SEU}(E)$ can be calculated as:

$$\sigma_{SEU}(E) = \sigma_p \cdot W(E)$$

Figure 57 taken from (Garcia Alia & Cecchetto, 2020) shows the experimental data and the fitted Weibull function

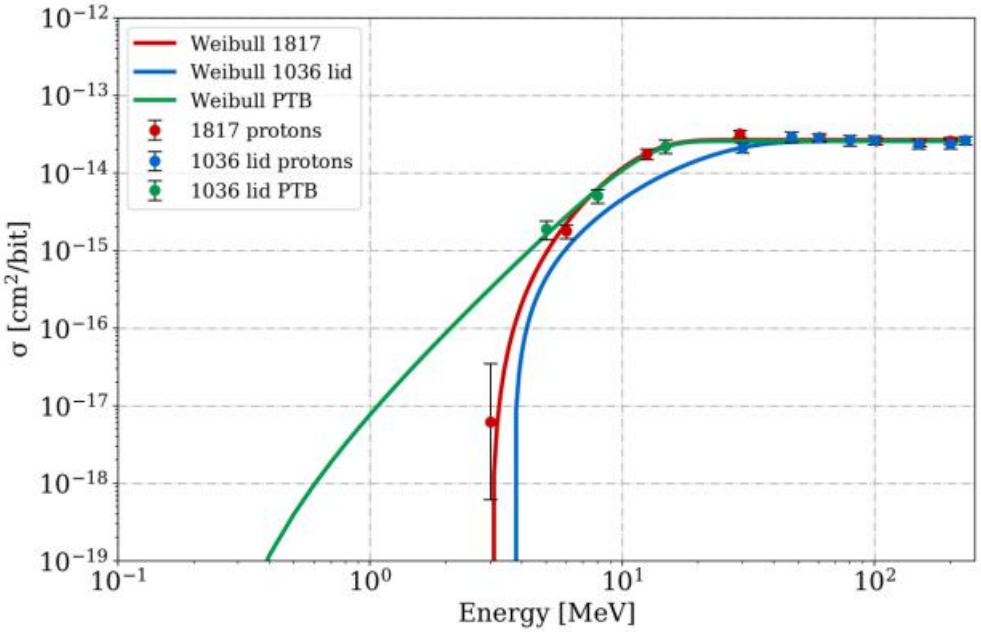

Figure 57 ***PSI proton data for the 1036 (with lid) and 1817 date codes and PTB neutron data 1036 (with lid) and respective Weibull fits in logarithmic scales.*****(Garcia Alia & Cecchetto, 2020)**

The expected cross section values at the TOP-IMPART test energies deduced from the best fit Weibull curve are the following:

$\sigma_{SEU}(29.1\ MeV) = 2.66\ 10^{-14}\ cm^2/bit$

$\sigma_{SEU}(18.8\ MeV) = 2.57\ 10^{-14}\ cm^2/bit$

5.4.1.1 NOTE:

Please note how the 29.1 MeV cross section is significantly lower than the experimental values at 29.3 and 30 MeV (from PSI and RADEF, respectively). This is due to the fact that the Weibull fits aims at best representing the cross section variation over order of magnitudes below a certain threshold energy level, while misrepresenting the experimental evidence of a peak in cross section at an energy of about 30 MeV, possibly due to a combination of direct and indirect ionization from the proton beam on the ESA monitor sensitive part.

The ratio between the cross section at 29.1 MeV with and without lid should be (with an uncertainty of ≈ ± 15%):

$$\sigma_{SEU}(29.1\ MeV)_{with\ LID} / \sigma_{SEU}(29.1\ MeV)_{without\ LID} = 2.11\ 10^{-14} / 2.66\ 10^{-14} = 0.79$$

Experimental ratio measured at PSI with 30 MeV protons is:

$$\sigma_{SEU}(30\ MeV)_{with\ LID} / \sigma_{SEU}(30\ MeV)_{without\ LID} = 2.12\ 10^{-14} / 2.48\ 10^{-14} = 0.85$$

5.5 TOP-IMPLART IRRADIATION SEU CROSS SECTION EXPERIMENTAL DATA

Single Event Upset data for the ESA Monitor irradiations are summarised in Table 16.

Table 16 SEUs for ESA monitor irradiations: total counts and detail of single dies counts

	SEUs	Die0	Die1	Die2	Die3
29 MeV - Low flux					
ESA monitor_dose1	1779	456	444	422	456
ESA monitor_dose2	1211	287	301	320	303
29 MeV - High flux					
ESA monitor_dose1	2602	636	666	647	649
ESA monitor_dose2	2712	664	695	656	695
ESA monitor_dose3	2591	627	651	672	638

29 MeV - High flux with LID					
ESA monitor with LID	2090	558	533	501	498
18.8 MeV - Low flux					
ESA monitor_dose1	1904	496	489	443	475
ESA monitor_dose2	1920	468	471	504	477
ESA monitor_dose3	1906	481	464	506	455
18.8 MeV - High flux with LID					
ESA monitor with LID	21	3	7	4	7
18.8 MeV - High flux					
ESA monitor_dose1	1444	345	365	363	371
ESA monitor_dose2	1408	341	363	387	317
ESA monitor_dose3	1585	386	377	397	424
ESA monitor_dose4	1449	354	365	351	379

5.5.1 4.4.1 TRANSVERSE HOMOGENEITY

The single dies data provide confirmation on the beam transverse homogeneity, which was assessed with SRIM/gafchromic film imaging.

SEUs are a stochastic process, and the associated uncertainty is

- SEUs statistics uncertainty (relative error): $\frac{\sqrt{N}}{N}$

with N number of SEUs

In most cases, counts for the four dies are compatible within one $\sqrt{N}$ statistic uncertainty. Looking at the absolute numbers, typical value of homogeneity, computed as $(SEU_{max} - SEU_{min})/SEU_{average}$, is 5%, which is consistent with the beam characterization described in 5.3.2.

5.5.2 4.4.2 CROSS SECTIONS MEASUREMENTS

Applying the calibration of Table 14 we calculate the actual total fluence delivered to the ESA monitor during the irradiation sessions and the corresponding cross section:

$$XS\ [cm^2/bit] = \frac{SEUs}{\phi\ [cm^{-2}]\ SRAMsize[bit]}$$

with SRAM size = 2^{24} bit

According to ESA recommendations (*ESCC Basic Specification No. 25100 - SINGLE EVENT EFFECTS TEST METHOD AND GUIDELINES*, 2014) cross section uncertainty is given by the quadratic sum of:

- SEUs statistics uncertainty: $\frac{\sqrt{N}}{N}$ with N number of SEUs
- Fluence uncertainty, discussed in the previous paragraphs

In a first iteration we consider the calibration data of Table 14, that is applying ionization chamber 1 coefficients in most cases, which corresponds to the actual dose delivery method used for the irradiation.

5.5.2.1 REPRODUCIBILITY

For each setting, ESA measurement were repeated two or three times with the same nominal fluence (the only exception being the 29 MeV – low flux case where the two measurements correspond to 3 times and 2 times the nominal fluence, respectively.)

We can compare the SEUs reproducibility with the dose reproducibility parameter reported in Table 14. For the 29 MeV cases, reproducibility was ≈ 5%, for the 18.8 MeV cases, it was ≈ 9 %.

SEUs counts reproducibility is better than 3% for the 29 MeV sets; reproducibility is better than 1% for the 18.8 MeV low flux case and it is instead of the order of 5% for the high flux case. In this latter set of data the most notable exception is the third high flux measurement, when a statistically significant different number of upsets where recorded while the flux and fluence remained instead (apparently) very stable. The outcome of this irradiation appears suspicious especially since in all other acquisitions (at both low and high flux) the number of SEUs were extremely repeatable. Further analysis of the LINAC log file offered no clue (such as RFQ or DTL cavity field variation) that would suggest a delivery error (immediately recovered in the following irradiation). Nevertheless, the measurements are all compatible with the typical dose reproducibility evaluated in the Ionization chamber calibration.

5.5.2.2 HIGH AND LOW FLUX CONSISTENCY

The SEU cross section for the ESA Monitor only depends on the proton beam energy and it is independent of the flux. We want to compare cross sections measured at high and low flux irradiation conditions to highlight possible calibration errors.

The measured cross sections are shown in the following Figure 58 and Figure 59 where the error bars combine the SEUs statistical uncertainty and the dose reproducibility (2σ). The stopping power uncertainty and diamond absolute calibration uncertainty are not accounted for at this stage as they influence the absolute value of the cross sections (and, for instance, their comparison with PIF and RADEF values), but not repeatability of the measurements and consistency of low and high flux measurement.

The figures highlight the good reproducibility already discussed, except for the third measurement at high flux for 18.8 MeV.

The relative difference in the low and high flux cross section is 4% for the 29 MeV case when applying calibration data from Table 15, that is a calibration based on readings from ionization chamber 2 for both low and high flux. As discussed, for the 18.8 MeV case we cannot obtain fluence evaluations based on ionization chamber 2 data for both configurations; based on ionization chamber 1 data, the cross section discrepancy for the 18.8 MeV case is 5%.

Despite the differences in stability and sensitivity of the two available ionization chambers, we have obtained similar agreement in the cross sections measurement at the two different flux levels. All measurements are compatible within the evaluated uncertainties.

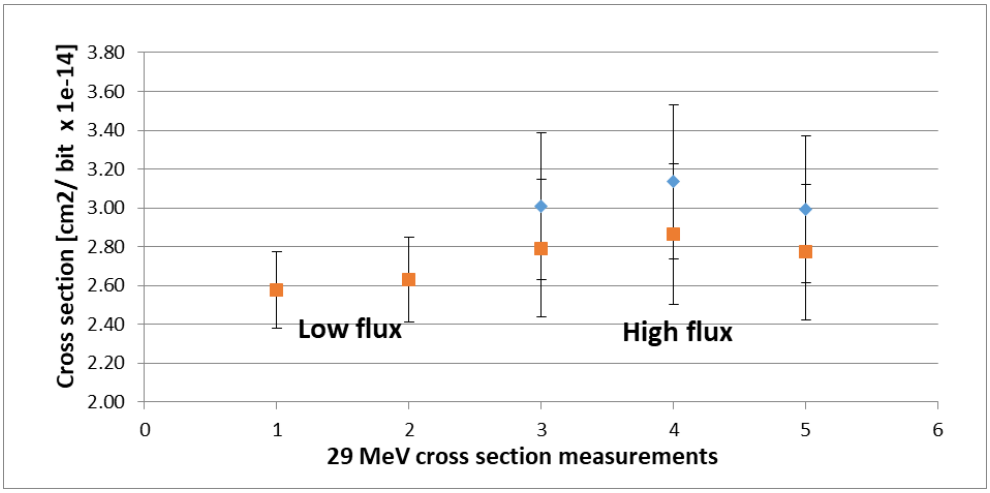

Figure 58 Measured cross sections at 29 MeV evaluated from ionization chamber 1 (blue) and 2 (orange) data (Table 14 and Table 15)

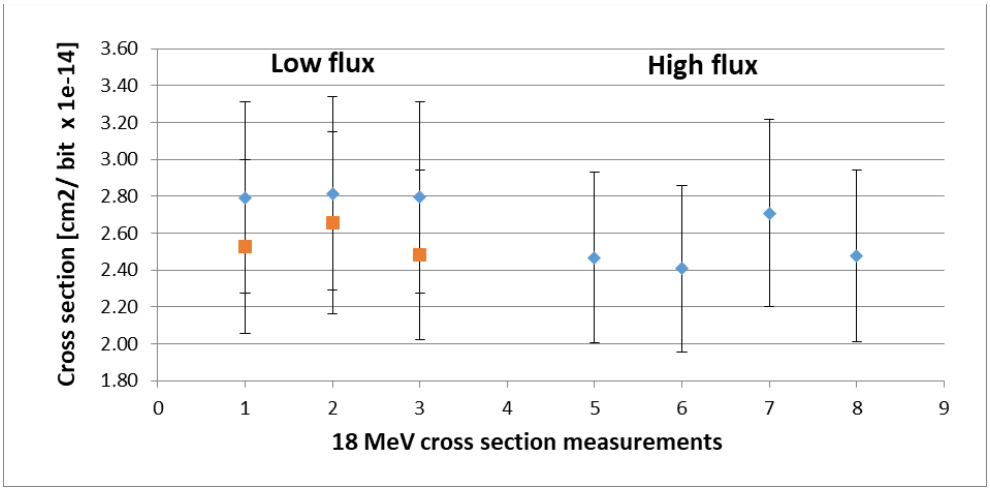

Figure 59 Measured cross sections at 18.8 MeV evaluated from ionization chamber 1 (blue) and 2 (orange) data (Table 14 and Table 15)

5.5.2.3 COMPARISON WITH OTHER FACILITIES CROSS SECTION DATA

Finally, we can compare the actual cross section values with the one measured at PSI and RADEF.

The most significant comparison is between our 29 MeV data and 29.3 MeV (i.e., the same energy within a ± 0.2 MeV error) from PSI. This is the tabulated value closer to our energy measurement setting and the one which has the lower uncertainty from our analysis.

Averaging all data (low and high flux) at 29 MeV and 18 MeV we obtain cross section values and uncertainties detailed in the following Table 17; the total uncertainty is the square sum of the single contributions.

Note: the LET uncertainty of ≈ 3% discussed in paragraph 5.3.4.1 and the μDiamond absolute calibration of 2% are considered uniformly distributed and therefore with a variance of $(3\%)^2/12$ and $(2\%)^2/12$, respectively. The μDiamond accuracy was verified with alanine in the 29 MeV low flux setting only, it could be larger for the other setups. Detail of the cross section evaluation for the 29 MeV low flux data only is also reported as it constitutes our most accurate measurement from the beam delivery point of view.

Figure 60 shows the cross section values obtained at TOP-IMPLART together with the available data in the < 30 MeV range from PSI and RADEF: TOP-IMPLART values closely follow the Weibull fit curve and the cross section at 29.1 MeV is compatible with the PSI value measured at 29.3 MeV.

The ratio of the cross section with and without lid at 29 MeV is found to be:

$$\sigma_{SEU}(29.1\ MeV)_{with\ LID} / \sigma_{SEU}(29.1\ MeV)_{without\ LID} = 2.32\ 10^{-14} / 2.75\ 10^{-14} = 0.85$$

which is the same ratio obtained experimentally at PSI with 30 MeV protons and within 7% of the previously calculated ratio of 0.79.

Table 17 Experimental cross section value for ESA Monitor SEU rate measured at TOP-IMPLART at 29.1 and 18.8 MeV

Energy [MeV]	σ [cm2/bit]	SEUs err % [1stdev]	Fluence reproduc % [1stdev]	LET % [1stdev]	μDiamond % [1stdev]	TOTAL % [2stdv]
29.1 low flux	2.60E-14	1.8	3.0	0.9	0.6	7.3
29.1	2.75E-14	1.0	5.1	0.9	*0.6*	10.6
29.1 with LID	2.32E-14	2.2	6.0	0.9	*0.6*	12.9
18.8	2.53E-14	0.9	9.0	0.9	*0.6*	18.2
18.8 with LID	3.49E-16	21.8	9.0	0.9	*0.6*	47.3

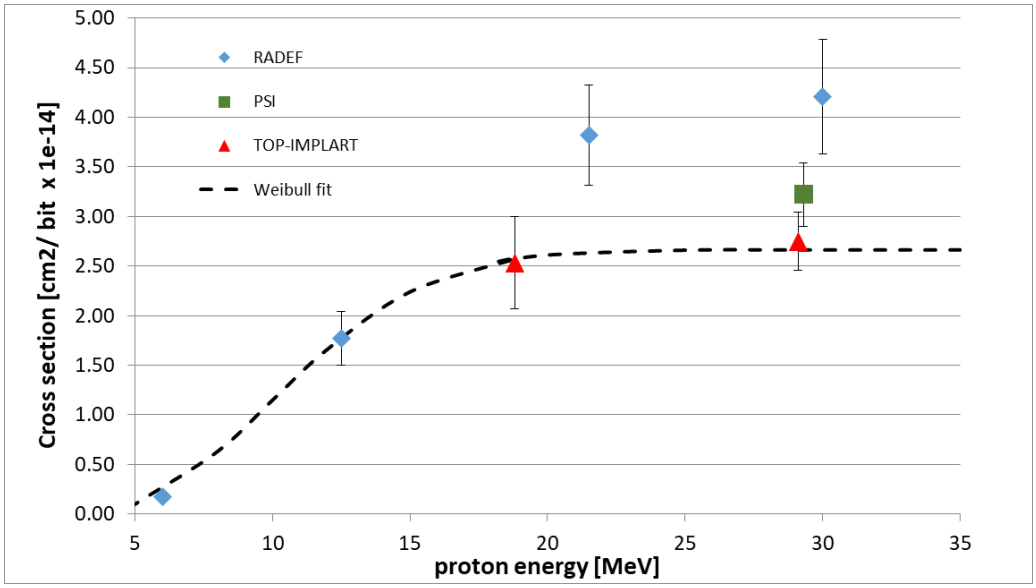

Figure 60 *Cross section comparison summary: TOP-IMPLART, RADEF and PSI data and Weibull fit curve obtained from PSI and RADEF data*

5.6 DISCUSSION AND LESSONS LEARNED

Comparison of cross section data from other accelerators can be summarised as follows:

- The 29 MeV TOP-IMPART cross section is consistent with the one measured at PSI within a typical (for this kind of measurements) 10% uncertainty; both cross sections are compatible with the Weibull curve obtained by the overall data set collected by the R2E group.
- Nevertheless, TOP-IMPLART cross sections appear to be lower than those measured at PSI and RADEF, where other facilities data show a peak in the cross section around 30 MeV proton energy which is not accounted for by the Weibull curve. This could suggest we are slightly overestimating our fluence.
- RADEF is (so far) the only source of cross section data for the ESA monitor for energies below 30 MeV. In the energy interval around 30 – 50 MeV, where RADEF and PSI data are both available, RADEF cross sections are systematically higher than PSI's. While it is beyond the scope of our work to discuss the reliability of other facilities data sets, hopefully measurements performed at other accelerators will clarify the source of these inconsistency and put TOP-IMPLART data in a wider framework.

The overall irradiations set-up and calibration procedure can be improved with the aim to reduce uncertainties or at least better clarify the error sources.

FLUENCE QUALIFICATION WITH THE μDIAMOND DOSIMETER AND ALANINE

While 29 MeV is a well characterized set-up in TOP-IMPLART, 18.8 MeV was a new set-up and suffered from limited number of data point for the dose characterization. This in turn impacted on the dose reproducibility parameter. Additionally, absolute calibration with alanine was determined only in one configuration. To achieve greater precision, i.e. even better that the prescribed 10%, each new setup should be characterized with the full procedure used for the 29 MeV low flux setting:

1. Perform multiple (≈ 30) μDiamond Vs Ionization Chamber measurements, possibly spread out on a significant dose range to verify the linearity of response of the ionization chamber in the neighbourhood of the working point
2. Confirm the dose accuracy, and specifically dose rate independence, with alanine measurements

This procedure is quite cumbersome and time consuming. Additionally, accuracy verification with alanine, which is critical at high LET and high fluxes, relies on equipment not available in the ENEA Particle Accelerator Laboratory.

For this reason, alternative strategies for fluence evaluation and dose rate independence verification should be investigated, specifically for high flux irradiation set-ups which are typically employed for RHA test.

SELECTION OF THE IRRADIATION "MASTER" MONITOR

The use of Ionization Chamber 1, which is prone to larger fluctuations with respect to Ionization Chamber 2, limited the accuracy of beam delivery. On the other hand, saturation on the Ionization Chamber becomes an issue when operating at lower energies (i.e. higher LET) and very high fluxes. To avoid saturation and achieve better reproducibility in dose calibration the 2D ionization chamber could be used instead of the integral chambers. To this end, and to further improve all irradiations, it is considered a priority to integrate the 2D ionization chamber control in the online dose delivery monitoring system.

Chapter 6
EVOLUTION OF THE TOP-IMPLART BEAM MONITORING SYSTEM

In this final chapter we present a series of activities related to the evolution of the TOP-IMPLART beam monitoring system. These include the commissioning of a new beam current monitor and the actions to integrate existing devices into the accelerator control system. The aim of these actions is to overcome the limitations, highlighted in the experimental irradiation activities reported in the previous chapters, of an online monitoring system so far based solely on integral ionization chambers. More specifically we describe the new online control system of the 2D ionization chambers, cross calibration activities of the 2D ionization chamber with the existing beam current monitor and the commissioning of a new, passive RF cavity based current monitor. Advantages of the new monitoring system specifically for RHA testing purposes is discussed.

6.1 UPGRADE IN THE BEAM MONITORING SYSTEM

In spring 2020 experimental activities on the TOP-IMPLART accelerator were suspended to allow installation of accelerating structures SCDTL5 and SCDTL6, bringing the maximum proton energy to 55.5 MeV. In the light of the cumulated experience of almost 2 years of activity with the 35 MeV proton beam, which includes the RHA tests reported in Chapter 3, Chapter 4 and Chapter 5, the LINAC beam monitoring system was upgraded as well.

In Figure 61 is a schematic layout of the accelerator in the 55.5 MeV configuration. With respect to the 35 MeV configuration, which was shown in Figure 7 in Chapter 2, the inter-section drift, that is the drift space between SCDTL4 and SCDTL5 separating the first and the second SCDTL sections, is now fully fleshed and includes two non-interceptive beam current monitors, the ACCT2 and the RF passive cavity, and a vacuum valve between two permanent magnet quadrupoles. At the SCDTL6 exits a new AC current transformer, ACCT3, is installed. The beamline setup is shown in Figure 62 and Figure 63.

Here are the main differences from the previous setup from the beam monitoring point of view:

- A new beam current monitor is available: the RF passive cavity
- The ACCT3, with the Faraday Cup, monitors the extracted current
- The integral ionization chamber 1, at the beam exit, is no longer used
- Integral ionization chamber 2 is the dose delivery monitor
- The 2D ionization chamber has a new dedicated interface for online monitoring

The RF passive cavity is a beam intensity monitor typically employed in electron LINACs. This particular implementation of this kind of beam instrumentation was developed at ENEA Frascati to allow online monitoring of currents < 10 μA, where the ACCT monitors have not sufficient resolution. A detailed account of the development of the passive cavity is published in (Cardelli et al., 2021); in this chapter we report details of its characterization and cross-calibration with beam measurements.

As discussed in Chapter 5, the integral ionization chamber positioned immediately after the vacuum window did not offer sufficient accuracy and was therefore removed. Online monitoring of the extracted current could be performed with signal integration of the ACCT3 trace: preliminary measurements are reported in this chapter.

Finally, the 2D ionization chamber control system was renewed allowing online monitoring of the chamber readings even by non-expert users.

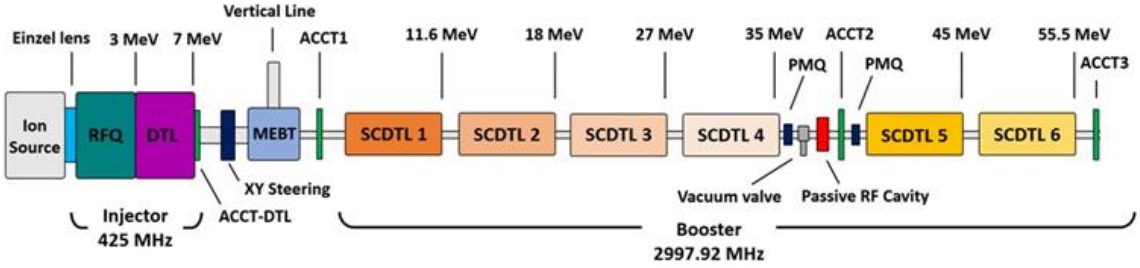

Figure 61 TOP-IMPLART layout up to 55.5 MeV

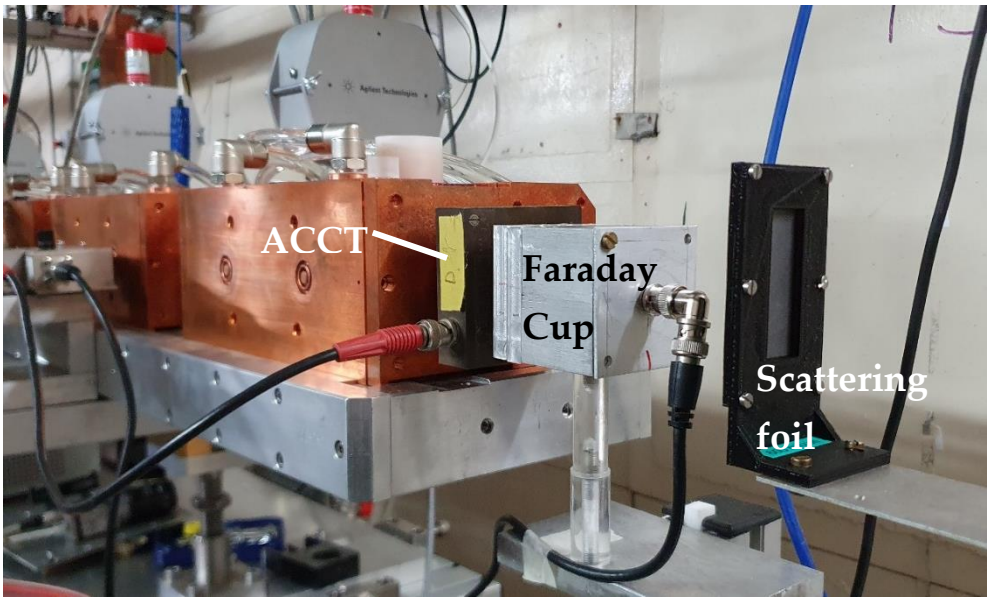

Figure 62 Beam monitors at the exit window of SCDTL6: ACCT3 and Faraday Cup, and lead scattering foil

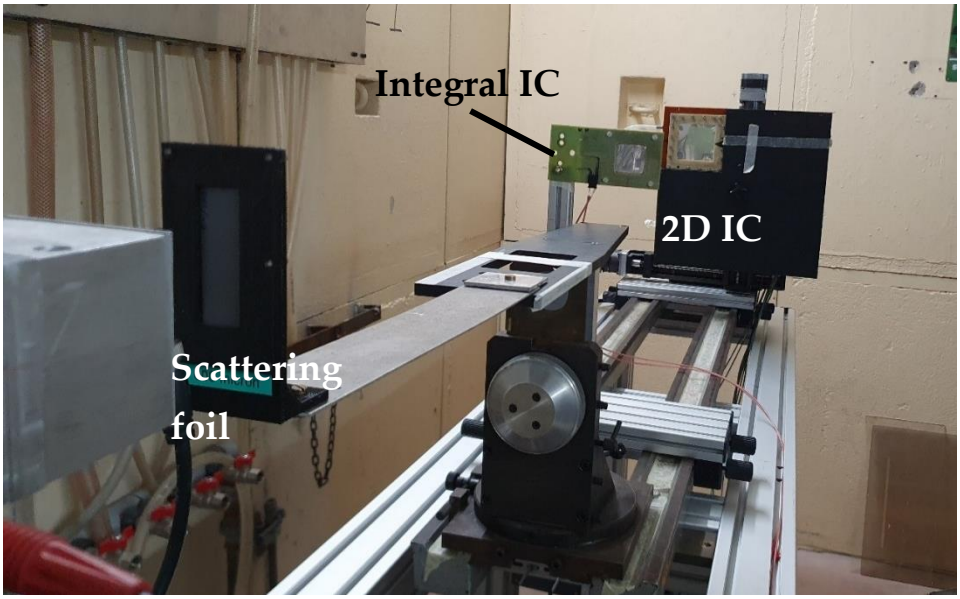

Figure 63 Beam monitors and dosimetric equipment from the beam exit to the irradiation position: lead scattering foil, integral ionization chamber, 2D Ionization chamber

6.2 USE OF THE UPDATED MONITORING SYSTEM IN RHA IRRADIATION

While numerous irradiation experiment on electronic components were proposed and evaluated with the 55 MeV proton beam configuration, none could be performed due to tight scheduling that strictly limited activities beyond the core topics of the TOP-IMPLART project, that is machine commissioning and radiobiology. For this reason, no radiation hardness assurance activity has so far benefited from the updated monitoring system. It should be stressed that the improvements regard the dose/flux monitoring capability and accuracy, as the strategy for energy and homogeneity evaluation remains the same.

In this paragraph we summarize how the updated system should impact future RHA irradiation activities, in the next paragraphs we will describe the upgrade procedure on specific beam monitor and report cross-calibration data collected in various dosimetry sessions.

6.2.1 2D IONIZATION CHAMBER

The main advantage of the new setup is the online availability of the 2D Ionization Chamber. As we have seen in the ESA Monitor irradiation campaign reported in Chapter 5, the monitoring limitations imposed by the limited dynamic range of the two integral ionization chambers, especially at low proton energies and therefore high LET, would probably have been easily overcome by the 2D Ionization Chamber. The comparative behaviour of the two detector was investigated in a dedicated dosimetric campaign with the 35 MeV proton beam and is reported in (Ampollini et al., 2020), demonstrating the significantly superior performances of the 2D ionization chamber, with respect to the two integral ones, in terms of stability and dose rate effect independence, when their response is compared against the μDiamond dosimeter.

Presently irradiations are still driven by the integral ionization chamber and independently monitored by the 2D irradiation chamber, on whose data the estimate of the actual delivered dose is given. This setup is still not optimal for radiobiology (and obviously clinical) activities, as the integral ionization chamber cannot guarantee sufficient accuracy and reproducibility (i.e. ≈ 3%) in the delivery of a specific amount of dose. It is instead adequate for RHA applications where accuracy is required in the determination of the delivered fluence, which can be achieved with the 2D ionization chamber data, while a 10% discrepancy between planned and delivered fluence can be tolerated in most cases.

6.2.2 BEAM CURRENT / CHARGE DETECTORS

While ionization chambers offer, as we have seen, very high charge resolution it is nevertheless desirable to have an independent measurement of the beam pulse-to-pulse current to diagnostic potential dose-rate effects above certain intensity threshold. Investigation of dose-rate effects is a topic of specific concern for RHA activities, as they require, as a rule, higher flux levels than radiotherapy. In particular, Displacement Damage tests may require fluxes in the 10^8 – 10^9 protons cm^{-2} s^{-1}, an order of magnitude over the typical radiotherapy fluxes. Additionally, while monitoring with the 2D IC should always be preferred, one can foresee high flux irradiations set-ups that would require positioning of the DUT before the ionization chamber. It can therefore be useful to assess the uncertainty in fluence determination that can be achieved through extracted current measurements.

Two research activities were dedicated to this topic:

- Development of a passive RF cavity intensity monitor for non-interceptive measurements in the 0.5 – 50 μA range.

  This beam detector was designed to improve the TOP-IMPLART monitoring capabilities for beam current lower than 10 μA, where the ACCT resolution is insufficient. We report the device performances as obtained by characterization of the readout electronic chain response and beam calibration measurements. The detector is an improvement over the ACCTs. Currently only one prototype is in operation in the 55.5 MeV set-up and is positioned in the inter-section drift: it is therefore presently non useful to monitor the current extracted from SCDTL6, but a second device will be installed in the next energy upgrade at the SCDTL8 exit and could further improve our current/charge monitoring capability.

- Charge-per-pulse measurement via digitization and integration of the ACCT3 trace and cross calibration with the 2D Ionization Chamber and μDiamond dosimeter.
  It is a preliminary investigation of the monitoring capabilities of the ACCT performed with a dedicated, temporary set-up. The promising results have stimulated the implementation of an electronic based integration system to be included in the accelerator control system.

6.3 ONLINE CONTROL SYSTEM FOR THE 2D IONIZATION CHAMBER

The 2D ionization chamber developed by the Istituto Superiore di Sanità (Cisbani et al., 2016) within the TOP-IMPLART project has been used in all main radiobiology and dosimetry campaigns carried out at ENEA Frascati. This detector was developed as a prototype of the main beam monitor for the TOP-IMPLART linac: in the clinical practice ionization chambers are the default beam monitoring devices, both in conventional and particle radiotherapy. In medical electron LINACS one or two ionization chambers are embedded into the accelerator head, after the electron to X-rays conversion target, to measure the dose rate: they are integrated into the accelerator control system and operate in closed loop to control the delivered dose. An independent qualification monitor is used at the target position to verify the correct operation of the accelerator. In the current

implementation of the TOP-IMPLART accelerator the two integral ionization chambers are playing the role of the embedded monitor, while the 2D ionization chamber is the independent monitor.

In the protontherapy practice, electronics for dose delivery monitors are designed having in mind the continuous or quasi-continuous proton current produced by cyclotrons and synchrotrons. A significant example is the TERA06 chip (la Rosa et al., 2008), an ASIC developed by INFN and Università di Torino for the beam delivery system of the Centro Nazionale di Adroterapia Oncologica (CNAO), also employed at the Austrian hadrontherapy centre, MedAustron. The TERA06 digitizes the charge readings of the ionization chambers with a current-to-frequency conversion, followed by a digital counter. The maximum frequency of counters is 5 MHz, which is well suited to the prescribed task of monitoring the ripple of a continuous current at 10 kHz. It is instead inadequate to monitor pulsed beam such as those produced by the TOP-IMPLART linac: as already described in Chapter 2, the charge is delivered in ≈ 3 μs long pulses with a 20 – 100 Hz pulse repetition frequency. Only in recent years, newer iterations of the TERA chip have reached counters frequency of over 60 MHz (Fausti et al., 2017) , specifically aiming at monitoring high-flux particle beams.

Being instead developed specifically for a pulsed beam structure, the electronic acquisition architecture of the 2D chamber for the TOP-IMPLART linac follows a different philosophy: the total (integrated) charge collected on a capacity is measured on a ≈ ms timescale, that is a time scale comparable with the accelerator pulse repetition frequency. A 10^4 dynamic range is obtained thanks to a multi gain amplification mechanism described in the following.

The current implementation is based on the IVC102 transimpedance amplifier chip by Texas Instruments (https://www.ti.com/product/IVC102): a single channel integrating circuit is used for the integral chamber, while 96 such channels (i.e. 6 boards with 16 channels each) are currently implemented for the segmented chamber, each channel acquiring one horizontal or vertical strip. The multi gain amplification mechanism is the main peculiar aspect of the readout: as soon as the voltage on the feedback capacitor of the trans-impedance amplifier is larger than a precise voltage reference, an analog switch (driven by a latch) inserts an additional capacitor in parallel to the initial capacitor thus reducing the gain of the trans-impedance amplifier and therefore increasing the dynamic gain of the system. The information of the analog switch status is recorded together with the

total charge. This mechanism can be extended to several gain states. Simultaneous acquisition of the channels is obtained with digital (TTL) timing inputs which control the integration period, hold and reset functions to set the effective transimpedance gain and to reset (discharge) the integrator capacitor. A multiplexer allows the digitalization of the 2D ionization chamber signals with a single ADC during the "hold" phase of the acquisition cycle. The dead time of the detector is limited to the integrator "reset" phase, lasting 10 μs.

Temporization, control and acquisition of the of the ionization chamber was also developed by the Istituto Superiore di Sanità team with electronics hosted in a NIM crate. At the end of 2019, the NIM crate stopped working. As no spare parts were available and some components were obsolete, it was decided to implement a new control system with National Instrument hardware already available for the control of the proton accelerator. This approach, while an unplanned solution, allowed for an easier integration of the 2D ionization chamber in the TOP-IMPLART control system, which is based on LabVIEW, and faster implementation of a user interface so that the beam monitor could be used routinely and not only operated by a small number of expert users.

The control hardware consists of:

- NI-9064 cRIO controller:

FPGA:	Zynq-7020
Processor:	ARM Cortana A9 Dual Core 667 MHz
Operating system:	Linux Real Time

  Only 2 C-modules are needed in a preliminary implementation:

  - NI-9223 analog inputs (AI):

range:	± 10 V
resolution:	16 bit
operating mode:	differential
readout mode:	simultaneous
max sample rate:	1 MS/s/ch

  - NI-9491 digital bidirectional input-outputs (DIO):

Signal levels:	5 V/TTL
Channels:	8
Update rate:	100 ns

Two Analogue Inputs channels are in use: one digitizes the strips voltage and one the gain status of each strip.

The first four Digital channels are used to generate the synchronization signals for the channels acquisition card and the multiplexer; the second set of Digital Output replicates those signals for debugging of the system logic and timing with an oscilloscope.

As described in Appendix A for the case of the BPW34F control, programming of a cRIO embedded system with LabVIEW is structured on three levels, each performing a specific set of tasks:

FPGA (Zynq-7020):	configuration and generation of the digital outputs signal for the IVC102 based acquisition cards; multiplexer and ADC synchronization; ADC acquisition of the voltage signal and gain status.
Real Time (ARM):	acts as arbiter between the User interface and the FPGA for data transfer and configuration setting;
User Interface (PC):	selects different configuration and acquisition mode displays, further elaborates, and saves data; configure the High Voltage generator;

Presently the cRIO based acquisition system is operational in an intermediate development stage: analysis and presentation of the acquired voltage signal is done at the Real Time level, instead of being performed at the FPGA level (analysis) and User interface level (presentation). This configuration is motivated by the limitations and time-consuming issues involved in implementing and debugging an analysis code entirely based on FPGA. Since the LabVIEW Real Time developing environment allows a "debug" mode where a graphical interface is enabled, we took advantage of this possibility to faster develop a simple analysis strategy that could be then transferred to the FPGA and perform graphical representations of data and more elaborate analysis (such as data fitting), which will be then moved at the User Interface level.

The 2D Ionization Chamber measure the proton beam characteristic operating independently from the accelerator. Most notably, its acquisition repetition frequency is asynchronous from the machine pulse repetition frequency and 3 to 4 times higher. Presently the 2D IC acquisition frequency is ≈ 80 Hz, while the LINAC has a 25 Hz PRF. The 2D IC control systems flags each acquisition as either "beam" or "background" based on comparison of the total collected charge with the pedestal reference average and rms value (representative of the "background"); the present threshold condition is 10σ from the pedestal reference. The collected charge is given in arbitrary units as its calculated as the product between each strip capacity (in pF) and the measured voltage in ADC counts.

For each "beam" data the following parameters are calculated:

- Total collected charge
- X and Y barycentre
- X and Y standard deviation

For each irradiation session the following information are immediately presented to the user

- Total collected charge in the irradiation
- Number of beam pulse measured
- Average and RMS collected charge

6.3.1 μDIAMOND AND 2D IONIZATION CHAMBER CALIBRATION

Tests with beam were resumed in late 2020 after the LINAC energy upgrade to 55 MeV and the new online acquisition system has since then been used routinely by ENEA personnel in every dosimetry and radiobiology irradiation session.

Figure 64 represents schematically the set-up of the beam line and the available beam monitoring equipment; after the integral ionization chamber different specific irradiation set-ups have been used, often with complex degraders, such as range modulators. The "target" position is where the μDiamond dosimeter is positioned for set-up qualification. Table 5 lists the budget of material up to the "target".

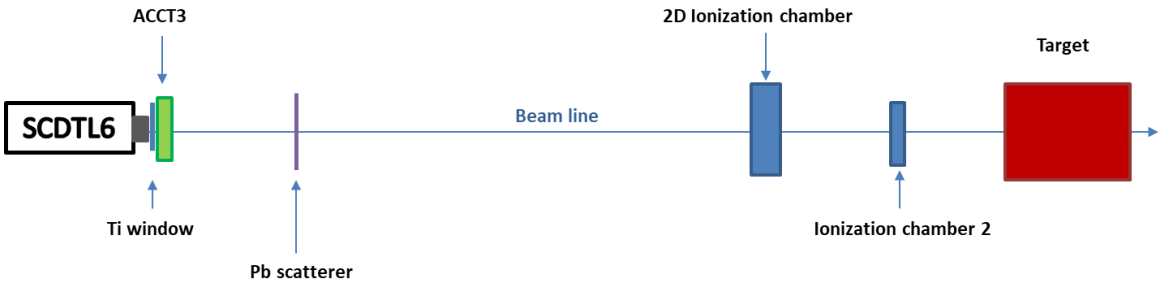

Figure 64 Line set-up in the 55.5 MeV configuration: the "Target" box represents the portion of the beamline which is modified to host different radiobiology experiments

Table 18 List of materials encountered by the proton beam

	Distance from SCDTL6 (mm)	Thickness (mm)	Material
Titanium window	0	0.050	Titanium
Lead scatterer	185	0.210	Lead
2D Ionization chamber	1765	0.170	Water equiv
Integral IC2	1935	---	Mylar & aluminium
Target / µDiamond	2045	-----	-----

For each radiobiology campaign, a cross calibration between the integral Ionization Chamber, which is the IC integrated into the accelerator control system, the 2D ionization chamber and the µDiamond dosimeter was performed.

The integral Ionization Chamber, which drives the irradiation, is responsible for the dose reproducibility, that is the consistency of multiple irradiations where the same dose should be delivered to the target. As described in detail in Chapter 5, for RHA irradiations performed in the 35 MeV setup (such as the IMU and the ESA monitor) when only the integral ionization chamber data were available, the reproducibility was the main uncertainty contributing to the fluence uncertainty.

The 2D Ionization Chamber and the µDiamond measure the dose independently. In Figure 65 and example of the dose measurement of the two device is given: data represent 13 consecutive irradiations at a nominal dose of 3 Gy, measured by the integral ionization chamber as 3000 Monitor Units. From this data set the accelerator & integral ionization chamber dose reproducibility is estimated as ± 7%

(2σ). The 2D ionization chamber readings are linear proportional to the μDiamond data; maximum deviation from linearity is 1.5%.

Linearity of response between the 2D Ionization Chamber and the μDiamond have been verified with multiple irradiation settings in several months of operation (i.e. different "target" arrangements as in Figure 64 nomenclature), with maximum recorded deviation from linearity of 3%. The specific calibration curve depends on the specific irradiation configuration and must be assessed each time. Figure 66 reports multiple examples of cross-calibration data sets between the two monitors.

As we can see, the possibility to acquire information on the delivered dose (and the fluence) with the 2D ionization chambers for all irradiations, including future RHA activities, dramatically decrease the uncertainty with respect to a monitoring system relying exclusively on the dose reproducibility offered by the integral ionization chamber.

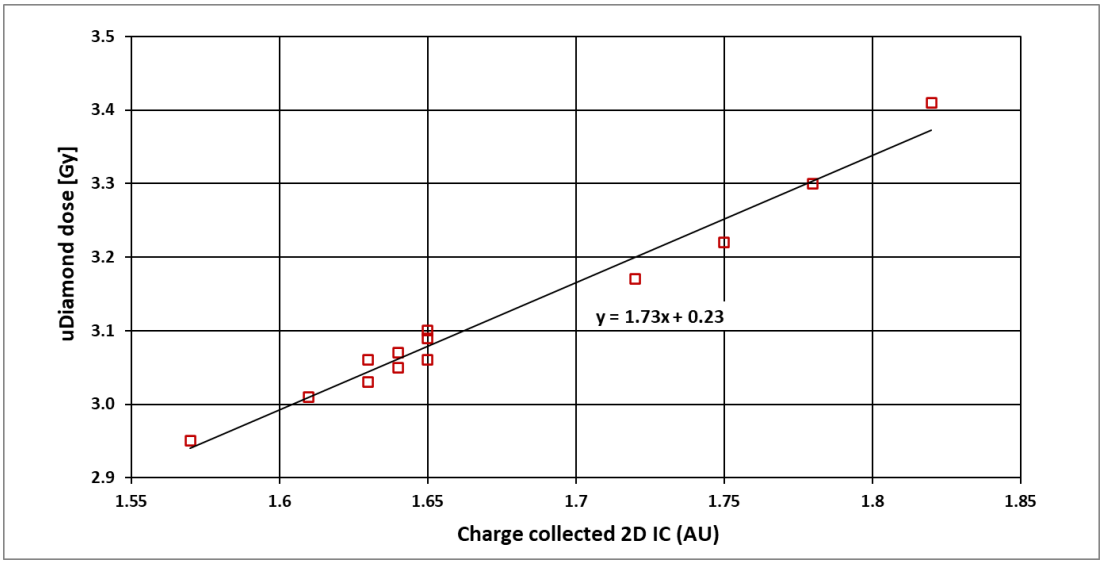

Figure 65 μDiamond 2D IC calibration data for 13 repeated irradiations of a nominal dose of 3 Gy. Dose reproducibility is ± 7 % (2sigma); μDiamond and 2D IC data maximum deviation from linearity is 1.5 %

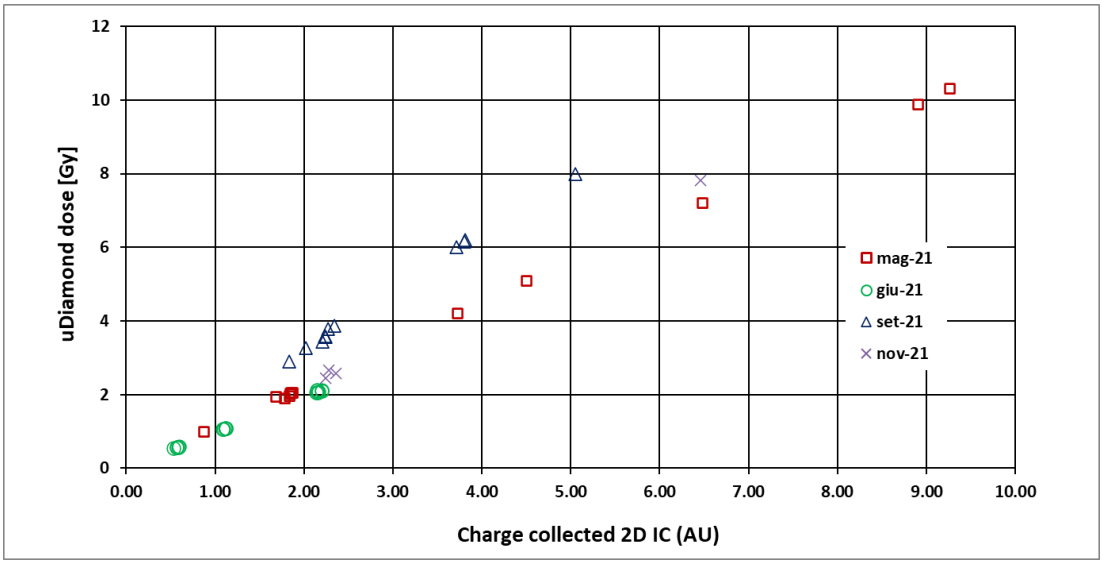

Figure 66 Examples of μDiamond 2D IC calibration data collected over multiple irradiation sessions and different set-up configurations

6.4 BEAM CHARACTERIZATION AND CALIBRATION OF THE RF PASSIVE CAVITY

As already mentioned, both commercially available and in-house manufactured AC Current Transformers employed both in the injector and in the booster section of the TOP-IMPLART accelerator to monitor the beam transmission and the accelerated current do not offer sufficient resolution in the real-time monitoring of very low current beams (< 10 μA) which are relevant for lower intensity applications, namely clinical treatment.

The RF passive cavity was designed to allow non interceptive measurements in the 0.5 – 50 μA range, and a longitudinal length of 12 mm as allowed by the beam optics constraint in the inter-section drift.

The physical principle underlying the passive cavity is the following: the proton beam passing along the axis through the gap of a cavity, resonating at the correct frequency, excites an electromagnetic field in it. The amplitude of this field is directly bound to the beam current intensity. Therefore, using a magnetic pick-up on the outer wall of the cavity coupled to the field, it is possible to obtain a signal proportional to the beam current.

Detail on the electromagnetic design of the passive RF cavity is beyond the scope of this work: it is reported in (Cardelli et al., 2021). Here we instead report the device performances as obtained by characterization of the readout electronic chain response and beam calibration measurements.

Figure 67 shows the passive cavity in its final position in the inter-module space between SCDTL-4 and SCDTL-5 together with a vacuum valve and an ACCT placed between two PMQs.

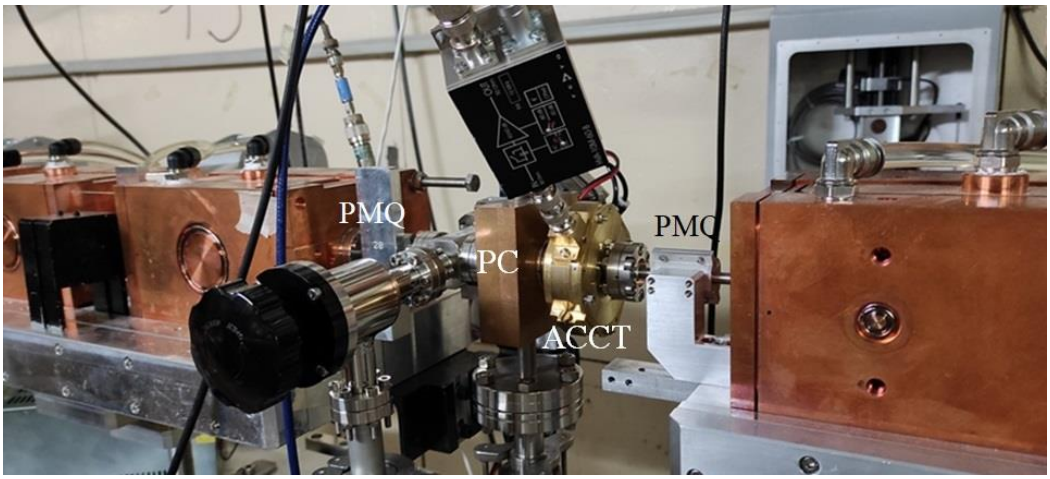

Figure 67 Passive cavity (PC) placed in the drift space between SCDTL-4 and SCDTL-5.

6.4.1 PASSIVE CAVITY OUTPUT SIGNAL AND READOUT ELECTRONIC CHARACTERISTICS

A simplified analytical model and Particle In Cell simulations with CST Studio Suite were used to characterize the passive cavity output power as a function of the proton beam average current: the two quantities follow a logarithmic law, as shown in Figure 68.

A simple yet effective detection system was implemented to cover the 40 dB dynamic range.

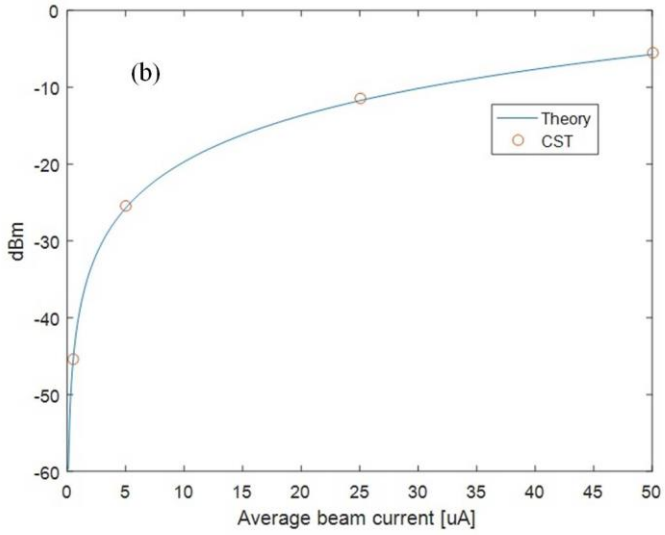

Figure 68 RF output power variation with respect to the average beam current as computed with the PIC module simulation (CST) and the analytical model

The current signal is extracted from the envelope of the cavity output using the ZX47-60+ power detector manufactured by Minicircuits. The detector consists of a logarithmic envelope-detecting amplifier characterized by a wide dynamic range, extending from -60 dBm to -5 dBm at 3 GHz, with a nominal transducer gain of -25 mV/dB and a log-conformance of ± 1 dB within that range. The video output of the power detector consists of an analog voltage in the 2.10V – 0.5V range varying linearly with the input power expressed in dB. It also outputs an analog voltage signal proportional to its temperature, to compensate temperature-dependent variation (2 mV/°C) on the video output.

The intended use of ZX47-60+ detector is in transmit power control loops in RF systems, to stabilize the output of RF power amplifiers, and is not designed to provide an accurate representation of the envelope of the input signal during large transients. This is particularly evident in the asymmetry between the rise and fall times, that are 400 ns and 10 ns respectively. As a consequence, the current signal is distorted and presents a long tail, longer than the actual decay of the field in the cavity detector.

The available documentation also does not report the video bandwidth. A reasonable estimation of it can be deduced from the fall time (tf) information:

$$BW = 0.35 / tf = 0.35/(10*10\text{-}9\ ) = 35\ MHz$$

The ZX47-60+ power detector is placed next to the cavity in a shielded aluminium box connected to it with a 1 m long coaxial cable in the accelerator bunker. Signal acquisition and processing is performed in the control room. The communication between the two environments is guaranteed by 50 Ohm coaxial cable with matched terminations.

ZX47 video and temperature outputs have minimum impedance requirements of 100 Ohm and 2000 Ohm respectively and cannot be connected directly to 50 Ohm systems. To overcome this limitation, front-end electronics has been developed, consisting of a gain stage followed by a high current buffer, as shown in Figure 69. The front-end electronics is hosted in the detector box.

The gain stage sets the load impedance for the detector ports (1 kOhm for the video output and 10 kOhm for the temperature output), provides a gain of 2 V/V and sets the system bandwidth to 12 MHz. The high current buffer sets the output impedance to 50 Ohms and is able to source or sink up to 250 mA. Front-end electronics provides an overall gain of 1 V/V on a load impedance of 50 Ohm and sets the system bandwidth to 12 MHz. This value, lower than the one of the detector alone, is sufficient to correctly detect the power level of the flat-top of the TOP-IMPLART current pulses, that have widths ranging from 1us to 5us.

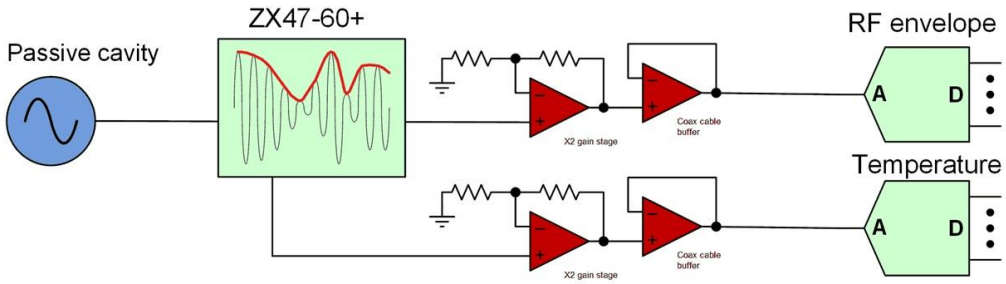

Figure 69 Detection system used in the measurements with the passive cavity in vacuum.

The full acquisition chain (i.e. power detector, amplifier, cable and scope) has been characterized using two different precision RF source, both in CW and Pulsed mode, to obtain an experimental Input power (Pin) Vs Output Voltage (Vout)

curve in the range -46 dBm; - 7 dBm. The output voltage is calculated as the difference between the flat-top and the pedestal and is a positive quantity. The uncertainties taken into account in this characterization are the input power reproducibility, estimated to be $\Delta P = \pm 0.2$ dBm, and the oscilloscope binning resolution and DC gain accuracy ($\Delta V = \pm 10$ mV and $\Delta V = \pm 38$ mV, respectively). The best fit of the experimental data is:

$$\text{Vout @ 1 M}\Omega = \text{Mcal} * \text{Pin} + \text{Qcal} \qquad 8$$

with Mcal = 49.3 ± 0.1 mV/dBm and Qcal = 3221 ± 3 mV ; Vout is expressed in mV and Pin is expressed in dBm.

The system was then tested at different current levels to perform a cross-calibration of the passive RF cavity with the already installed diagnostic devices: the ACCT and Faraday Cup. The output current has been changed varying the voltage on the Einzel lens placed in the injector. Figure 70 shows the output signal from the passive cavity detection system for two different current values, compared to the signal of Faraday cup and current transformer at high intensity, and only with the signal of the Faraday cup at low intensity (where the current transformer is outside its working range). In the cavity traces a non-zero signal less than 100 mV of amplitude is visible about 2 μs before the actual beam signal, at the RF power system switching on. This effect, which limited the detector operating range, has been then removed by putting the amplifier circuit in the shielded aluminium box.

Figure 71 reports the beam current intensity as retrieved by both the detection systems described above versus the measured values of the output signal of the cavity in Volts. They have been acquired by the oscilloscope, simultaneously recording the average value on the plateau for the traces of faraday cup, ACCT and passive cavity. The data follow an exponential law, as expected, since the ZX47-60+ power meter output voltage is linear with the logarithm of the input power according with equation 8. The errors on the measured data consider the uncertainties for the different instrumentations depending on the combined binning resolution and DC gain accuracy of the scope used for the data acquisition. The calibration uncertainties have been also taken into account, but their contribution is negligible with respect to the voltage uncertainty.

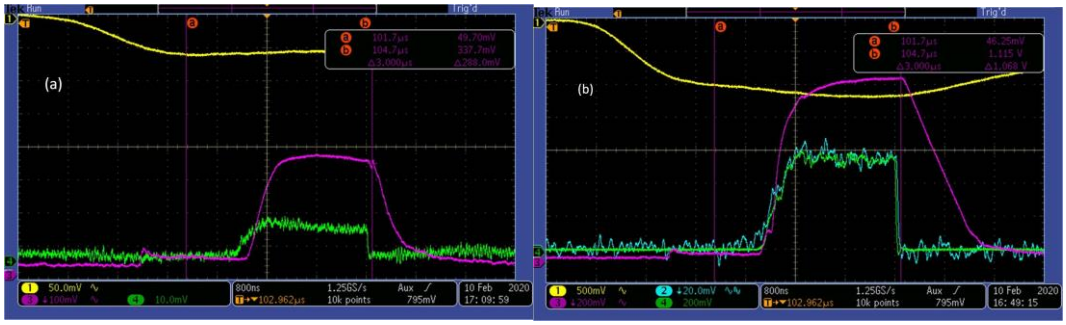

Figure 70 Beam current profile measurement at the end of the fourth SCDTL structure read with an oscilloscope for two different values of the current injected into SCDTL structures: (a) AC transformer at SCDTL-1 input (yellow, Scale = 50 μA/div), Faraday cup (green, Scale = 0.5 μA/div), passive cavity (purple). (b) AC transformer at SCDTL-1 input (yellow, Scale = 500 μA/div), Faraday cup (green, Scale = 10 μA/div), Current Transformer (blue, Scale = 10 μA/div), passive cavity (purple).

The best fit of the measured data gives the following empirical calibration curve of the beam current versus the measured voltage shown in Figure 71 as solid line.

$$I\ [\mu A] = 0.086 * \exp(2.33 * V_{meas}) \qquad 9$$

with Vmeas expressed in Volt.

The impact of the measured voltage uncertainty on the beam current evaluated with this calibration model is given by the relation:

$$\delta I / I = 2.33 * \delta V \qquad 10$$

with δV expressed in Volt.

To the typical oscilloscope acquisition setting δV ≈ 40 mV corresponds a beam current relative uncertainty of ± 9%, which is adequate to monitor the beam intensity stability pulse to pulse, and could be further improved with a dedicated, higher accuracy digitization system.

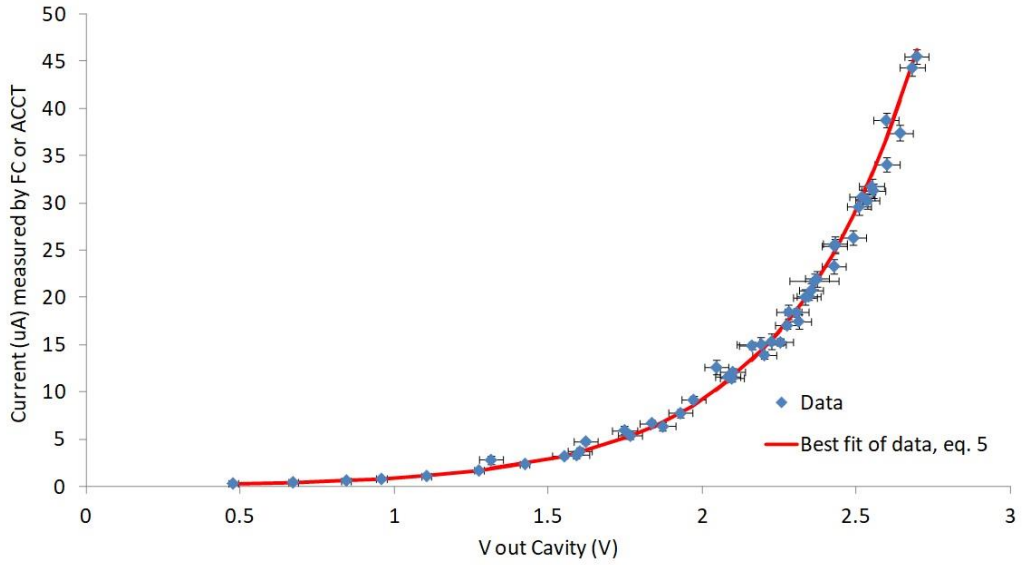

Figure 71: Calibration curve (equation 9) and beam pulse Vs detector output voltage data.

Presently there is no temperature control on the passive cavity, in contrast to the SCDTL accelerating structures which are provided with thermo-regulator system and operated within a temperature stability of +/- 0.02 °C . However, while the SCDTL structures have Q0 values up to ≈ 11000, the passive cavity, thanks to its lower Q0 (≈ 4000), is less prone to thermal detuning. It can be calculated that a 50 kHz detuning, induced by a 1 °C temperature variation, only results in a power variation of about 0.5 %, which is negligible compared to the other uncertainties we accounted for in our experimental setup. Nevertheless, the resonant frequency of the passive cavity was checked before and after all measurements reported in this paper, to ensure no significant temperature variation had occurred.

To ensure long term stability and reliability of the device, even at higher repetition frequency (50-100 Hz), we plan to acquire the temperature readout of the power detector and equip the passive cavity with a cooling system.

6.5 ONLINE CHARGE MONITORING WITH AC CURRENT TRANSFORMER

It has been stated before that the AC Current Transformer employed in the TOP-IMPLART 3 GHz section struggle with measurements for pulse currents below 10 μA.

As an example, Figure 72 shows ACCT2 acquisitions in the 35 MeV setup at two peak current levels, 5 and 2 μA. While averaging of the trace over many pulses reduces the stochastic error allowing measurement of the average current over the time interval, the pulse-to-pulse information on the proton current is lost. In normal machine operation the ACCTs traces are displayed on the oscilloscope to provide a reference to the operators, but no data is included in the accelerator control system or stored.

To perform intensity modulated proton therapy, pulse-to-pulse current variation and measurement over at least a factor 10 in the 0.1 – 10 μA range is required. For RHA irradiations, fast intensity variations are not required, instead we would like to guarantee the stability of the beam extraction over the whole irradiation time.

Since the charge-per-pulse, rather than the peak current level, determines the flux to the target position we wanted to investigate the possibility to extract charge information from the noisy ACCT trace by digital or electronic integration. The information we want to obtain are analogue to those recorded with the 2D ionization chamber in one irradiation session:

- Total collected charge in the irradiation
- Number of beam pulse measured
- Average and RMS collected charge

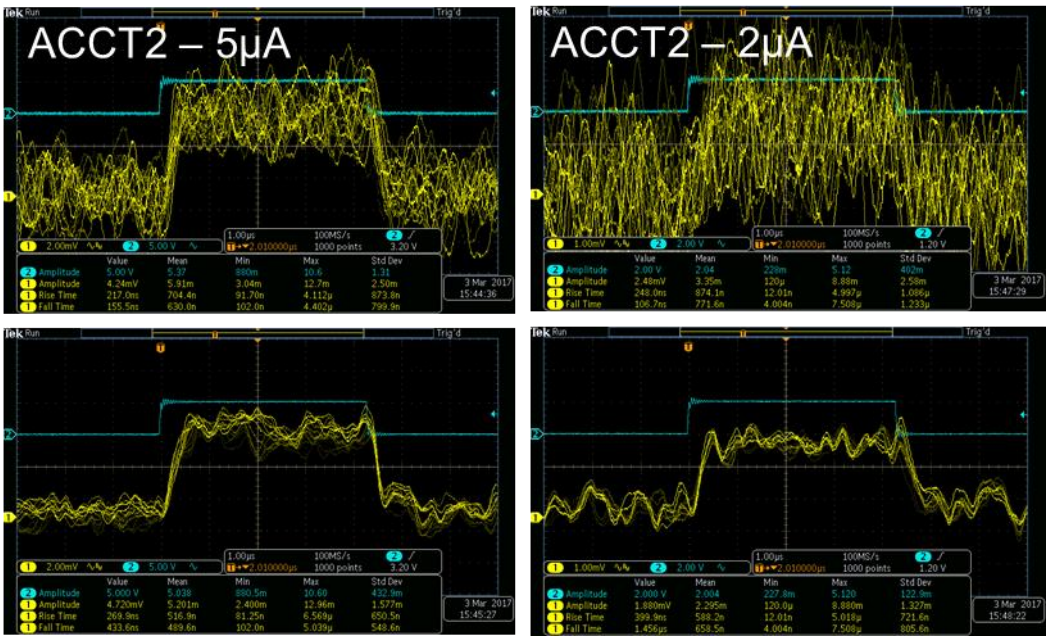

Figure 72 ACCT2 acquisitions with the 35 MeV setup: pulse to pulse trace at 5 and 2 μA peak current (top), averaged trace at 5 and 2 μA peak current (bottom)

6.5.1 ACCT3 ACQUISITION WITH PICOSCOPE

The preliminary investigation was carried out employing a PicoScope 3405D, a PC based oscilloscope that can record multiple captures (each capture corresponds to one pulse) in its memory and transfer them on the PC at the end of the acquisition. This technique was already employed in the past to investigate the stability of RF signals the 35 MeV section of the accelerator (Nenzi et al., 2018). In this analysis each capture consists of 5.000 samples, with a sample time of 2 ns. Acquisition is synchronous with the accelerator Pulse Repetition Frequency.

Digital integration of the traces is performed offline with a LabVIEW analysis routine.

For each trace, the voltage signal is converted to current (in μA) with the ACCT3 conversion factor; 2500 samples, corresponding to a 5 μS interval where the ≈ 3 μS pulse signal is comprised, are summed and the average charge (in pC) is computed. The extremely simple analysis mimics a straightforward circuit-based integration, which is being implemented. Due to the limited bandwidth of the

ACCT electronic, the charge value computed with this procedure is expected to be proportional, rather than equal, to the number of protons per pulse.

In "no beam" pulses the ACCT trace average value is zero, that is there is no offset in the device to be subtracted. A threshold on the charge value is then used to separate pulses and tag them as "beam" or "background", a procedure similar to the one used in the 2D ionization chamber.

6.5.2 COMPARISON OF THE ACCT3 BASED FLUX MONITORING WITH THE 2D IONIZATION CHAMBER

In this preliminary investigation we cannot unfortunately assess absolute values of charge and flux. A relative comparison is instead performed between the ACCT and the 2D ionization chamber at different current levels. Two settings were used: the nominal one, described in Figure 64, with the 210 μm Lead scatterer and the same setting without the scatterer. The extracted beam energy is 55.5 MeV. In the two settings, at a same extracted current correspond a very different fraction of beam transported at the 2D IC position: the beam parameter computed with SRIM/TRIM are reported in Table 19. We considered a 4 x 4 cm^2 the active area of the ionization chamber, corresponding to the central portion equipped with readout electronics.

Table 19 Beam parameters at the 2D IC position computed with SRIM/TRIM

Scatterer	Beam size at the 2D IC (sigma) [mm]	Fraction of protons at the 2D IC active area [-]	Average LET at the 2D IC active area [MeV g^{-1} cm^{-2}]
210 μm Lead	27.8	0.293	12.165
none	8.7	0.993	11.934

6.5.2.1 FLUX STABILITY

We define the flux stability parameter as the ratio of the standard deviation and the average value of the pulse-to-pulse charge over an irradiation session. Measurement of this parameter with the ACCT3 and the 2D ionization chamber was carried out in ≈ 2000 pulses long irradiations.

In Figure 73 the computed flux stability parameter is reported for the two irradiations setting (with and without the scatterer) together. The instantaneous current value here reported is obtained from the computed integral current value and considering a pulse FWHM of 2.4 μA. As we can see, the discrepancy between the flux stability estimate from the two detectors increases at lower instantaneous current level. This suggests that integration alone is not sufficient to suppress the noise contribution of the ACCT trace, leading to a pejorative estimate of the machine stability.

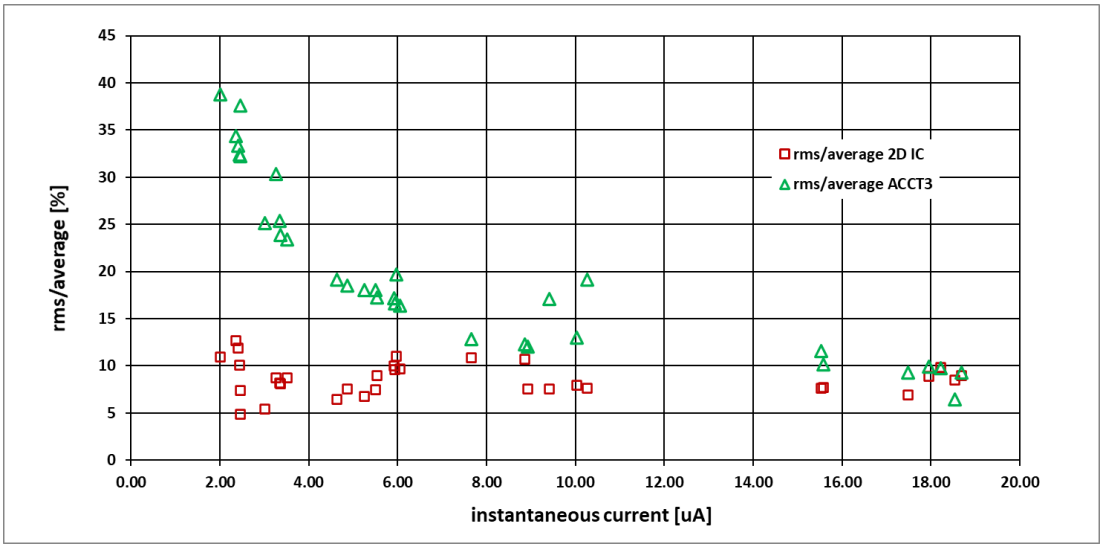

Figure 73 Flux stability evaluation at different extraction current computed with two different instrumentations: ACCT and 2D IC

A better representation of the accelerator extracted charge stability should be achieved with a beam monitor with adequate sensitivity to the lower currents, such as the RF passive cavity. Since this detector is currently implemented in the inter-section drift only, its present readings do not properly represent the extracted beam stability, which is additionally affected by the beam transmission through sections SCDTL5 and SCDTL6. However, in Figure 74 flux stability measured with the RF passive cavity is added to Figure 73 graph, showing the promising behaviour of the RF passive cavity as flux stability monitor on all the investigated current range.

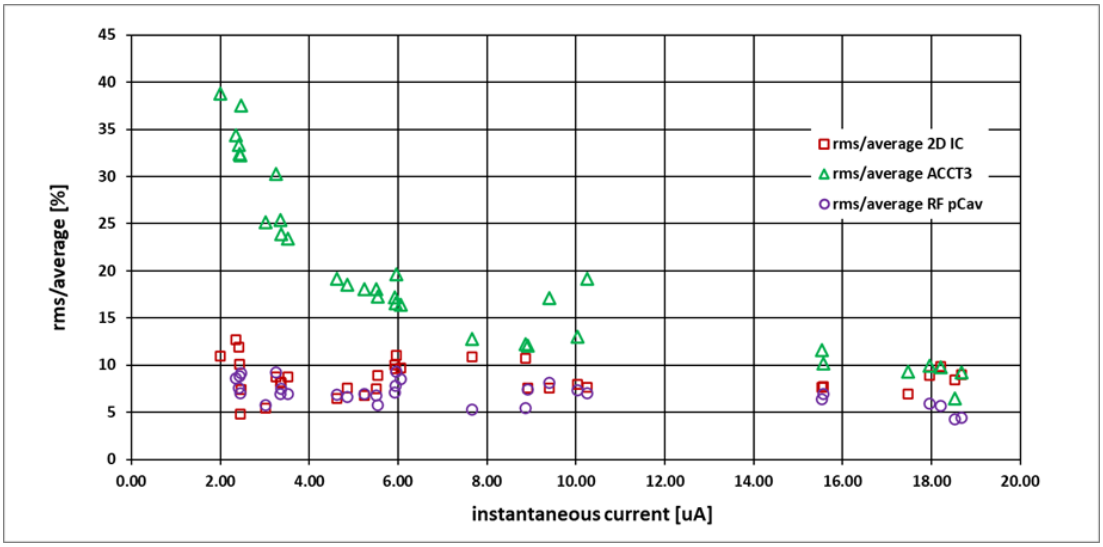

Figure 74 Flux stability evaluation at different extraction current computed with three different instrumentations: ACCT, 2D IC and RF passive cavity

6.5.2.2 EXTRACTED CHARGE - FLUENCE LINEARITY

A comparison between the total extracted charge and the collected charge at the 2D IC is here presented. Despite the resolution limits of the ACCT monitor at lower currents, demonstrated in the previous paragraph, it could still provide meaningful information on the fluence, or dose, delivered to a target on the beam line.

To compare data of the two settings (with and without the scatterer) together, we convert the total extracted charge measured by the ACCT3 to the expected fluence at the 2D IC active area, with information based on SRIM/TIRM calculation reported in Table 19. Higher fluence are obtained with higher instantaneous current levels. The elaborated data are shown in Figure 75: in the usual beam line configuration, i.e. with the lead scatterer, we observe a linearity between computed fluence and 2D IC collected charge; in the "high flux" configuration, i.e. without the scatterer, saturation in the 2D IC response is observed at the highest fluxes.

In the linear region, deviation from linearity of the collected data is on average 4%: this would be the typical instrument uncertainty that should be considered in a scenario where fluence monitoring at the DUT positions should be based on the

ACCT online data. A proper calibration strategy, to obtain absolute dose or fluence values at the DUT position even in high-flux configurations shall be investigated in future works. This should include μDiamond and alanine dose comparison, as was already done within the TOP-IMPLART project, and absolute fluence measurement with activation analysis. The latter technique, which is a standard in many facilities, relies on gamma spectroscopy with high-resolution germanium detector, which is still not available within the TOP-IMPLART laboratory.

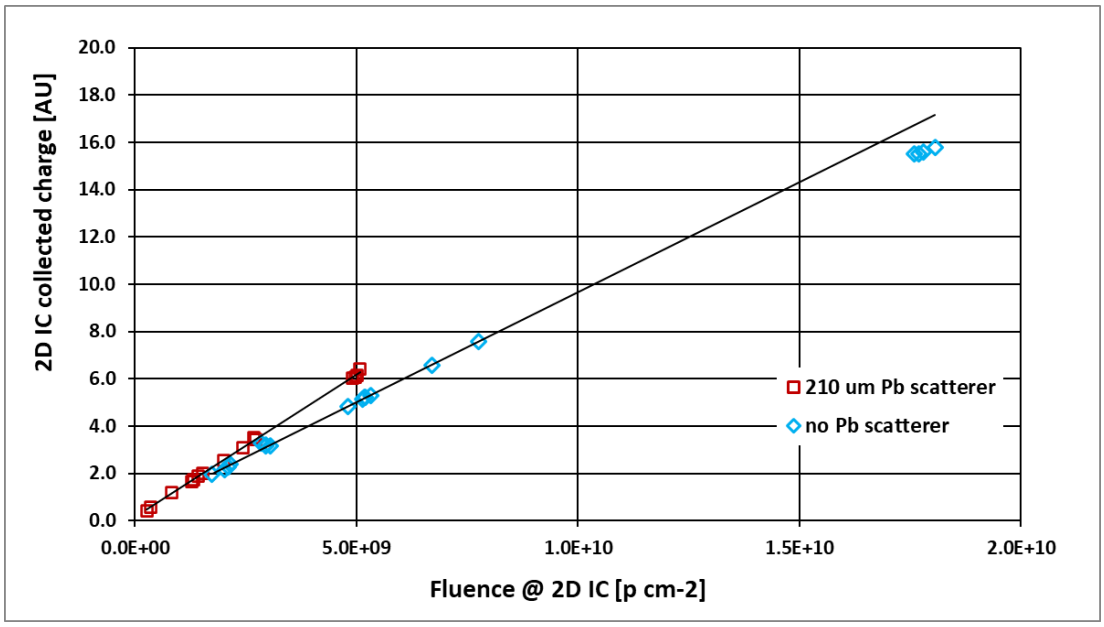

Figure 75 Comparison between computed fluence at the 2D IC position and charge collected by the 2D IC

6.5.2.3 EXTRACTED CHARGE – DOSE REPRODUCIBILITY LINEARITY

The same acquisition set-up was used contemporary to a dosimetry session for radiobiology studies. The beam line setup is the one described in Figure 64, the μDiamond dosimeter was positioned in the "target" area. Dose reproducibility comparison already performed with the 2D ionization chamber and the μDiamond dosimeter (see Figure 65 as an example), is now including charge information from ACCT3 trace integration. Result is shown in Figure 76: as before, data represent 13 consecutive irradiations at a nominal dose of 3 Gy, measured by the integral ionization chamber as 3000 Monitor Units. From this data set the accelerator & integral ionization chamber dose reproducibility is estimated as ± 6% (2σ). The ACCT3 readings, reported as total number of extracted protons, are linear proportional to the dose measured by μDiamond. The maximum deviation from

linearity is 2.3%. Agreement within the two detectors, while significantly worse than the one achieved with the 2D ionization chamber, still constitute and improvement with respect to the previous monitoring system relying exclusively on the dose reproducibility offered by the integral ionization chamber.

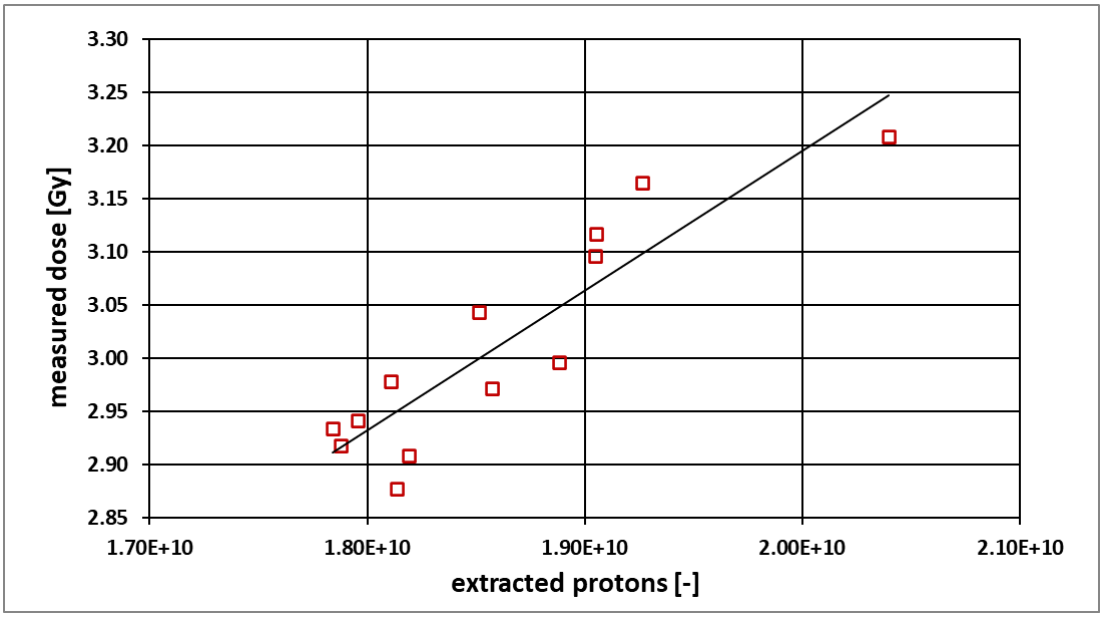

Figure 76 μDiamond and ACCT3 calibration data for 13 repeated irradiations of a nominal dose of 3 Gy. Dose reproducibility is ±6 % (2sigma); μDiamond and ACCT3 data maximum deviation from linearity is 2.3

SUMMARY AND CONCLUSIONS

The aim of this thesis was to investigate the possibility to apply a full-LINAC proton accelerator designed for particle therapy as a radiation source for Radiation Hardness Assurance test compliant with the European Space Components Coordination prescriptions.

In a worldwide scenario of growing need of beam-time for radiation qualification of space components, proton therapy accelerators are playing a significant role in providing proton beams of energies and intensities fulfilling the typical requirements for Displacement Damage and Single Event Effects tests. Each facility, though, develops unique solutions to satisfy the clinical requirements for beam monitoring, and so will be the procedures to perform beam qualification and monitoring for RHA irradiation in that facility. As proton LINACs aim at providing an alternative to cyclotrons and synchrotrons in the cancer therapy domain, they could also constitute a meaningful alternative for radiation testing once specific beam monitoring system, tailored to the pulsed nature of the proton beam, are validated.

The research activity was carried out at the TOP-IMPLART accelerator, presently in the commissioning stage at ENEA Frascati research centre. Even if the accelerator is still not completed, its intrinsic modularity allows extraction of the proton beam in temporary set-ups and irradiation of samples in air. We tested the beam delivery competences developed for pre-clinical studies in three irradiation campaigns when the accelerator was in the 35 MeV configuration, which constitutes the fundamental unit of the TOP-IMPLART linac. The three selected devices were representative of different radiation hardness tests that can be performed with protons: displacement damage effects, single event effects and system level qualification where cumulative and stochastic effects are probed simultaneously. The first two are considered reference devices for Displacement damage and SEE and have a known radiation response either from literature or from previous irradiation data with proton beams produced by synchrotrons and cyclotrons. A commercial 6-axis integrated MEMS inertial navigation system

(accelerometer, gyroscope) not intended for operation in harsh environment, was instead selected to evaluate a simple system level procedure that could be applied in typical University CubeSat projects.

The IMU characterization, performed in a single irradiation session, exploited the relatively high LET of the low energy protons to simultaneously probe combined TID and DD effects up to a 50 krad(Si) and, additionally, to quantify the device sensitivity to single event effects at a system level by measuring the Single Event Functional Interrupt cross section at low proton energy. While still limited in its scope, as, for instance, characterization at 3 or 4 more proton energies are needed to properly define a Weibull SEFI cross section curve, this procedure allowed a qualitative and quantitative description of a complex component behaviour and a minimum set of possible failure modes to be characterized, thus constituting a cost and time effective alternative over the frequent "no test" approach.

The experimental activities allowed an assessment of the maturity level of the beam characterization and delivery capabilities already in place and specifically adapted for the purposes of electronic components qualification. The agreement found with literature data for both the p-i-n diode dosimeter and the ESA monitor confirm the acceptable accuracy in beam parameters determination already assessed in the dosimetry and radiobiology fields. We consider this a significant achievement, especially considering that the accelerator is still in its installation and commissioning phase. However, significant improvement could be obtained in fluence and dose monitoring accuracy and precision.

The latter was the focus of the latest part of the research activity, carried out during the transition phase of the TOP-IMPLART accelerator to a maximum proton energy of 55.5 MeV and the subsequent commissioning. This activity, pertaining the field of beam instrumentation, involved the qualification of a new, non-interceptive monitor specifically developed for precision measurements of the proton current in the TOP-IMPLART range of operation, and the update of the control system of already available beam monitors.

Online availability, even to non-expert user, of the 2D ionization chamber dramatically increases the determination of the delivered dose accuracy with respect to the previous set-up which relied only on the accelerator dose reproducibility. This dose monitor, independent from the linac control system, has demonstrated a linearity of response within 3% with our reference, calibrated

dosimeter, the μDiamond. This brings the overall dose monitoring accuracy well below the prescribed ± 10% level, at least for low flux irradiation configuration.

The AC Current Transformer and an RF Passive Cavity can provide a complementary beam monitoring strategy, based on beam current monitors rather than ionization chambers. These devices, while possibly lacking the precision an ionization chamber can reach in dose measurements, can be employed to properly investigate dose-rate effects in the μDiamond and 2D Ionization chamber system. This feature is especially relevant for Displacement Damage tests which require flux levels nearly an order of magnitude higher than those of clinical applications and Single Event Effects tests. Moreover, for fluence rather than dose monitoring, an independent beam monitoring strategy could be investigated, based on online measurement of the extracted proton current coupled with absolute fluency calibration with activation techniques. This is the standard in many facilities involved in RHA activities and we hope it can be investigated in the future also at the TOP-IMPLART accelerator.

Even if numerous irradiation experiment on electronic components were proposed and evaluated with the 55.5 MeV proton beam configuration, none could be performed due to tight scheduling that strictly limited activities beyond the core topics of the TOP-IMPLART project, that is machine commissioning and radiobiology. At the time of this writing, a new energy improvement is underway and will bring the maximum proton beam energy to 71 MeV. Future electronic component irradiation campaigns will thus benefit from the updated monitoring system. We are confident they will further demonstrate that proton linear accelerators for cancer therapy are a meaningful and accurate alternative to cyclotrons for space component radiation resistance qualification.

APPENDIX A: P-I-N DIODE ACQUISITION SYSTEM

A.1 VOLTAGE CONTROLLED CURRENT SOURCE

To measure proton fluence without removing diodes from the position in the test geometry, a remote measuring system has been developed. The system operates in lockstep with irradiation experiment, keeping the BPW34F diode shorted during the irradiation step and performing the voltage measurement as soon as it finishes.

The 1 mA measurement current is generated by a Voltage Controlled Current Source (VCCS) circuit realized with the LT1213 Operational Amplifier. The schematics is shown in Figure 77. The board scheme is reported at the end of this Appendix.

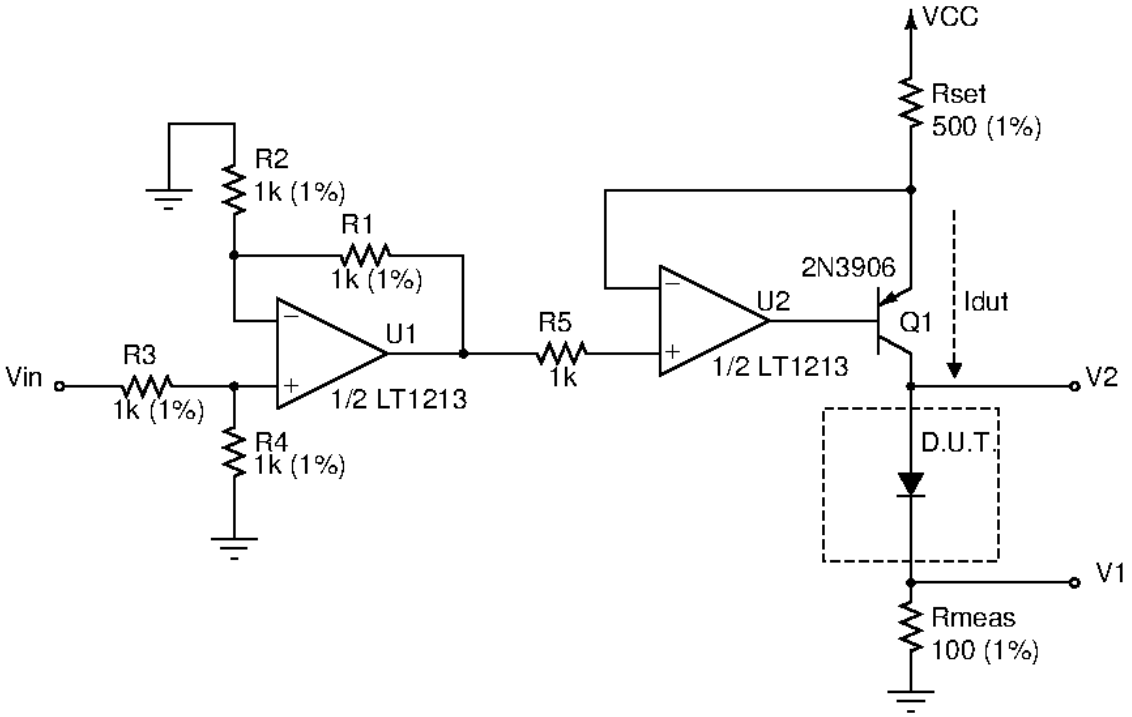

Figure 77 Voltage Controlled Voltage Source schematics

The LT1213 is a single supply precision dual op-amp already used in the control electronics of pulsed medical LINACs (IORT1, NOVAC, LIAC). Operational amplifiers positive power supply is VCC (not shown on the schematic) and the negative is ground.

The U1 acts as a non-inverting buffer whose output voltage follows the input one:

$$Vout1 = Vin$$

The output of U1 drives a current source realized by U2 Q1 and R_{set}. The current I_{dut} flowing into the D.U.T. is the collector current of Q1, that is set by:

$$Idut = \frac{VCC - Vset}{Rset}[A]$$

The current source supply voltage VCC is set to 12V. The transfer characteristics of the VCCS is, thus:

$$Idut = \frac{12 - Vset}{500}[A]$$

V_{set} assumes values between 0V and 10V.

A.2 sbRIO 9636 ACQUISITION SYSTEM

The 9636 single board RIO device is a reconfigurable single-board computer produced by National Instruments which combines an ARM processor, the NI Linux Real-Time OS, a programmable Xilinx FPGA Spartan-6 LX45 and built-in peripherals. Its characteristics and programming philosophy is the same as the compact RIO (cRIO) systems which is widely used in the control of the TOP-IMPLART accelerator. With respect to a cRIO system the available I/O are built-in in the sbRIO board and cannot be modified.

The analogue and digital signal employed for the BPW34F acquisition system have the following characteristics:

- analogue inputs (AI):

  range (programmable): ±1 V to ± 10 V

  resolution: 16 bit

operating mode: single-ended or differential

readout mode: multiplexed

max aggregated (16 ch) sample rate: 200 kS/s

- analogue outputs (AO):

  range: ± 10 V

  resolution: 16 bit

  max update rate: 336 kS/s

- digital input-outputs (DIO):

  Max input voltage: 3.3 V

Programmatic access to the remote system is performed via ethernet connection. LabVIEW programming of the device is structured on three levels, each performing a specific set of tasks:

FPGA (Spartan-6):	provides configuration of the I/O, temporization of signal generation and acquisition
Real Time (ARM):	acts as arbiter between the User interface and the FPGA for data transfer and configuration setting
User Interface (PC):	selects different configuration and acquisition mode, displays, elaborates, and saves data

The acquisition system is structured as a state machine, the main states corresponding to the three operating modalities:

Calibration	The diode is shorted; a pulse is generated and acquired to calibrate the current generator
Irradiation	The diode is shorted; no pulse is generated
Measurement	The diode is connected to the circuit; the pulse is generated for V_F measurement

Transition between states is arbitered by the User Interface which manages the user inputs and, through the real time code, sets the FPGA accordingly.

A.2.1 FPGA CONFIGURATION

Contrary to other NI embedded systems, such as cRIO, where the I/O can be configured by the Real Time code, in the sbRIO they are managed exclusively by the FPGA.

The FPGA software performs a system initialization setting the default value for the analogue and digital signals when first operated. It is then structured as a state machine, the three states being Calibration, Irradiation, Measurement. For each state the FPGA

sets a meaningful value for

- the DO that pilots the relay
- the DO that selects the diode to be measured
- the AO that drives the current generator V_{set}

reads the Analogue Inputs signal (even when no pulse is applied) V_1 and V_2 of Figure 77 so to obtain, through simple algebra, the meaningful physical signals:

- the diode V_F trace
- the current generator output trace

The analogue input channels are digitized with a 100 μS sampling period, 200 ms duration. Digitization starts 1 ms before the test current pulse is generated. As already mentioned, the AI acquisition is not synchronous, but multiplexed. As we are interested in the average value of the flat-top of the two signals, the slight delay between the two traces is negligible.

The digitized traces are tagged by a code number to identify the corresponding state (Irradiation/Measurement/Calibration) and are transferred to the RT code via a Direct Access Memory (DMA) FIFO.

A.2.2 REAL-TIME CONFIGURATION

The Real Time code is organized into a master loop and a slave loop. The master loop is synchronized with the FPGA code through an interrupt which is asserted

by the FPGA. The master loop configures the FPGA when there is a new request from the User Interface and reads the data from the DMA FIFO. The slave loop converts the digitized data from the two Analogue Input channels to double precision and transfers the data array to the user interface.

A.2.3 USER INTERFACE

The User Interface panel allows the User to interact with the acquisition system in a graphical environment. Raw and elaborated data from the Analogue Inputs traces are shown continuously, and average value on the flat top signals for the calibration factor, the test current and the voltage drop V_F.

Form the panel the user can set new parameters for the acquisition, such as the sampling period, sample size, pulse length, select one of the two diodes, start a calibration or a measurement. Additionally, a sequence of measurements can be requested to perform programmatically an I-V characterization of the diodes. Acquired data can be fitted "online" and saved on a file for later analysis. Figure 78 shows the front panel of the User interface.

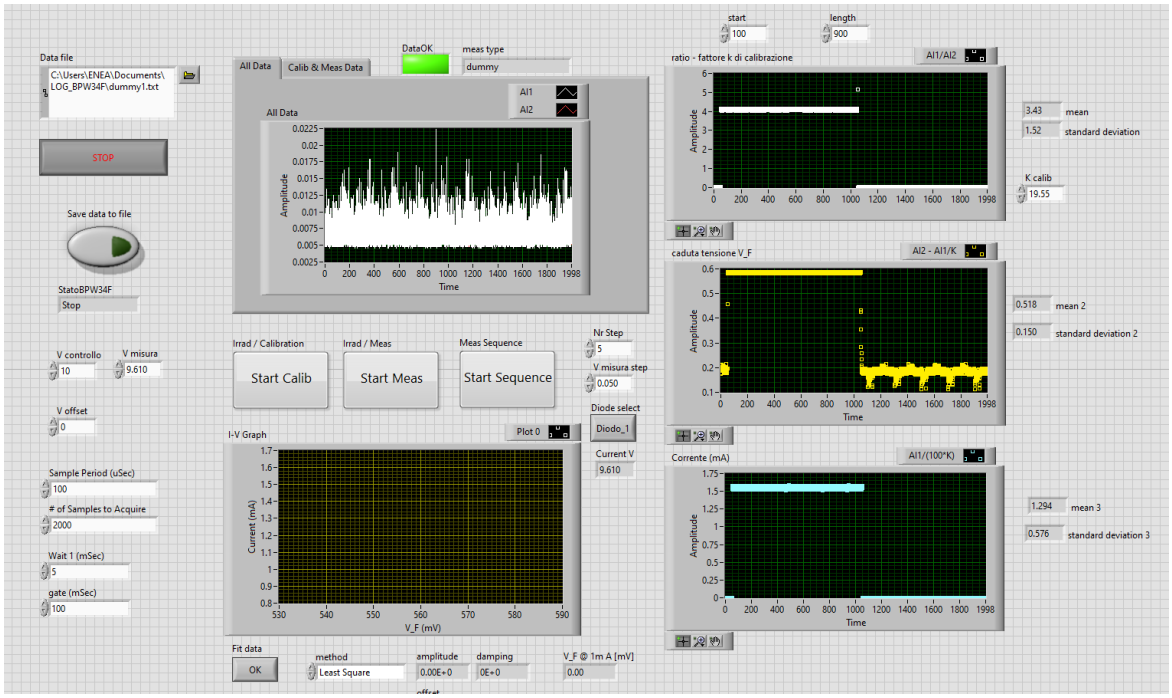

Figure 78 User Interface Panel for the BPW34F acquisition system

A.3 BOARD SCHEMATICS

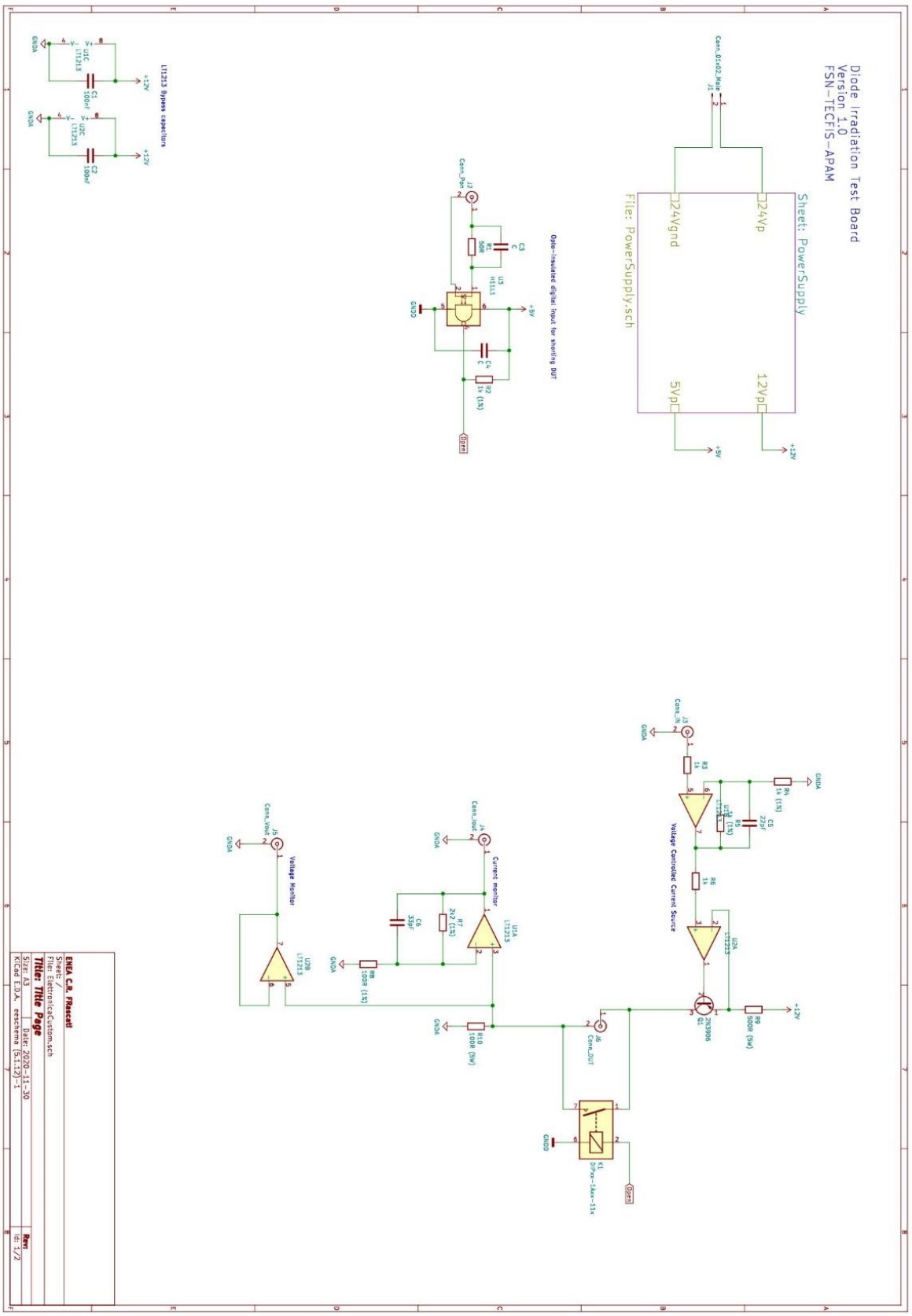

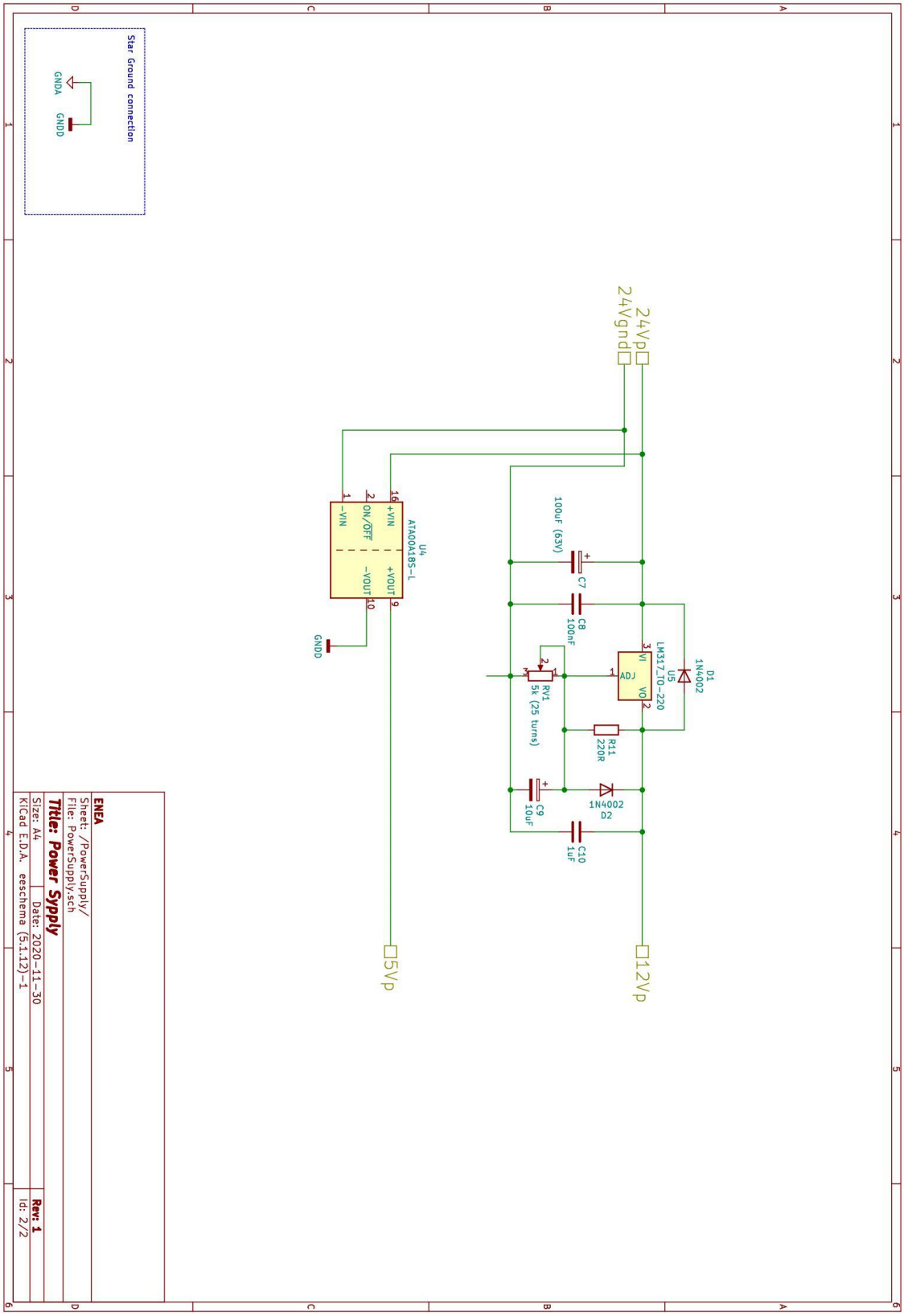
Star Ground connection
GNDA
GNDD
24Vp
24Vgnd
U4
ATA00A18S-L
16 +VIN
2 ON/OFF
1 -VIN
+VOUT 9
-VOUT 10
GNDD
5Vp
100uF (63V)
C7
C8
100nF
U5
LM317_TO-220
3 VI
ADJ
VO 2
D1
1N4002
RV1
5k (25 turns)
R11
220R
C9
10uF
1N4002
D2
C10
1uF
12Vp
ENEA
Sheet: /PowerSupply/
File: PowerSupply.sch
Title: Power Sypply
Size: A4
Date: 2020-11-30
KiCad E.D.A. eeschema (5.1.12)-1
Rev: 1
Id: 2/2

REFERENCES

Alia, R. G., Brugger, M., Daly, E., Danzeca, S., Ferlet-Cavrois, V., Gaillard, R., Mekki, J., Poivey, C., & Zadeh, A. (2017). Simplified SEE Sensitivity Screening for COTS Components in Space. *IEEE Transactions on Nuclear Science*, *64*(2), 882–890. https://doi.org/10.1109/TNS.2017.2653863

Amaldi, U., Braccini, S., & Puggioni, P. (2009). High Frequency Linacs for Hadrontherapy. *Reviews of Accelerator Science and Technology*, *02*(01), 111–131. https://doi.org/10.1142/S179362680900020X

Amaldi, U., Szeless, B., Vretenar, M., Wilson, E., Crandall, K., Mauri, M., Weiss, M., & Stovall, J. (1998). LIBO: a 3 GHz proton linac booster of 200 MeV for cancer treatment. *Proceedings of International Linear Accelerator Conference (LINAC'98)*, 663.

Ampollini, A., Basile, E., Bazzano, G., Cisbani, E., de Angelis, C., della Monaca, S., Ghio, F., Giuliani, F., Lucentini, M., Nenzi, P., Placido, C., Picardi, L., Ronsivalle, C., Santavenere, F., Spurio, A., Surrenti, V., & Vadrucci, M. (2020). Recombination effects in the ionization chambers dose delivery monitor of the TOP-IMPLART proton beam. *Journal of Physics: Conference Series*, *1561*(1), 012008. https://doi.org/10.1088/1742-6596/1561/1/012008

ASTM Committee. (1994). *ASTM E772-94 Standard practice for characterizing neutron fuence spectra in terms of an equivalent monoenergetic neutron fuence for radiation hardness testing of electronics*.

Bazzano, G., Ampollini, A., Cardelli, F., Fortini, F., Nenzi, P., Palmerini, G. B., Picardi, L., Piersanti, L., Ronsivalle, C., Surrenti, V., Trinca, E., Vadrucci, M., & Sabatini, M. (2021). Radiation testing of a commercial 6-axis MEMS inertial navigation unit at ENEA Frascati proton linear accelerator. *Advances in Space Research*, *67*(4). https://doi.org/10.1016/j.asr.2020.11.031

Bazzano, G., Ampollini, A., Cardelli, F., Fortini, F., Nenzi, P., Picardi, L., Piersanti, L., Ronsivalle, C., Surrenti, V., Trinca, E., Vadrucci, M., Sabatini, M., & Palmerini, G. B. (2019). Radiation testing for space applications at ENEA Frascati 35 MeV proton linear accelerator. *Proceedings of the International Astronautical Congress, IAC*, *2019-Octob*.

Bazzano, G., Basile, E., Nenzi, P., Picardi, L., Piccinini, M., Pittà, G., Ronsivalle, C., Surrenti, V., Vadrucci, M., & Verona Rinati, G. (2016). First beam characterization of the TOP-IMPLART proton linear accelerator for cancer radiotherapy. *Proceedings to the 55 th Annual Meeting for the Particle Therapy Cooperative Group (PTCOG), First Beam Characterization of the TOP-IMPLART Proton Linear Accelerator for Cancer RadiotherapyInternational Journal of Particle Therapy*, *3*(1), 71–276. https://doi.org/10.14338/IJPT.16-PTCOG-1.1

Bazzano, G., Borgognoni, F., Nenzi, P., Palmerini, G. B., Picardia, L., Ronsivalle, C., Sabatini, M., & Vadrucci, M. (2020). Dynamic radiation testing on commercial integrated MEMS inertial navigation system with X-rays and electrons. *Proceedings of the International Astronautical Congress, IAC*, *2020-Octob*.

Berger, M. J., Coursey, J. S., & Chang, M. A. (2005). *ESTAR, PSTAR, and ASTAR: Computer Programs for Calculating Stopping- Power and Range Tables for Electrons, Protons, and Helium Ion (version 1.2.3)*. https://www.nist.gov/pml/stopping-power-range-tables-electrons-protons-and-helium-ions

Bisello, D., Candelori, A., Ferlet-Cavrois, V., Giubilato, P., Mattiazzo, S., Pantano, D., Silvestrin, L., Tessaro, M., & Wyss, J. (n.d.). *SEU cross section measurement of the ESA SEU monitor*. http://pif.web.psi.ch/

Borgognoni, F., Vadrucci, M., Bazzano, G., Ferrari, P., Massa, S., Moretti, R., Calvitti, M., Ronsivalle, C., Moriani, A., & Picardi, L. (2017). X-ray sterilization of insects and microorganisms for cultural heritage applications. *Nuclear Instruments and Methods in Physics Research, Section B: Beam Interactions with Materials and Atoms*, *406*. https://doi.org/10.1016/j.nimb.2017.03.033

Campola, M. J., & Pellish, J. A. (2019). *RADECS2019 short course - Radiation Hardness Assurance: Evolving for NewSpace*.

Cardelli, F., Ampollini, A., Bazzano, G., Nenzi, P., Piersanti, L., Ronsivalle, C., & Picardi, L. (2021). Design and test of a compact beam current monitor based on a passive RF cavity for a proton therapy linear accelerator. *Review of Scientific Instruments*, *92*(11), 113304. https://doi.org/10.1063/5.0062509

Cisbani, E., Carloni, A., Colilli, S., de Angelis, G., Frullani, S., Ghio, F., Giuliani, F., Gricia, M., Lucentini, M., Notaro, C., Santavenere, F., Spurio, A., Vacca, G.,

Ampollini, A., Nenzi, P., Picardi, L., Ronsivalle, C., Vadrucci, M., Basile, E., … Placido, C. (2016). Micro Pattern Ionization Chamber with Adaptive Amplifiers as Dose Delivery Monitor for Therapeutic Proton LINAC. *Proceedings of the International Beam Instrumentation Conference (5th)*. https://accelconf.web.cern.ch/ibic2016/doi/JACoW-IBIC2016-TUPG51.html

Coronetti, A., Alia, R. G., Budroweit, J., Rajkowski, T., Costa Lopes, I. da, Niskanen, K., Soderstrom, D., Cazzaniga, C., Ferraro, R., Danzeca, S., Mekki, J., Manni, F., Dangla, D., Virmontois, C., Kerboub, N., Koelpin, A., Saigne, F., Wang, P., Pouget, V., … Germanicus, R. C. (2021). Radiation Hardness Assurance Through System-Level Testing: Risk Acceptance, Facility Requirements, Test Methodology, and Data Exploitation. *IEEE Transactions on Nuclear Science*, *68*(5), 958–969. https://doi.org/10.1109/TNS.2021.3061197

Crandall, K. R., & Weiss, M. (1994). *LINAC code - TERA 94/34 ACC 20 (internal note)*.

de Angelis, C., Ampollini, A., Bazzano, G., della Monaca, S., Ghio, F., Giuliani, F., Lucentini, M., Montereali, R. M., Nenzi, P., Notaro, C., Placido, C., Piccinini, M., Ronsivalle, C., Santavenere, F., Soriani, A., Spurio, A., Strigari, L., Surrenti, V., Trinca, E., … Picardi, L. (2019). THE TOP-IMPLART PROTON LINEAR ACCELERATOR: INTERIM CHARACTERISTICS OF THE 35 MEV BEAM. *Radiation Protection Dosimetry*, *186*(1). https://doi.org/10.1093/rpd/ncz142

di Mascio, S., Menicucci, A., Furano, G., Szewczyk, T., Campajola, L., di Capua, F., Lucaroni, A., & Ottavi, M. (2018). Towards defining a simplified procedure for COTS system-on-chip TID testing. *Nuclear Engineering and Technology*, *50*(8), 1298–1305. https://doi.org/10.1016/j.net.2018.07.010

ESCC Basic Specification No. 22500 - GUIDELINES FOR DISPLACEMENT DAMAGE IRRADIATION TESTING. (2019). https://escies.org

ESCC Basic Specification No. 25100 - SINGLE EVENT EFFECTS TEST METHOD AND GUIDELINES. (2014). https://escies.org

Fausti, F., Mazza, G., Attili, A., Mazinani, M. F., Giordanengo, S., Lavagno, M., Manganaro, L., Marchetto, F., Monaco, V., Sacchi, R., Vignati, A., & Cirio, R. (2017). Design and characterization of a 64 channels ASIC front-end electronics for high-flux particle beam detectors. *Nuclear Instruments and*

Methods in Physics Research Section A: Accelerators, Spectrometers, Detectors and Associated Equipment, *867*, 1–6. https://doi.org/10.1016/J.NIMA.2017.04.025

Garcia Alia, R., & Cecchetto, M. (2020). *Radiation Test Report – ESA SEU MONITOR CALIBRATION; EDMS Document No. 2059465 v.1*. https://edms.cern.ch/ui/#!master/navigator/document?D:100251968:100251968:subDocs

Gkotse, B., Glaser, M., Moll, M., & Ravotti, F. (2015). IRRAD: THE NEW 24GeV/c PROTON IRRADIATION FACILITY AT CERN. *12th International Topical Meeting on Nuclear Applications of Accelerators, Washington, DC, USA*, 182–187.

Hamm, W. R., Crandall, K. R., & Potter, J. M. (1991). Preliminary design of a dedicated proton therapy linac. *Proceedings of Particle Accelerator Conference (PAC91)*, 2583–2585.

Harboe-Sørensen, R., Poivey, C., Guerre, F. X., Roseng, A., Lochon, F., Berger, G., Hajdas, W., Virtanen, A., Kettunen, H., & Duzellier, S. (2008). From the reference SEU monitor to the technology demonstration module on-board PROBA-II. *IEEE Transactions on Nuclear Science*, *55*(6), 3082–3087. https://doi.org/10.1109/TNS.2008.2006896

Harryman, D. M., & Pertica, A. (2016). Online Total Ionisation Dosimeter (TID) Monitoring Using Semiconductor Based Radiation Sensors in the ISIS Proton Synchrotron. *Proceedings of IBIC 2016, Barcelona, Spain*. https://www.researchgate.net/publication/308520838

JEDEC Solid State Technology Association. (2013). *JESD234 - Test Standard for the Measurement of Proton Radiation Single Event Effects in Electronic Devices*.

Kaiser, F. J., Bassler, N., & Jäkel, O. (2010). COTS Silicon diodes as radiation detectors in proton and heavy charged particle radiotherapy 1. *Radiation and Environmental Biophysics*, *49*(3), 365–371. https://doi.org/10.1007/s00411-010-0299-8

Klesh, A., Seagreaves, S., Bennett, M., Boone, D., Cutler, J., & Bahcivan, H. (2009). Dynamically driven Helmholtz Cage for experimental magnetic attitude determination. *2009 AAS/AIAA Astrodynamics Specialist Conference*.

Knudson, A. R., Buchner, S., McDonald, P., Stapor, W. J., Campbell, A. B., Grabowski, K. S., & Knies, D. L. (1996). The effects of radiation on mems accelerometers. *IEEE Transactions on Nuclear Science*, *43*(6 PART 1), 3122–3126. https://doi.org/10.1109/23.556914

la Rosa, A., Donetti, M., Borri, M., Rivero, F., Attili, A., Bourhaleb, F., Cirio, R., Garella, M. A., Giordanengo, S., Givehchi, N., Mazza, G., Marchetto, F., Pardo, J., Pecka, A., & Peroni, C. (2008). Characterization of a front-end electronics for the monitoring and control of hadrontherapy beams. *Nuclear Instruments and Methods in Physics Research Section A: Accelerators, Spectrometers, Detectors and Associated Equipment*, *586*(2), 270–275. https://doi.org/10.1016/j.nima.2007.12.012

Lal, B., Balakrishnan, A., Picard, A., Corbin, B., Behrens, J., Green, E., & Myersm Roger. (2017). *Trends in Small Satellite Technology*.

Malfante, L. (1992). *Utilisation de dosimetres semi-conducteurs au silicium autour del accelerateurs de particules a haute energie*.

Mandapaka, A. K., Ghebremedhin, A., Patyal, B., Marinelli, M., Prestopino, G., Verona, C., & Verona-Rinati, G. (2013). Evaluation of the dosimetric properties of a synthetic single crystal diamond detector in high energy clinical proton beams. *Medical Physics*, *40*(12), 121702. https://doi.org/10.1118/1.4828777

Marsolat, F., de Marzi, L., Patriarca, A., Nauraye, C., Moignier, C., Pomorski, M., Moignau, F., Heinrich, S., Tromson, D., & Mazal, A. (2016). Dosimetric characteristics of four PTW microDiamond detectors in high-energy proton beams. *Physics in Medicine and Biology*, *61*(17), 6413–6429. https://doi.org/10.1088/0031-9155/61/17/6413

Mekki, J. (2009). *Characterization and performance optimization of radiation monitoring sensors for high energy physics experiments at the CERN LHC and Super-LHC*.

Nenzi, P., Ampollini, A., Bazzano, G., Picardi, L., Ronsivalle, C., Trinca, E., Surrenti, V., & Vadrucci, M. (2018). STABILITY ANALYSIS OF THE TOP-IMPLART 35 MeV PROTON BEAM. *9th International Particle Accelerator Conference*, 697–700.

Nichelatti, E., Ronsivalle, C., Piccinini, M., Picardi, L., & Montereali, R. M. (2019). An analytical approximation of proton Bragg curves in lithium fluoride for beam energy distribution analysis. *Nuclear Instruments and Methods in Physics Research Section B: Beam Interactions with Materials and Atoms*, *446*, 29–36. https://doi.org/10.1016/J.NIMB.2019.03.026

Nightingale, M. P. S., Holmes, A. J. T., & Griffiths, N. (1992). Booster linear accelerator for proton therapy. *Proceedings of the Linear Acceleration Conference (LINAC'92)*, 398–401.

Noordeh, E., & Garcia Alia, R. (2014). *Simulating Heavy Ion SEUs in the ESA Monitor*.

Oelfke, U., Blackmore, E., Gardey, K., & Lam, G. K. Y. (1995). Proton Dosimetry at TRIUMF: Experimental Profiles and PTRAN MC Calculations. *PTCOGG 1995*.

Oudea, C., Poirot, P., Gaillard, R., Poivey, C., & Marchand, L. (2009). Single Event Effects in MEMS Accelerometers. *2009 IEEE Radiation Effects Data Workshop*, 94–98. https://doi.org/10.1109/REDW.2009.5336309

Palni, P., Hoeferkamp, M., Taylor, A., Vora, S., McDuff, H., Gu, Q., & Seidel, S. (2013). *A Method for Real Time Monitoring of Charged Particle Beam Profile and Fluence*. https://doi.org/10.1016/j.nima.2013.09.037

Pang, W. J., Bo, B., Meng, X., Yu, X. Z., Guo, J., & Zhou, J. (2016). Boom of the cubesat: A statistic survey of cubsats launch in 2003-2015. *Proceedings of the International Astronautical Congress, IAC*, *0*.

Picardi, L., Ampollini, A., Bazzano, G., Cisbani, E., Ghio, F., Montereali, R. M., Nenzi, P., Piccinini, M., Ronsivalle, C., Santavenere, F., Surrenti, V., Trinca, E., Vadrucci, M., & Tafo, E. W. (2020). Beam commissioning of the 35 MeV section in an intensity modulated proton linear accelerator for proton therapy BEAM COMMISSIONING of the 35 MeV ... L. PICARDI et al. *Physical Review Accelerators and Beams*, *23*(2). https://doi.org/10.1103/PHYSREVACCELBEAMS.23.020102

Picardi, L., Ronsivalle, C., & Hamm, R. (2000). Beam injection study of the TOP linac using an ACCSYS model PL-7 linac. *Proceedings of European Particle Accelerator Conference (EPAC2000)*, 1675.

Picardi, L., Ronsivalle, C., & Vignati, A. (1995). *Patent No. RM95-A000564*.

Piccinini, M., Nichelatti, E., Ronsivalle, C., Ampollini, A., Bazzano, G., Bonfigli, F., Nenzi, P., Surrenti, V., Trinca, E., Vadrucci, M., Vincenti, M. A., Picardi, L., & Montereali, R. M. (2019). Visible photoluminescence of color centers in LiF crystals for advanced diagnostics of 18 and 27 MeV proton beams. *Radiation Measurements*, *124*. https://doi.org/10.1016/j.radmeas.2019.03.010

Pitt, E. B., Barth, E. J., Diggins, Z. J., Mahadevan, N., Karsai, G., Sierawski, B. D., Reed, R. A., Schrimpf, R. D., Weller, R. A., Alles, M. L., Alles, M. L., & Witulski, A. F. (2017). Radiation Response and Adaptive Control-Based Degradation Mitigation of MEMS Accelerometers in Ionizing Dose Environments. *IEEE Sensors Journal*, *17*(4), 1132–1143. https://doi.org/10.1109/JSEN.2016.2640199

RADIATION REQUIREMENTS GUIDELINES FOR MEMS DEVICES. (2009).

Ravotti, F. (2006). *Development and Characterisation of Radiation Monitoring Sensors for the High Energy Physics Experiments of the CERN LHC Accelerator*.

Ravotti, F. (2018). Dosimetry techniques and radiation test facilities for total ionizing dose testing. *IEEE Transactions on Nuclear Science*, *65*(8), 1440–1464. https://doi.org/10.1109/TNS.2018.2829864

Ravotti, F., Glaser, M., & Moll, M. (2005). *"SENSOR CATALOGUE" DATA COMPILATION OF SOLID-STATE SENSORS FOR RADIATION MONITORING*.

Ravotti, F., Glaser, M., Moll, M., & Saigne, F. (2008). BPW34 Commercial p-i-n Diodes for High-Level 1-MeV Neutron Equivalent Fluence Monitoring. *IEEE Transactions on Nuclear Science*, *55*(4), 2133–2140. https://doi.org/10.1109/TNS.2008.2000765

Ronsivalle, C., Carpanese, M., Marino, C., Messina, G., Picardi, L., Sandri, S., Basile, E., Caccia, B., Castelluccio, D. M., Cisbani, E., Frullani, S., Ghio, F., Macellari, V., Benassi, M., D'Andrea, M., & Strigari, L. (2011). The TOP-IMPLART project. *European Physical Journal Plus*, *126*(7), 1–15. https://doi.org/10.1140/epjp/i2011-11068-x

Rousselet, M., Adell, P. C., Sheldon, D. J., Boch, J., Schone, H., & Saigne, F. (2017). Use and benefits of COTS board level testing for radiation hardness assurance. *Proceedings of the European Conference on Radiation and Its Effects on Components and Systems, RADECS*, *2016-Septe*, 1–5. https://doi.org/10.1109/RADECS.2016.8093122

Schippers, J. M., & Seidel, M. (2014). ACCELERATORS FOR MEDICAL APPLICATION: WHAT IS SO SPECIAL? *Proceedings of IPAC2014*.

Sinclair, D., & Dyer, J. (2013). *SSC13-IV-3 Radiation Effects and COTS Parts in SmallSats*.

Springmann, J. C., Cutler, J. W., & Bahcivan, H. (2011). Initial flight results of the Radio Aurora Explorer. *62nd International Astronautical Congress 2011, IAC 2011*, *5*, 3833–3841.

Summers, G. P., Burke, E. A., Shapiro, P., Messenger, S. R., & Walters, R. J. (1993). Damage correlations in semiconductors exposed to gamma, electron and proton radiations. *IEEE Transactions on Nuclear Science*, *40*(6), 1372–1379. https://doi.org/10.1109/23.273529

Testing at the Speed of Light. (2018). National Academies Press. https://doi.org/10.17226/24993

Vadrucci, M., Bazzano, G., Borgognoni, F., Chiari, M., Mazzinghi, A., Picardi, L., Ronsivalle, C., Ruberto, C., & Taccetti, F. (2017). A new small-footprint external-beam PIXE facility for cultural heritage applications using pulsed proton beams. *Nuclear Instruments and Methods in Physics Research, Section B: Beam Interactions with Materials and Atoms*, *406*. https://doi.org/10.1016/j.nimb.2017.02.045

Vadrucci, M., Borgognoni, F., Cicero, C., Perini, N., Migliore, L., Mercuri, F., Orazi, N., & Rubechini, A. (2019). Parchment processing and analysis: Ionizing radiation treatment by the REX source and multidisciplinary approach characterization. *Applied Radiation and Isotopes*, *149*, 159–164. https://doi.org/10.1016/j.apradiso.2019.04.021

Vadrucci, M., Esposito, G., Ronsivalle, C., Cherubini, R., Marracino, F., Montereali, R. M., Picardi, L., Piccinini, M., Pimpinella, M., Vincenti, M. A., & de Angelis, C. (2015). Calibration of GafChromic EBT3 for absorbed dose measurements

in 5 MeV proton beam and ^{60}Co γ-rays. *Medical Physics*, *42*(8), 4678–4684. https://doi.org/10.1118/1.4926558

Vadrucci, M., Ferrari, P., Borgognoni, F., & Campani, L. (2019). The REX irradiation facility and its applications. *Nuclear Instruments and Methods in Physics Research, Section A: Accelerators, Spectrometers, Detectors and Associated Equipment*, *930*, 126–131. https://doi.org/10.1016/j.nima.2019.02.066

Vasilescu, A., & Lindstroem, G. (n.d.). *Displacement Damage in Silicon online compilation*. Retrieved December 9, 2021, from http://rd50.web.cern.ch/RD50/NIEL/default.html

Williams, C., Doncaster, B., & Shulman, J. (2018). *Nano/Microsatellite Market Forecast* (8th ed.). SpaceWorks Enterprises Inc.

Ziegler, J. F., Ziegler, M. D., & Biersack, J. P. (2010). SRIM – The stopping and range of ions in matter (2010). *Nuclear Instruments and Methods in Physics Research Section B: Beam Interactions with Materials and Atoms*, *268*(11–12), 1818–1823. https://doi.org/10.1016/j.nimb.2010.02.091

ACKNOWLEDGEMENTS

This thesis work has been carried out at ENEA Frascati Particle Accelerator and Medical Application Laboratory within the TOP-IMPLART project, funded by Regione Lazio and Lazio Innova.

.

LIST OF PUBLICATIONS

In this section, the list of the publications produced during the PhD research activities is reported.

Journal Papers:

Cardelli, F., Ampollini, A., Bazzano, G., Nenzi, P., Piersanti, L., Ronsivalle, C., Picardi, L.
Design and test of a compact beam current monitor based on a passive RF cavity for a proton therapy linear accelerator
(2021) Review of Scientific Instruments, 92 (11), art. no. 113304,
DOI: 10.1063/5.0062509

Cecchetto, M., Alia, R.G., Wrobel, F., Coronetti, A., Bilko, K., Lucsanyi, D., Fiore, S., Bazzano, G., Pirovano, E., Nolte, R.
0.1-10 MeV Neutron Soft Error Rate in Accelerator and Atmospheric Environments
(2021) IEEE Transactions on Nuclear Science, 68 (5), art. no. 9373367, pp. 873-883.
DOI: 10.1109/TNS.2021.3064666

Bazzano, G., Ampollini, A., Cardelli, F., Fortini, F., Nenzi, P., Palmerini, G.B., Picardi, L., Piersanti, L., Ronsivalle, C., Surrenti, V., Trinca, E., Vadrucci, M., Sabatini, M.
Radiation testing of a commercial 6-axis MEMS inertial navigation unit at ENEA Frascati proton linear accelerator
(2021) Advances in Space Research, 67 (4), pp. 1379-1391.
DOI: 10.1016/j.asr.2020.11.031

Piccinini, M., Nichelatti, E., Ampollini, A., Bazzano, G., De Angelis, C., Della Monaca, S., Nenzi, P., Picardi, L., Ronsivalle, C., Surrenti, V., Trinca, E., Vadrucci, M., Vincenti, M.A., Montereali, R.M.
Dose response and Bragg curve reconstruction by radiophotoluminescence of color centers in lithium fluoride crystals irradiated with 35 MeV proton beams from 0.5 to 50 Gy
(2020) Radiation Measurements, 133, art. no. 106275,
DOI: 10.1016/j.radmeas.2020.106275

Picardi, L., Ampollini, A., Bazzano, G., Cisbani, E., Ghio, F., Montereali, R.M., Nenzi, P., Piccinini, M., Ronsivalle, C., Santavenere, F., Surrenti, V., Trinca, E., Vadrucci, M., Tafo, E.W.
Beam commissioning of the 35 MeV section in an intensity modulated proton linear accelerator for proton therapy
(2020) Physical Review Accelerators and Beams, 23 (2), art. no. 020102,
DOI: 10.1103/PHYSREVACCELBEAMS.23.020102

De Angelis, C., Ampollini, A., Bazzano, G., Della Monaca, S., Ghio, F., Giuliani, F., Lucentini, M., Montereali, R.M., Nenzi, P., Notaro, C., Placido, C., Piccinini, M., Ronsivalle, C., Santavenere, F., Soriani, A., Spurio, A., Strigari, L., Surrenti, V., Trinca, E., Vadrucci, M., Cisbani, E., Picardi, L.
The TOP-IMPLART proton linear accelerator: interim characteristics of the 35 MeV beam
(2019) Radiation Protection Dosimetry, 186 (1), pp. 113-118.
DOI: 10.1093/rpd/ncz142

Piccinini, M., Nichelatti, E., Ronsivalle, C., Ampollini, A., Bazzano, G., Bonfigli, F., Nenzi, P., Surrenti, V., Trinca, E., Vadrucci, M., Vincenti, M.A., Picardi, L., Montereali, R.M.
Visible photoluminescence of color centers in LiF crystals for advanced diagnostics of 18 and 27 MeV proton beams
(2019) Radiation Measurements, 124, pp. 59-62.
DOI: 10.1016/j.radmeas.2019.03.010

Conference Papers:

Bazzano, G., Ampollini, A., Cisbani, E., De Angelis, C., Della Monaca, S., Nenzi, P., Nichelatti, E., Palmerini, G.B., Picardi, L., Piccinini, M., Ronsivalle, C., Sabatini, M.
Beam characterization methods at the TOP-IMPLART proton linear accelerator: An application to space components qualification
(2021) 2021 IEEE International Workshop on Metrology for AeroSpace, MetroAeroSpace 2021 - Proceedings, art. no. 9511719, pp. 37-41.
DOI: 10.1109/MetroAeroSpace51421.2021.9511719

Coronetti, A., Cecchetto, M., Wang, J., Tali, M., Martinez, P.F., Kastriotou, M., Papadopoulou, A., Bilko, K., Castellani, F., Sacristan, M., Alia, R.G., Cazzaniga, C., Morilla, Y., Martin-Holgado, P., Van Goethem, M.-J., Kiewiet, H., Van Der Graaf, E., Brandenburg, S., Hajdas, W., Sinkunaite, L., Marszalek, M., Kettunen, H., Rossi, M., Jaatinen, J., Javanainen, A., Moscatello, M.-H., Dubois, A., Fiore, S.,

Bazzano, G., Frost, C., Letiche, M., Farabolini, W., Gilardi, A., Corsini, R., Puchner, H.
SEU characterization of commercial and custom-designed SRAMs based on 90 nm technology and below
(2020) IEEE Radiation Effects Data Workshop, 2020-November, art. no. 9325822, DOI: 10.1109/REDW51883.2020.9325822

Ampollini, A., Basile, E., Bazzano, G., Cisbani, E., De Angelis, C., Della Monaca, S., Ghio, F., Giuliani, F., Lucentini, M., Nenzi, P., Placido, C., Picardi, L., Ronsivalle, C., Santavenere, F., Spurio, A., Surrenti, V., Vadrucci, M.
Recombination effects in the ionization chambers dose delivery monitor of the TOP-IMPLART proton beam
(2020) Journal of Physics: Conference Series, 1561 (1), art. no. 012008, DOI: 10.1088/1742-6596/1561/1/012008

Bazzano, G., Borgognoni, F., Nenzi, P., Palmerini, G.B., Picardi, L., Ronsivalle, C., Sabatini, M., Vadrucci, M.
Dynamic radiation testing on commercial integrated MEMS inertial navigation system with X-rays and electrons
(2020) Proceedings of the International Astronautical Congress, IAC, 2020-October,

Bazzano, G., Ampollini, A., Cardelli, F., Fortini, F., Nenzi, P., Picardi, L., Piersanti, L., Ronsivalle, C., Surrenti, V., Trinca, E., Vadrucci, M., Sabatini, M., Palmerini, G.B.
Radiation testing for space applications at ENEA Frascati 35 MeV proton linear accelerator
(2019) Proceedings of the International Astronautical Congress, IAC, 2019-October, art. no. IAC-19_D5_3_10_x53110,

Bazzano, G., Ampollini, A., Blasi, L., Cardelli, F., Cisbani, E., De Angelis, C., Della Monaca, S., Mastrandrea, A., Menichelli, F., Nenzi, P., Olivieri, M., Palmerini, G.B., Picardi, L., Piccinini, M., Ronsivalle, C., Sabatini, M., Vigli, F.,
Dosimetric characterization of an irradiation set-up for electronic components testing at the TOP-IMPLART proton linear accelerator
(2019) proceedings of RADECS 2019, Montpellier, France (to be published on IEEExplore)